Energy Loss and Flow of Heavy Quarks in Au+Au Collisions at $\sqrt{s_{NN}}$ = 200 GeV

A Dissertation Presented

by

Alan Dion

to

The Graduate School

in Partial Fulfillment of the Requirements

for the Degree of

Doctor of Philosophy

in

Physics

Stony Brook University

May 2007

Stony Brook University

The Graduate School

Alan Dion

We, the dissertation committee for the above candidate for the Doctor of Philosophy degree, hereby recommend acceptance of this dissertation.

Axel Drees
Department of Physics & Astronomy

Abhay Deshpande
Department of Physics & Astronomy

Warren Siegel
Department of Physics & Astronomy

Michael Leitch
Los Alamos National Laboratory

This dissertation is accepted by the Graduate School.

Lawrence Martin
Dean of the Graduate School

Abstract of the Dissertation

Energy Loss and Flow of Heavy Quarks in Au+Au Collisions at $\sqrt{s_{NN}} = 200$ GeV

by

Alan Dion

Doctor of Philosophy

in

Physics

Stony Brook University

2007

Axel Drees

Two of the most interesting results to come from the heavy ion program at the Relativistic Heavy Ion Collider (RHIC) are the observation of jet suppression and elliptic flow. The production of light mesons from Au+Au collisions is suppressed at large momentum compared to that from p+p collisions at the same energy per nucleon when the number of nucleon-nucleon collisions is taken into account. Secondly, the meson production is highly asymmetric with respect to the reaction plane, the plane formed by the impact parameter and the beam axis, indicating strong collective behavior of produced particles, consistent with hydrodynamic expansion.

Jet suppression and azimuthal anisotropy of mesons containing heavy quarks can in principle give more direct information about the properties of the medium than can light mesons. At RHIC, charm and bottom quarks are believed to be formed exclusively in the initial hard nucleon scatterings, predominately by gluon-gluon

fusion. Since the heavy quarks are formed early in the collision, their spectrum is sensitive to the entire lifespan of the medium formed. Heavy quarks are predicted to lose less energy than light quarks traversing the medium due to the "dead-cone" effect, and as such could be more sensitive to medium effects than are the light quarks.

This dissertation details the measurement of electrons from heavy quark decays from Au+Au collisions at $\sqrt{s_{NN}} = 200$ GeV using the PHENIX detector over a transverse momentum range of 0.3 GeV/c < p_T < 9.0 GeV/c. The measurement of the azimuthal anisotropy with respect to the reaction plane of electrons from heavy quark decays is also presented. The results of the measurement are compared to predictions from recent theoretical work. It is found that the energy loss models used to describe the light meson suppression are insufficient to describe the suppression of electrons from heavy quarks. Models based on collective motion of the heavy quarks with the medium which give a simultaneous description of the suppression and anisotropy of heavy quarks provide evidence that the bulk properties of the medium can be extracted by the data presented in this thesis.

Contents

List of Figures

List of Tables

Acknowledgements

I start by thanking my thesis advisor, Axel Drees. Axel believed in my ability, encouraged me to work in this field, and always made time to work with me. Whenever I would become stressed with work, or had lost sight of the important physics we were trying to study, a conversation with Axel would remind me of why I had endeavored into experimental physics in the first place and give me insight into solving whatever technical problem was bothering me. He taught me how to find the most simple and clear approach to solving a complex problem. Axel has been a great advisor, and a great friend.

I was lucky enough to work with Ralf Averbeck, who is a pioneer of the analysis which led to this thesis. Ralf and I developed a rapport which made working together easy and fun. I would rarely have to finish my sentence when asking him a question, and his answers were just as easy for me to understand. The speed and success I have had in writing this thesis are due largely to the diligence and enthusiasm of Ralf.

It has been amazing to be a part of the PHENIX collaboration. Having so many people from whom to draw help and encouragement has been instrumental in my development as a physicist. I am particularly grateful to the Relativistic Heavy Ion Group at Stony Brook. I hope that the size and strength of the group persists for many years to come.

Lastly, I would like to thank my parents, who have supported me in all of my endeavors for my entire life. To them, I owe more than I can put into words.

Chapter 1

Introduction

1.1 Motivation

The main goal of the Relativistic Heavy Ion Collider (RHIC) is to create, identify, and study quark gluon plasma (QGP), the state of matter hypothesized to exist when nuclear matter reaches high enough temperatures or densities [1]. The QGP is a state of nuclear matter in which the degrees of freedom are colored partons (quarks and gluons), or composite colored objects, instead of the color-neutral hadronic states which can be directly observed. Figure 1.1 shows a schematic version of the phase diagram for idealized nuclear matter with two massless quarks and one infinitely heavy quark as a function of temperature and baryon chemical potential. The matter formed in RHIC collisions should have low chemical potential and high temperature. That these equilibrium concepts even apply to the system has sound experimental backing. An overview of the evidence for the creation of quark-gluon matter at RHIC can be found in the experimental "white papers" of the four experiments at RHIC [2, 3, 4, 5].

Regardless of whether QGP is actually created at RHIC, it is interesting to study the properties of high temperature nuclear matter. Since the medium created is so small (~ 1000 fm^3), and so short-lived (~ 100 fm/c), any observable of the medium must be probed with particles created during the collision. There are many observables which are accessible to the experiments at RHIC, which are outlined in the experimental white papers. Perhaps the most sensitive type of probes of the medium properties are so-called penetrating probes. There are two main classes of penetrating probes:

- Hard probes
  Particles created from QCD hard-scattering are produced at the very early stage of the collision. Since they are produced in the initial in-

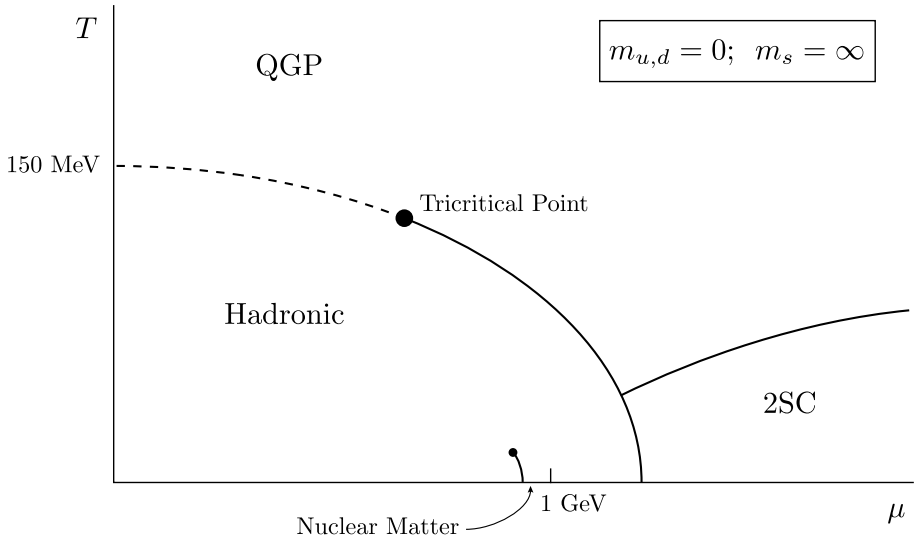

Figure 1.1: Theoretical phase diagram of nuclear matter for two massless quarks and one heavy quark as a function of temperature and baryon chemical potential [6].

teraction, hard probes propagate through, and can be modified by, the medium. High p_T particles from jets and particles containing heavy quarks are hard probes.

- Electromagnetic probes
  Leptons and photons created in the medium leave the medium with very little final state interaction due to their long mean free path. As such, they carry direct information about the properties of the medium that lead to their creation. The main probes in this class are dilepton pairs and direct photons.

This thesis focuses on the measurement of hadrons containing open heavy flavor, that is, a non-zero number of heavy quarks minus heavy antiquarks (one heavy quark, the rest light quarks). That these hadrons are indeed hard probes is demonstrated in Figure 1.2, which shows the yield of "non-photonic" electrons in Au+Au and p+p collisions per the number of binary nucleon-nucleon collisions N_{coll}, as a function of N_{coll} [7]. The "non-photonic" electrons are thought to come from the decays of mesons with open heavy flavor. Since open heavy flavor is a hard probe, the medium-modification of its production will be sensitive to properties of the medium created at RHIC. As the heavy

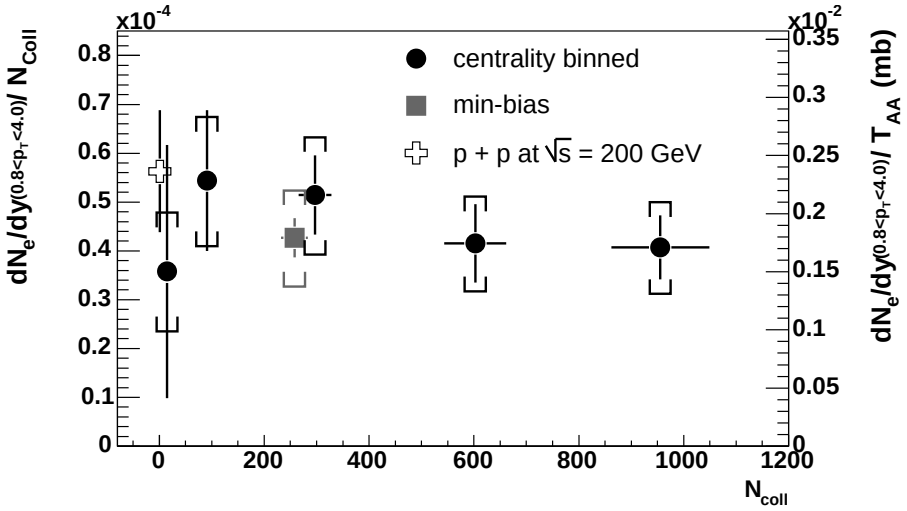

Figure 1.2: Non-photonic electron yield (0.8< p_T <4.0 GeV/c) measured in Au+Au reactions 200 GeV scaled by the number of binary collisions N_{coll} [7]. The yield in p+p collisions is also shown.

flavor decays occur after the medium has dispersed, modification to the electron spectra directly reflects modification of the heavy flavor particles, and not a modification of decay kinematics due to the medium. In principle heavy flavor can also be measured through direct reconstruction of meson decays, such as $D \rightarrow K\pi$, but the lack of primary vertex reconstruction at RHIC experiments makes such a measurement difficult, and so we focus on the indirect measurement of heavy flavor through semi-leptonic decays. There are three main channels through which to measure medium effects on open heavy flavor hadrons:

- Suppression of high p_T particles: energy loss
  QCD predicts that quarks and gluons lose energy as they propagate through dense matter. One way to study this energy loss of partons through the medium created in heavy ion collisions at RHIC is to compare the yield of particles observed from p+p collisions to the yield observed from Au+Au collisions, as a function of (transverse) momentum.

- Azimuthal anisotropy of particle production
  In mid-central (not head-on) heavy ion collisions, the initial geometry of the created medium is spatially asymmetric. In hydrodynamical models, "elliptic flow" caused by a pressure gradient gives rise to an azimuthally

asymmetric distribution of particle production. Such an asymmetric distribution provides evidence of thermalization of the medium, and hints that the matter is strongly coupled.

- Dilepton production in the charm mass region
  If the charm quarks are modified in the medium, then the mass spectrum of correlated $e^{\pm}$ pairs from the simultaneous semi-leptonic decays of $c\bar{c}$ pairs produced in the initial hard-scattering will also be modified.

In this thesis, the analysis of the medium modification of the single electron spectra from heavy flavor decays in Au+Au collisions at $\sqrt{s_{NN}}$=200 GeV will be detailed. The measurement of the azimuthal anisotropy of electrons from heavy flavor decays is also presented. The dilepton spectra will be shown in conjunction with the single electron spectra to facilitate discussion of the results. But before we detail the analysis, we give a brief history of predictions for medium modification of open heavy flavor.

1.2 Expectations for Heavy Flavor

Quantitative predictions for medium modification of electrons from heavy flavor decays in collisions at RHIC date back to dilepton predictions from Shuryak [8]. In this paper, Shuryak refutes a prediction from Gavin *et al.* [9] that the invariant mass spectrum of dileptons is dominated by semileptonic correlated charm quark decays. Shuryak argues that energy loss of heavy quarks from gluon radiation suppresses the dileptons from charm decays such that above invariant mass of 2 GeV, the background from correlated charm decays is smaller than the spectrum from true dileptons.

The energy loss model adopted in this paper is known as BDPS [10], which is a model of radiative energy loss for infinite matter. BDPS was later extended to BDMPS [22], which took finite matter effects into account. The medium modification of the single electron spectra from heavy-flavor decays would later also be calculated within the BDMPS framework. But first came the measurement of light hadron suppression at RHIC, and the associated predictions. The suppression of high p_T light hadrons is important to the history of predictions for heavy flavor, and we disuss it in the next subsection.

1.2.1 Jet Suppression Measurements at PHENIX

To study the effects on partons as they propagate through the medium, we need a probe that is created at the earliest stages of the collision, and is sensitive to the medium properties. Energetic partons from hard scattering should provide

such a probe. Particles with transverse momentum (p_T) greater than 2 GeV/c should come almost entirely from initial hard scattering of the Au nuclei.

Although energy loss of hard-scattered partons could be a signature of a deconfined medium, it has also been argued that the energy loss is only sensitive to the unscreened color charge density, and not necessarily to deconfinement [10, 11, 12]. Nevertheless, jet suppression is an important piece of the experimental puzzle at RHIC. In the remainder of this subsection, the PHENIX data pertaining to suppression of high p_T light hadrons will be shown.

Nuclear Modification Factor: R_{AA}

In the absence of modification from either initial or final state effects, the production of hard-scattered particles from heavy ion collisions should be given by the p+p cross section for that production, scaled by T_{AB}, where T_{AB} is the integral of the product of nuclear thickness over the geometrical region of the colliding nuclei. For hard-scattering, the p+p invariant differential cross section should be given by pertubative QCD (pQCD),

$$E\frac{d^3\sigma}{d^3p} = \frac{1}{p_T^n}F(x_T) \tag{1.1}$$

where $x_T = 2p_T/\sqrt{s}$, and $F(x_T)$ is a function which depends only on x_T. In leading order pQCD, n is equal to 4. Figure 1.3 shows that the invariant differential cross section of π^0 production from PHENIX agrees well with next-to-leading-order (NLO) pQCD predictions for $p_T > 2$ GeV/c. Note that this measurement was taken with the PHENIX central arms, which correspond to a pseudorapidity of $|\eta| < 0.35$. Figure 1.4 shows the PHENIX π^0 invariant yield in central and peripheral collisions compared to the p+p cross section, scaled by T_{AB}. The error bands on the p+p data in Figure 1.4 include both the systematic error on the p+p data points and the uncertainty in T_{AB}. The figure demonstrates that the π^0 from central Au+Au are suppressed with respect to the yields expected from scaling with the number of hard binary collisions. The peripheral yields, however, do not show any suppression, indicating, though not proving, that the suppression in central collisions is a final-state effect of the medium.

To show more precisely the suppression of high p_T pions, we define the nuclear modification factor, R_{AA}, as

$$R_{AA} \equiv \frac{dN_{AA}}{T_{AB} \times d\sigma_{pp}} = \frac{dN_{AA}}{\langle N_{coll}\rangle \times dN_{pp}} \tag{1.2}$$

where dN_{AA} is the differential yield of particles in a nucleus-nucleus (Au+Au)

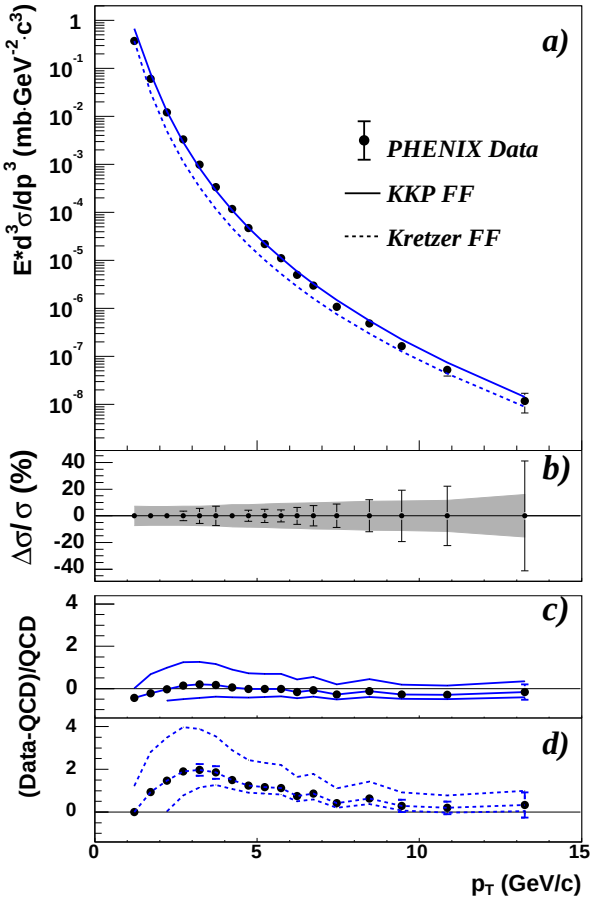

Figure 1.3: PHENIX π^0 invariant cross section at mid-rapidity from p + p collisions at $\sqrt{s} = 200$ GeV, together with NLO pQCD predictions [13, 14]. a) The invariant differential cross section for inclusive π^0 production (points) and the results from NLO pQCD calculations with equal renormalization and factorization scales of p_T using the "Kniehl-Kramer-Pötter" (solid line) and "Kretzer" (dashed line) sets of fragmentation functions. b) The relative statistical (points) and point-to-point systematic (band) errors. c,d) The relative difference between the data and the theory using KKP (c) and Kretzer (d) fragmentation functions with scales of $p_T/2$ (lower curve), p_T, and $2p_T$ (upper curve). In all figures, the normalization error of 9.6% is not shown [15].

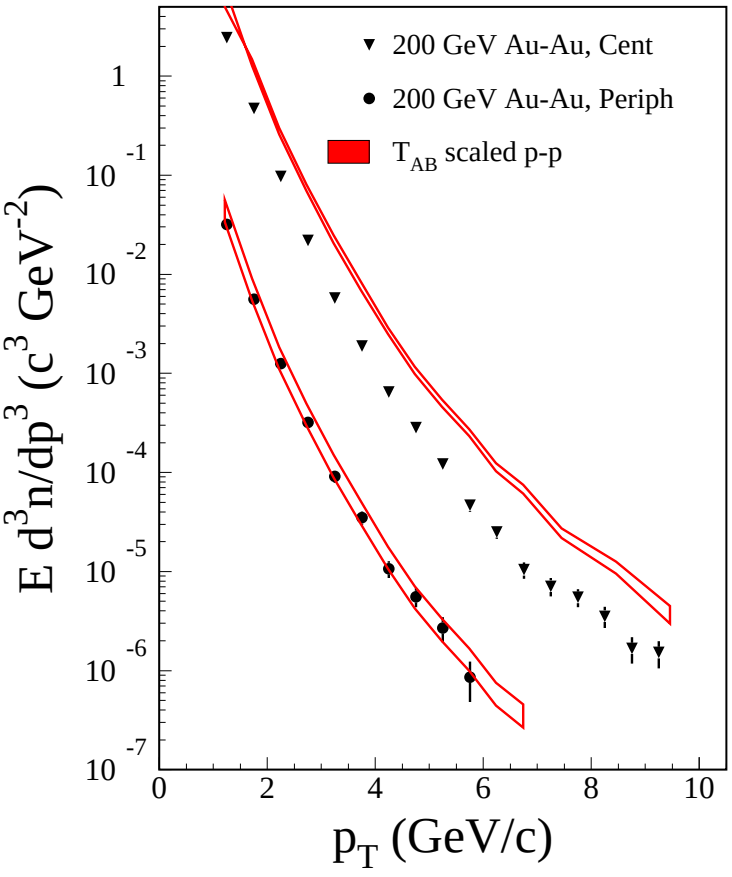

Figure 1.4: π^0 p_T spectra in 200 GeV Au+Au collisions [69] compared to T_{AB} scaling of the 200 GeV p+p cross section (see Figure 1.3). The central data correspond to a 0-10% centrality selection, while the peripheral data correspond to 80-92%.

collision, $d\sigma_{pp}$ is the differential cross section for particle production in a nucleon-nucleon (p+p) collision, and $\langle N_{coll} \rangle$ is the average number of binary nucleon-nucleon inelastic collisions in a nucleus-nucleus collision, for a given centrality. Figure 1.5 shows the R_{AA} of π^0 for central and peripheral Au+Au collisions at $\sqrt{s_{NN}} = 200$ GeV/c. In addition, Figure 1.5 also shows the R_{AA} from d+Au collisions, as a test of the contribution to the suppression in Au+Au collisions from initial-state nuclear effects. The d+Au R_{AA} demonstrates that there is no significant initial-state contribution to the Au+Au R_{AA}. The data do suggest a slight enhancement in d+Au collisions, consistent with expectations due to the Cronin effect [17].

Figure 1.6 shows the R_{AA} as a function of p_T and centrality for inclusive charged particles from Au+Au collisions at PHENIX. For $p_T > 4.5$ GeV/c, the R_{AA} is flat, just as for the π^0 R_{AA}, and shows a similar suppression. For intermediate p_T the charged particles are suppressed less than the π^0. This effect is related to contributions from baryons, which are enhanced relative to the charged mesons [19].

Given that high-p_T hadrons are suppressed in central Au+Au collisions, what quantitative statements can we make about the medium? Clearly there is a dense colored matter produced. To demonstrate the sensitivity of the light-hadron suppression to properties of the medium, we compare here to a model based on BDMPS [20] which calculates suppression of hadrons from energy-loss due to gluon radiation from partons, as a function of the transport coefficient $\hat{q} = \langle q_T^2 \rangle / \lambda$, the average squared transverse momentum transferred to the parton per unit pathlength. It is assumed that multiple gluons are radiated independently from a given parton. Figure 1.7 shows the model prediction for R_{AA} compared to various values of $\hat{q}$. As $\hat{q}$ goes above 5 GeV^2/fm, the nuclear modification factor becomes insensitive to the value of the transport coefficient. This is largely due to particle emission from the surface region of the medium, which remains mostly unsuppressed regardless of the overall density. This insensitivity of the light hadron spectra to the medium density is one motivation to study the spectra of open heavy flavor hadrons, since the heavy flavor hadrons are predicted to lose less energy than light hadrons from gluon radiation due to the "dead-cone" effect [21], a mass-dependent reduction of the available phase space for radiation of a gluon.

Another approach to radiative energy loss by Gyulassy *et al.* [23], denoted GLV, predicted the constant R_{AA} of the π^0 from an interplay between the Cronin effect, nuclear shadowing, and jet quenching at RHIC. In this model, unlike the BDMPS model, there is no surface emission bias limiting the sensitivity of the model at high densities. The main parameter in the GLV model is the gluon density per rapidity, dN_g/dy. The π^0 R_{AA} is well described with

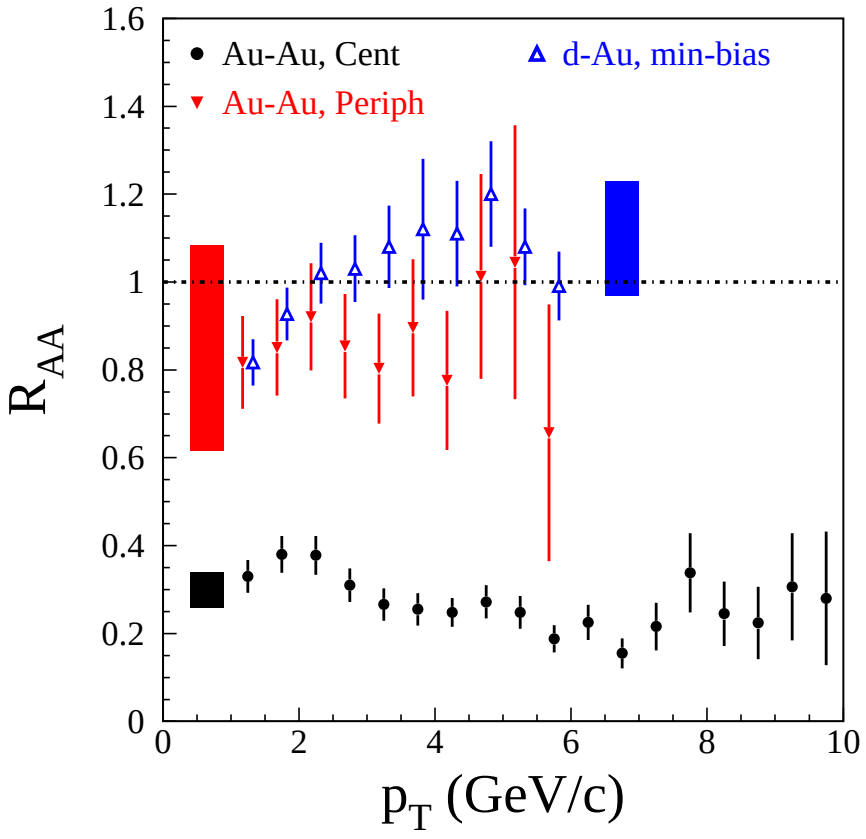

Figure 1.5: R_{AA} for π^0 for central (0-10%) and peripheral (80-92%) collisions [69] and for minimum-bias d+Au collisions [16]. The shaded boxes show normalization errors resulting from systematic error in the R_{AA} and uncertainty in T_{AB}.

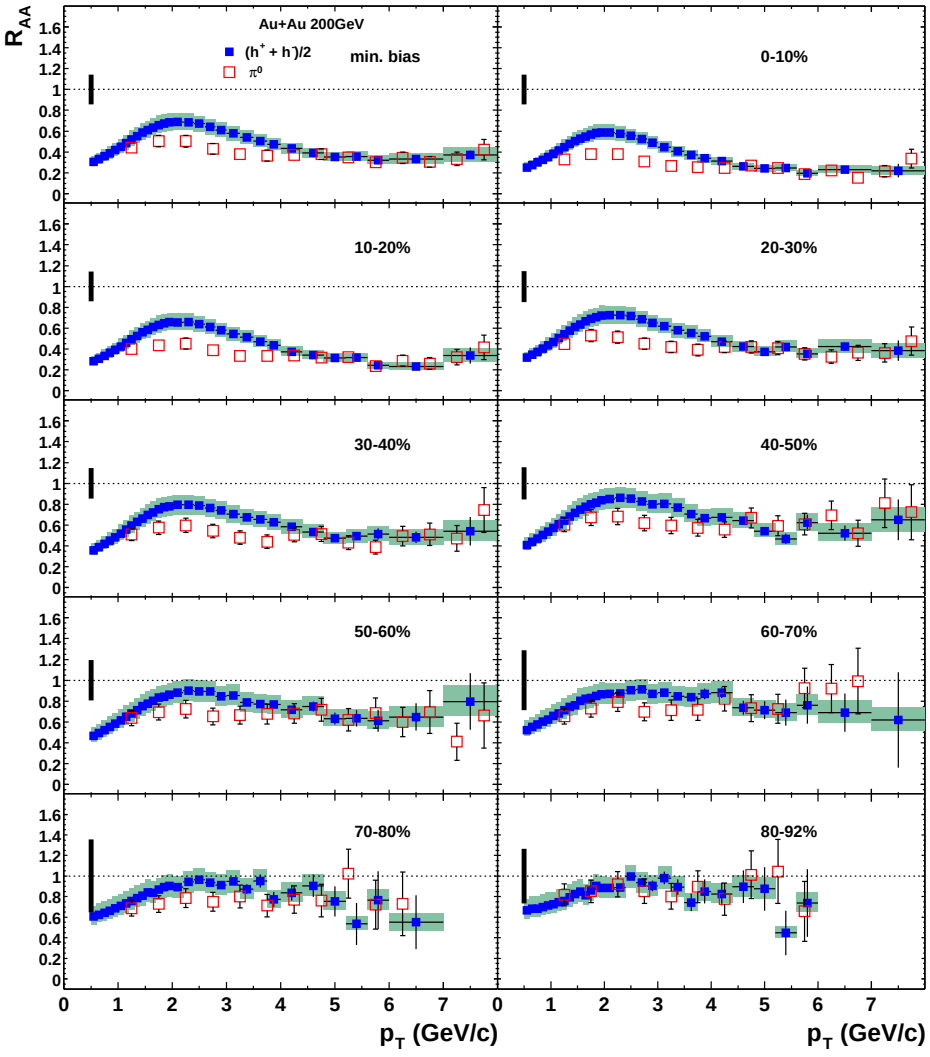

Figure 1.6: Centrality and p_T dependence of charged particle R_{AA} [18]

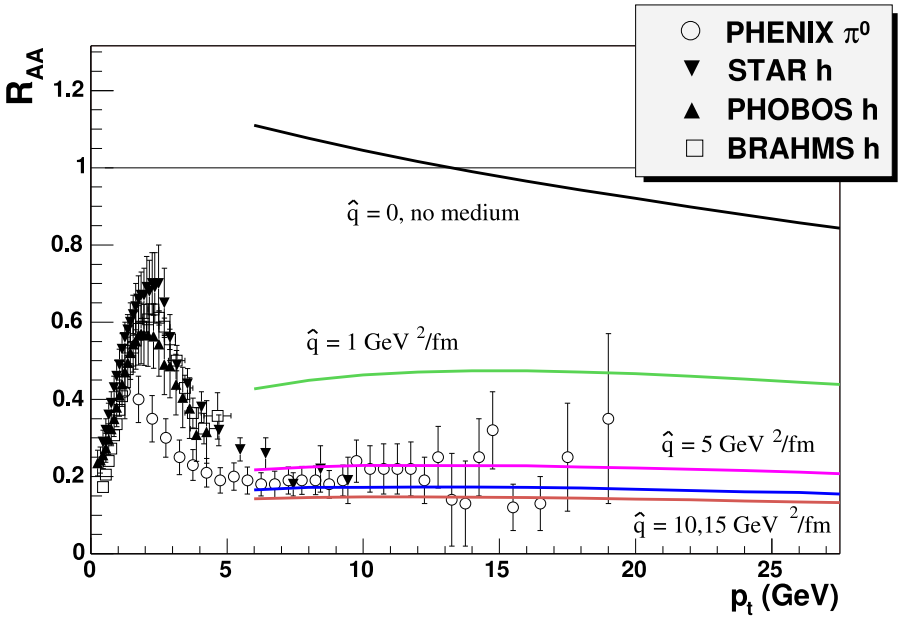

Figure 1.7: Gluon-radiation model predictions from [20] for various values of $\hat{q}$ together with hadron R_{AA} data from the RHIC experiments.

dN_g/dy ∼800-1200. Figure 1.8 shows the GLV model predictions for π^0 R_{AA} at SPS, RHIC, and LHC.

To further scrutinize these models for radiative energy loss, they must be compared to other observables. The single electron spectra from semileptonic decays of open heavy flavor hadrons serves as a valuable complementary observable.

Azimuthal Anisotropy: v_2

In non-central collisions of heavy ions, the distribution of colliding matter is not isotropic around the beam direction. As such, the spatial distribution of particles leaving the produced matter can also be anisotropic. Indeed, in the thermodynamic limit, the asymmetric distribution of initial energy density causes a pressure gradient which is largest in the shortest direction of the ellipsoidal medium.

To quantify the azimuthal anisotropy of the yield, we make a Fourier expansion

$$\frac{dN}{d(\phi - \Psi)} = N_0(1 + 2v_2\cos(2(\phi - \Psi))) \tag{1.3}$$

where ϕ is the azimuthal angle of the measured particle, and Ψ is the angle of the "reaction plane", that is, the direction between the centers of the colliding nuclei. In Equation 1.3, the first order Fourier coefficient v_1 is ignored due to symmetry reasons. Although we expect the anisotropy to be dominated by the elliptic flow from the pressure gradient in the thermodynamic limit, even if higher order Fourier coefficients were important in the expansion, they would be washed out in the measured anisotropy due to the finite resolution of the reaction plane [26], and so terms of order higher than 2 are also ignored. Figure 1.9 shows v_2 for pions, kaons, and protons compared to a hydrodynamical calculation.

Prior to the analysis which is the topic of this thesis, azimuthal anisotropy from heavy flavor had been measured, but with low precision [28]. The prediction from theory was that the v_2 of the D meson, and of the electrons from semileptonic decays of D mesons, would be significantly smaller due to the mass of the charm quark, and due to the large mass difference between the charm quark and the corresponding light quark in the meson [41, 43].

1.2.2 Initial measurements of open heavy flavor at RHIC

Prior to the analysis of PHENIX data which is the focus of this thesis, PHENIX had published the centrality and p_T dependence of non-photonic single electron spectra from Au+Au collisions from RHIC Run 2 [29], and STAR had released

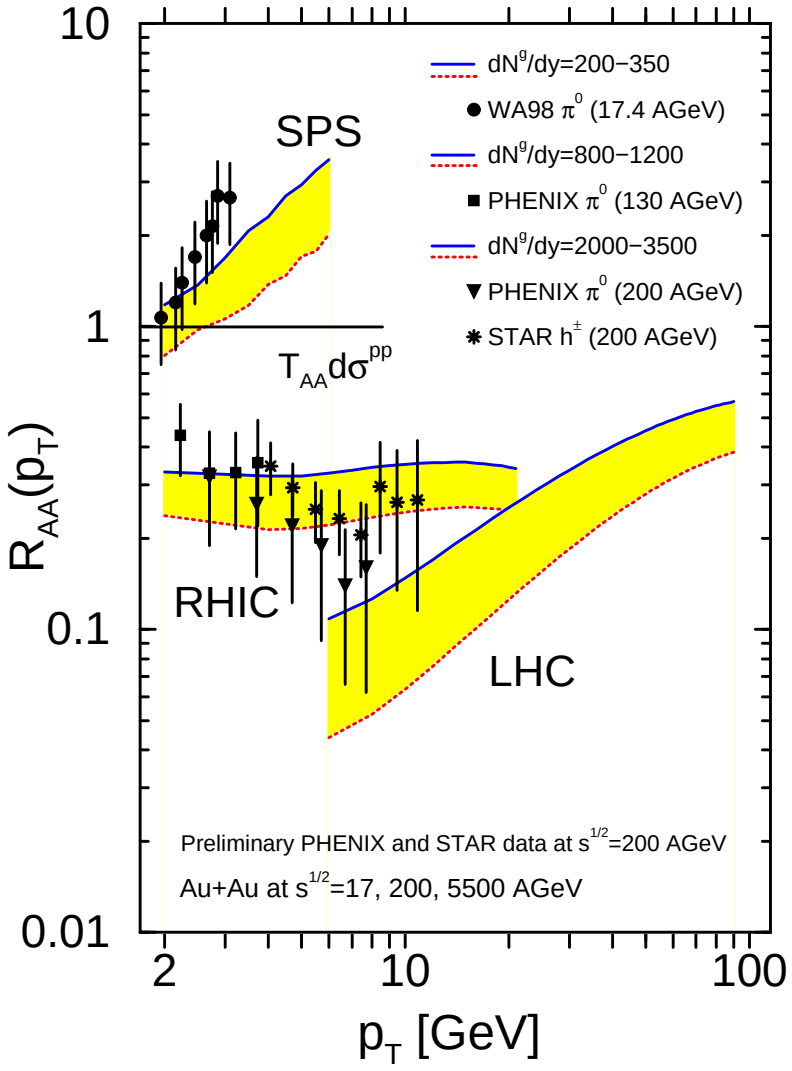

Figure 1.8: Gluon-radiation model predictions from the GLV model [23].

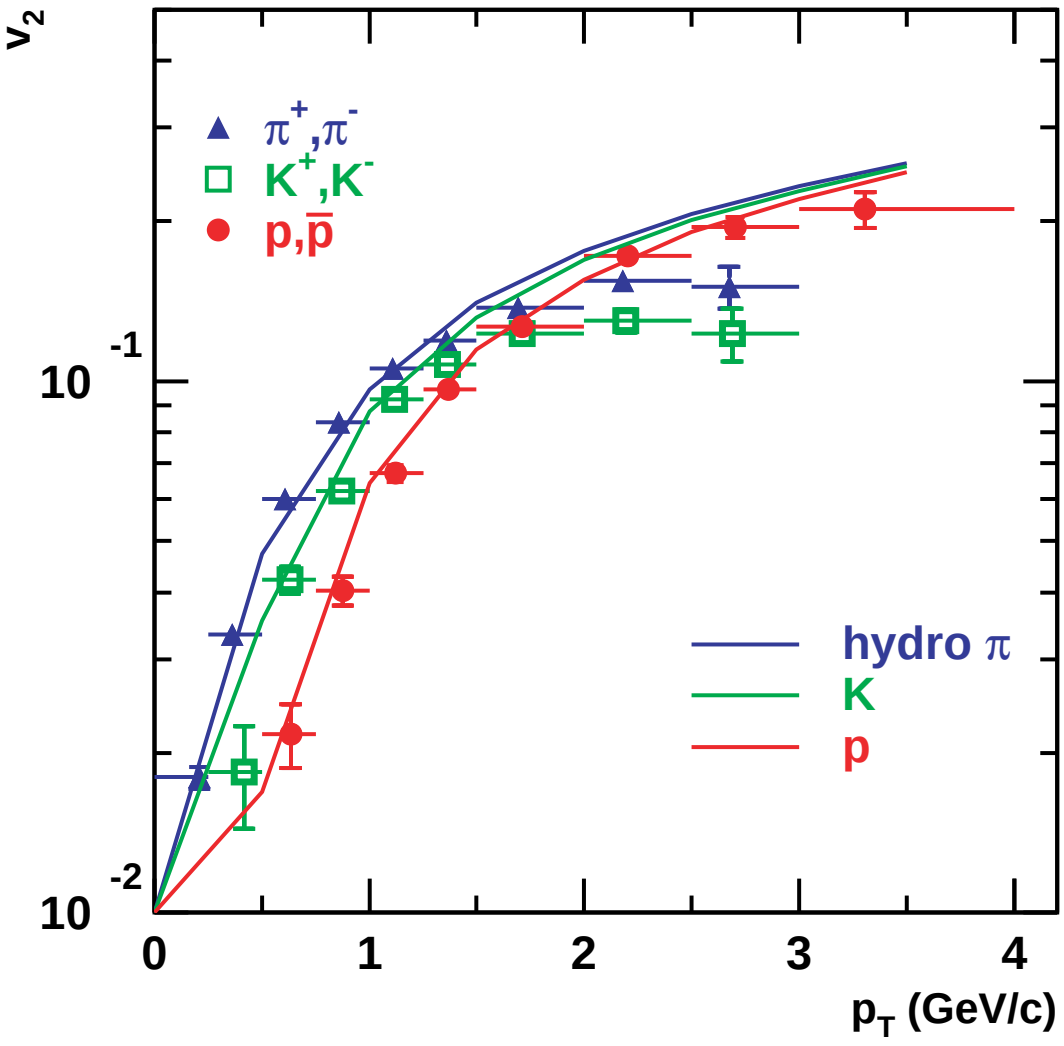

Figure 1.9: v_2 as a function of p_T for pions, kaons, and protons from minimum-bias Au+Au collisions [24], compared to ideal hydrodynamical calculations from [25].

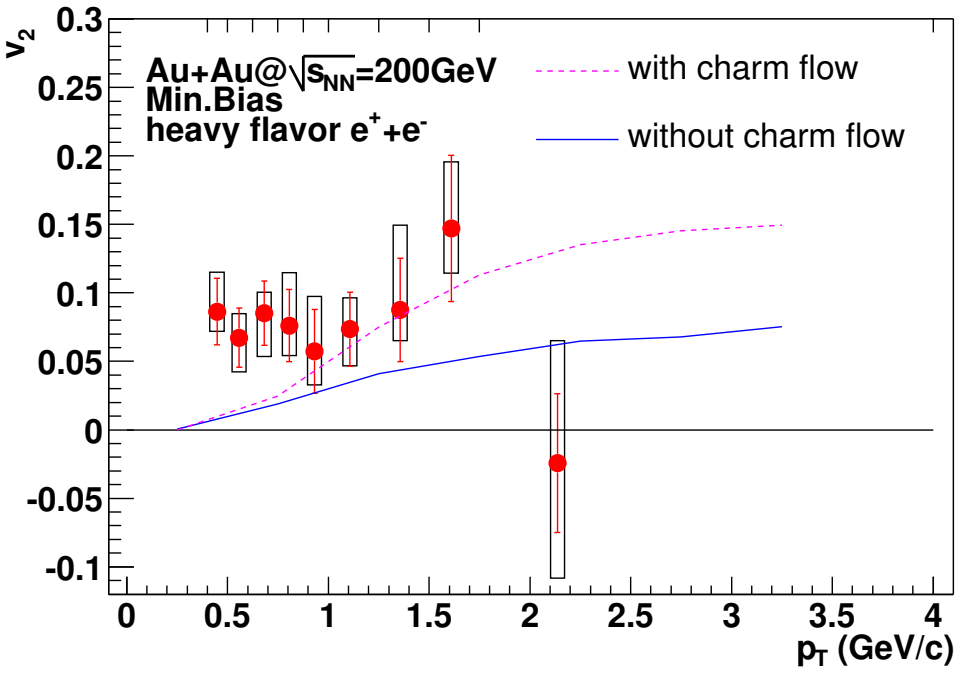

Figure 1.10: Heavy flavor electron v_2 [28] with charm flow scenarios from [43]

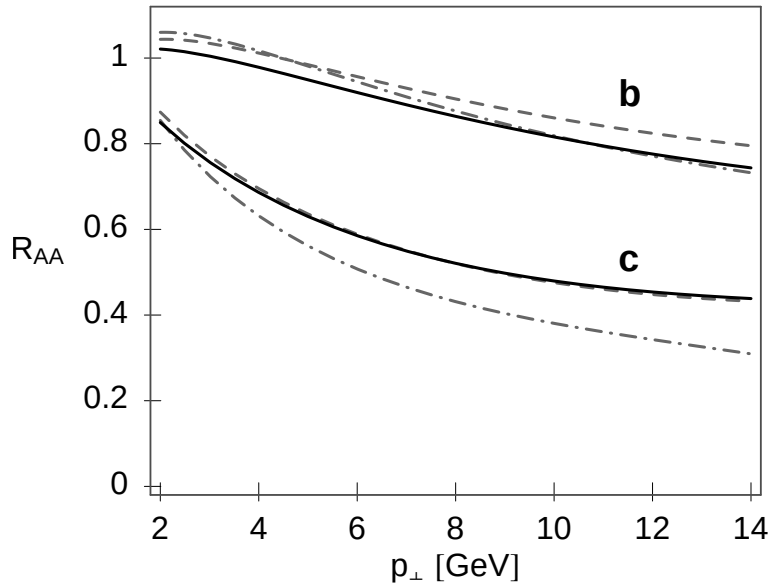

Figure 1.11: DGLV prediction of R_{AA} for charm and bottom quarks [31].

preliminary results from RHIC Run 4 Au+Au collisions. Prior to these analyses, charm electron R_{AA} had been measured from Au+Au collisions at 130 GeV/c [7]. Heavy flavor electrons from p+p collisions from Run 3 had been measured [44] by PHENIX, and STAR had measured charm production in p+p and d+Au collisions through semileptonic decays and through reconstruction of $D^0(\overline{D^0}) \rightarrow K^{\mp}\pi^{\pm}$ decays [45]. The prediction of R_{AA} versus p_T for charm and bottom quarks (before the electron decays) by Djordjevic et.al. using an extension to the GLV model, denoted DGLV, is shown in Figure 1.11. The BDMPS model calculations for the heavy-flavor electron R_{AA} using similar values of $\hat{q}$ as those which describe the light hadron R_{AA} are plotted along with the Run2 PHENIX and Run4 Preliminary STAR data in Figure 1.12. Figure 1.13 shows the DGLV prediction for the single electron R_{AA}. As can be seen from Figures 1.12-1.13, there is indication from the PHENIX and STAR single electron data that the BDMPS and DGLV models underpredict the level of suppression of charm and bottom quarks in the medium. The DGLV model was extended to include energy loss from elastic scattering as well, but still it seems to underpredict the R_{AA}. However, the statistical and systematic errors on the data shown in Figures 1.12-1.13 are large, and do not completely rule out the BDMPS or DGLV models. Also, the radiative energy loss models are expected to work at high p_T where pertubative QCD calculations can be

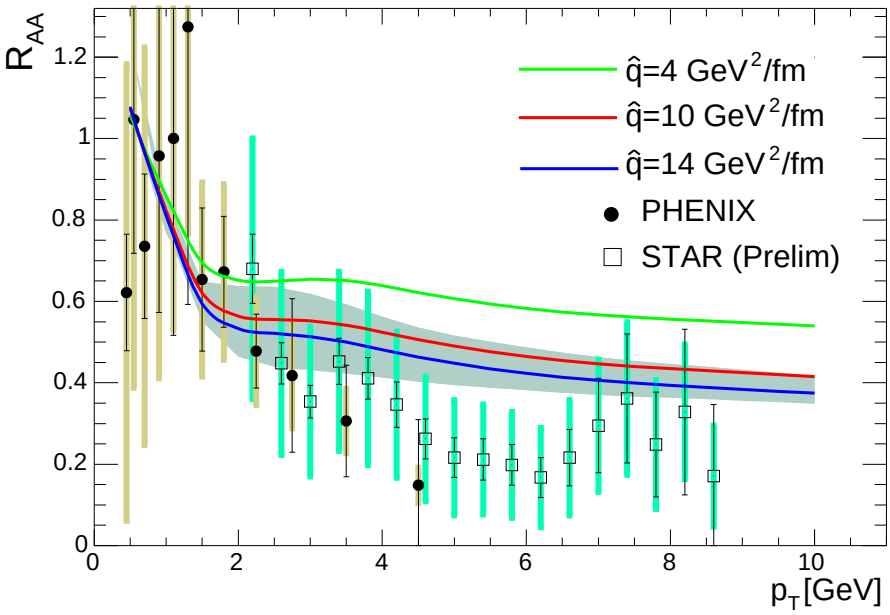

Figure 1.12: Single electron R_{AA} from central Au+Au collision from PHENIX and STAR along with BDMPS model predictions [32].

trusted, but are probably less accurate as momentum decreases. The analysis which is the topic of this thesis extends the PHENIX measurement to higher p_T with greatly reduced systematic and statistical errors.

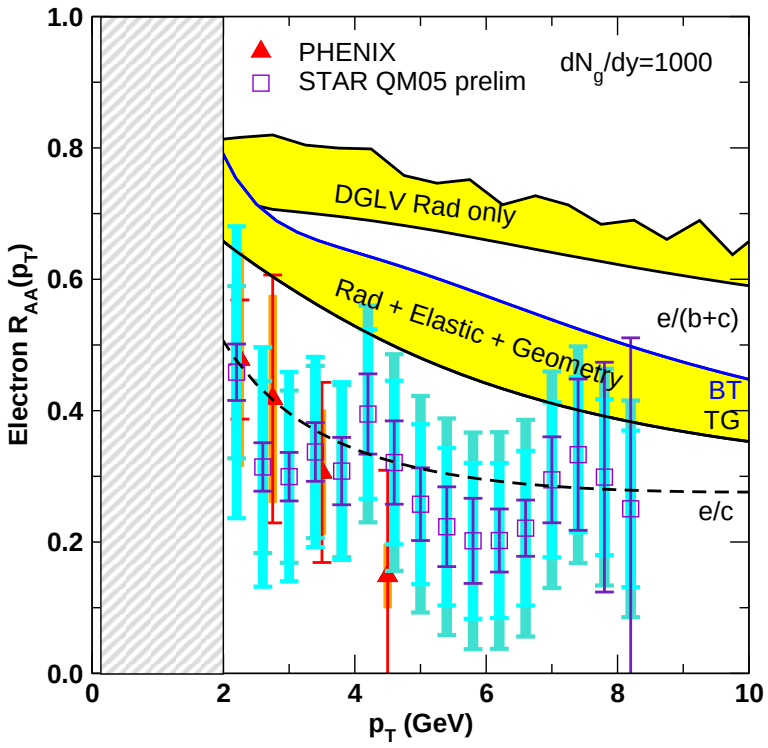

Figure 1.13: DGLV prediction of R_{AA} for single electrons from heavy flavor [33], with and without contribution from elastic scattering.

Chapter 2

PHENIX Experiment

2.1 Detector Overview

PHENIX (Pioneering High Energy Nuclear Interaction eXperiment) is an advanced detector system, consisting of 11 independent detector subsystems, capable of collecting information about the particles produced in heavy ion collisions. Charged particles (electrons and hadrons at mid-rapidity, and muons at forward rapidity) are measured in a large momentum range with the PHENIX tracking system. In addition, the Electromagnetic Calorimeter provides measurement of photons. Figure 2.1 shows the PHENIX experimental setup in Run4. The setup consists of 4 spectrometer arms as well as global detectors. The spectrometer arms at mid-rapidity are called the central arms, and the spectrometer arms at forward rapidity are called the muon arms. Table 2.1 [34] summarizes the subsystems installed and active in Run4. The global detectors, the BBC and ZDC, provide collision time, collision vertex position, and centrality measurement as well as serving as event triggers. The central arms provide momentum, energy, and particle identification for charged tracks as well as energy measurement of photons. The two central arms each cover ± 0.35 units of pseudorapidity and 90° in azimuthal angle around the beam direction. The drift chambers measure charged particle trajectories in the $r - \phi$ plane, while the first layer of the pad chambers (PC1) supplement the drift chamber tracking with a 3-D point along the straight line projection of the track. The ring-imaging Cherenkov detectors (RICH) are the primary detectors for electron identification, and lie behind the first layer of the pad chambers. Beyond the RICH sits the Electromagnetic Calorimeter, which measures the energy of electrons and photons, and gives further spatial information for charged tracks. Together, the RICH and the EMCal gives a $\pi^{\pm}/e^{\pm}$ separation of better than one part in 10^4 for p <4.7 GeV/c [34]. The time-of flight detector, which

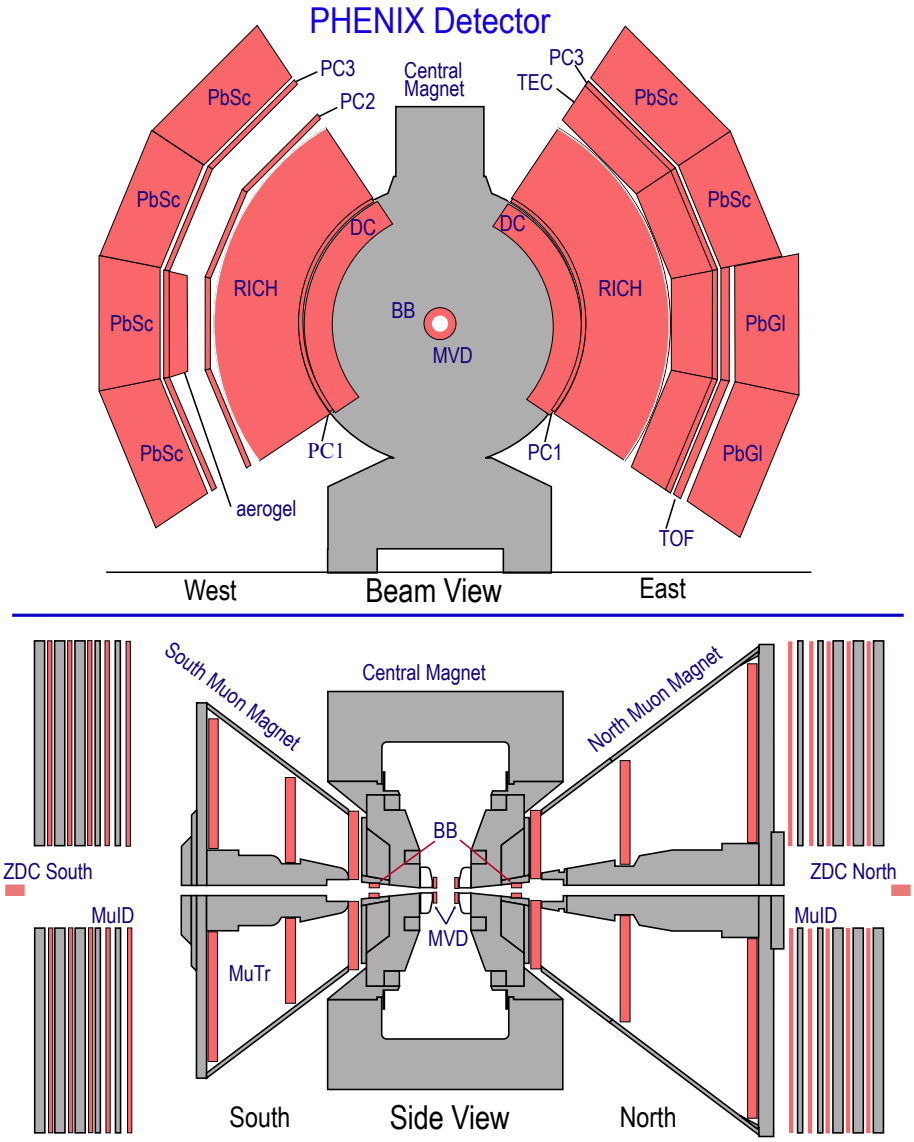

Figure 2.1: Schematic of the PHENIX experimental setup in the 2004 Au+Au run (Run4). Top: Cross section of central arms perpendicular to the beam pipe. Bottom: View from the east side with the beam pipe spanning the horizontal direction.

Component	$\Delta\eta$	$\Delta\phi$	Purpose/features
Magnet: central	± 0.35	360°	Up to 1.15 T·m
muon south	-1.1 to -2.2	360°	0.72 T·m for $\eta = 2$
muon north	1.1 to 2.4	360°	0.72 T·m for $\eta = 2$
Beam-beam counters (BBC)	± 3.1 to 3.9	360°	Start timing, fast vertex
Zero-degree Calorimeter (ZDC)	± 2 mrad	360°	Minimum-bias trigger
Drift Chambers (DC)	± 0.35	$2 \times 90°$	Good momentum and mass resolution, $\Delta m/m = 0.4\%$ at $m = 1GeV$
Pad chambers (PC)	± 0.35	$2 \times 90°$	Pattern recognition tracking in non-bend direction
Time Expansion Chamber (TEC)	± 0.35	90°	Pattern recognition, dE/dx
Ring-Imaging Cherenkov Detector (RICH)	± 0.35	$2 \times 90°$	Electron identification
Time-of-flight (TOF)	± 0.35	45°	hadron ID, σ <100ps
PbSc EMCal	± 0.35	$90° + 45°$	electron/photon ID
PbGl EMCal	± 0.35	45°	Good $e^{\pm}/\pi^{\pm}$ separation at p >1 GeV/c by EM shower and p <0.35 GeV/c by TOF. $K^{\pm}/\pi^{\pm}$ separation up to 1 GeV/c by TOF
μ tracker: south	-1.15 to -2.25	360°	μ tracking
north	1.15 to 2.44	360°	μ tracking
μ ID: south	-1.15 to -2.25	360°	μ/hadron separation
north	1.15 to 2.44	360°	μ/hadron separation

Table 2.1: Summary of PHENIX subsystems [34].

rests between the RICH and EMCal in the east arm only, provides charged hadron identification. The two muon arms measure muon and decay hadrons

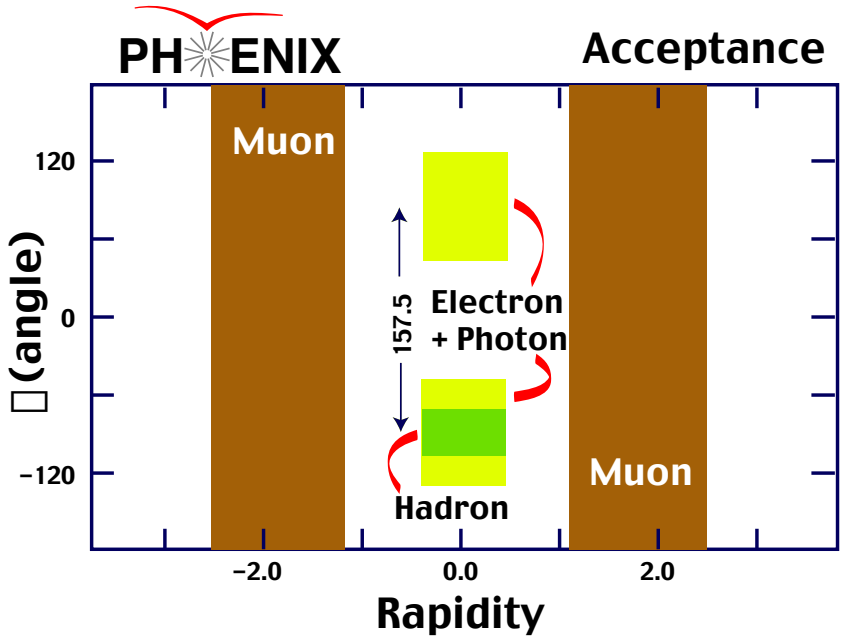

Figure 2.2: PHENIX acceptance for electrons, muons, photons, and hadrons in Run4.

at forward and backward rapidity (see table 2.1).

2.2 Global Detectors

2.2.1 Beam-Beam Counters

The purpose of the beam-beam counters (BBC) is to provide the time at which a collision takes place, to produce a signal on which to trigger data collection, to measure the position of a collision, and to determine the centrality of a collision along with the zero-degree calorimeter (ZDC). The BBC is also used to determine to reaction plane, or orientation of the impact parameter in a collision. The BBC consists of three rings of quartz Cherenkov detectors, which measure fast-moving charged particles produced in a small cone around the beam axis in either direction. Each BBC is positioned 1.4m along the beam direction from the center of PHENIX, and has an outer radius of 30cm and

an inner radius of 5 cm. Each counter consists of 64 photo-multiplier tubes

(a) (b)

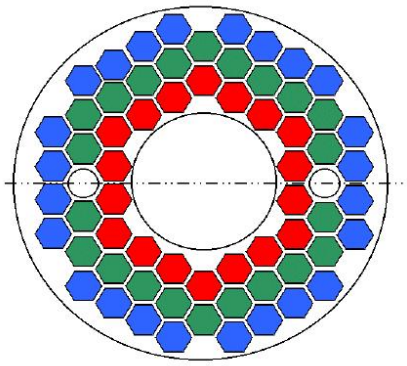

(c)

Figure 2.3: (a) Picture of the 64 PMTs comprising the BBC array. (b) BBC element consisting of one inch mesh dynode PMT mounted on a 3 cm quartz radiator. (c) Schematic of the BBC, with each box corresponding to a PMT.

(PMT) mounted on quartz Cherenkov radiators, as shown in Figure 2.3. Each PMT has a dynamic range capable of registering anywhere between 1 and 30 minimum ionizing particles, allowing the BBC to serve in a minimum-bias trigger for any of the collision species used in RHIC.

Each PMT has a timing resolution of 50 ps. The collision vertex can be found by looking at the difference in the average hit time over the PMTs between the north and the south BBC. In p+p collisions, the vertex resolution in the beam direction is 1.2 cm, while in central Au+Au collisions the resolution is 0.3 cm. The PHENIX Level-1 trigger accepts signals if the BBC vertex is within 50 cm of the center of PHENIX, in order to avoid interactions of particles with the magnet poles, scattering particles into the central arm

acceptance. Since this trigger is efficient for most interaction processes, it is referred to as a "minimum-bias" trigger.

2.2.2 Zero Degree Calorimeters

The zero degree calorimeters (ZDC) are hadron calorimeters positioned about 18 m from the center of PHENIX on either side in the direction of the beam axis with the purpose of measuring spectator neutrons from nucleus-nucleus collisions. Charged particles from the collision, such as spectator protons, are bent out of the ZDC acceptance by the DX magnets (see Figure 2.5). The correlation between the energy measured in the ZDC and the charge measured in the BBC is used to determine the centrality of a nucleus-nucleus collision, as seen in Figure 2.4. The centrality is defined such that each 5% centrality bin has an equal number of events.

Each ZDC counter contains 3 modules consisting of tungsten alloy plates with a depth of two hadronic interaction lengths, and each module is read out by a single PMT. The ZDC, like the BBC, also provides timing information, though not as accurately as the BBC. The ZDC is an important part of the minimum-bias trigger in nucleus-nucleus collisions. Figure 2.5 shows a schematic view of the ZDC.

2.3 Central Arm Detectors

2.3.1 Central Magnet

The central magnet is not a detector subsystem, but tracking in the central arms is dependent on a stable magnetic field. The magnet consists of an outer and inner coil inside a steel yolk, generating an axially-symmetric magnetic field in the region around the beam pipe in PHENIX. Figure 2.6 displays the magnetic field lines when both coils are turned on with current with the same helicity. The magnetic field integral for a charged track with both coils energized, with current in the same direction, is $\int \mathbf{B} \cdot d\mathbf{l} = 1.15$ T·m. In the region of the tracking detectors, about 2 m from beam pipe, the magnetic field strength is much smaller to allow for a tracking model which assumes tracks are straight.

2.3.2 Drift Chambers

The Drift Chambers (DC) are the main tracking detectors for PHENIX, each consisting of multiwire gas chambers located between 202 cm and 246 cm in

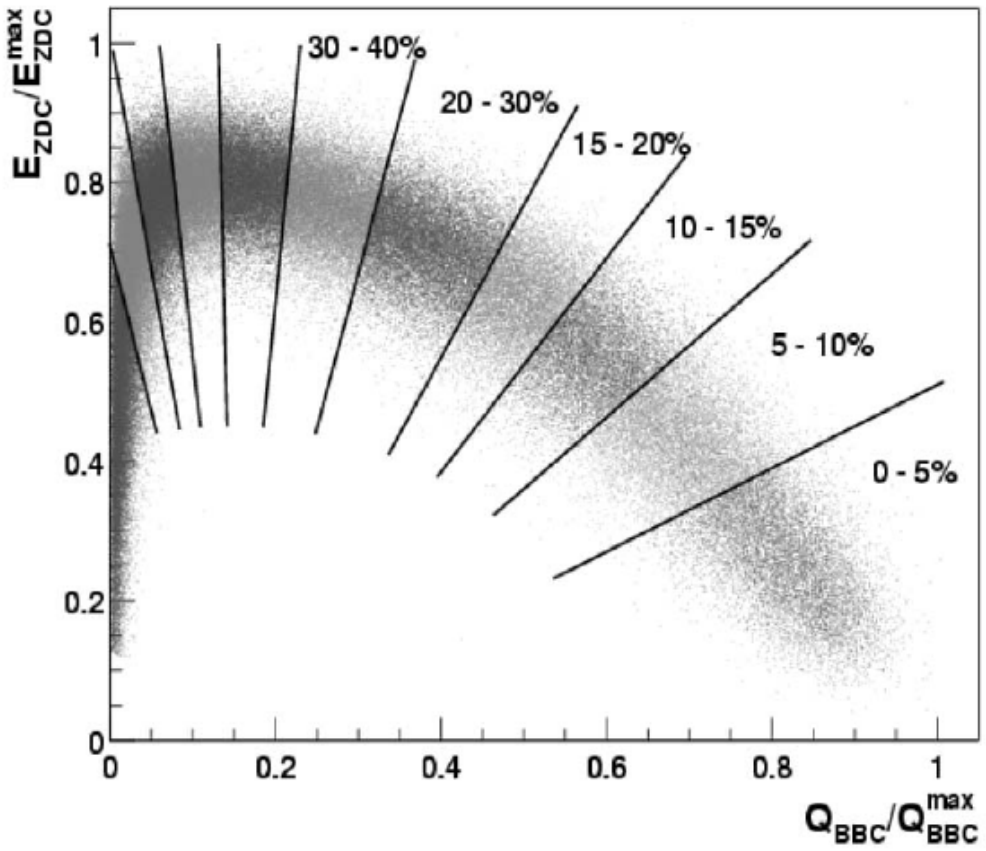

Figure 2.4: Correlation between the BBC measured charge and the ZDC measured energy. The lines show the definition of centrality classes from this correlation.

radius. The drift chambers measure trajectories of charged particles in the $r - \phi$ plane in order to determine the momentum of each particle, and the invariant mass of charged particle pairs. An initial goal of the drift chamber was to measure the mass of the ϕ meson through the $\phi \rightarrow e^+e^-$ channel, with better resolution than the width of the ϕ of 4.4 MeV. This, along with the ability to perform tracking in a high-multiplicity environment, places the following design requirements on the DC [35]

- Single wire resolution better than 150 μm in $r - \phi$
- Single wire two-track separation better than 1.5 mm

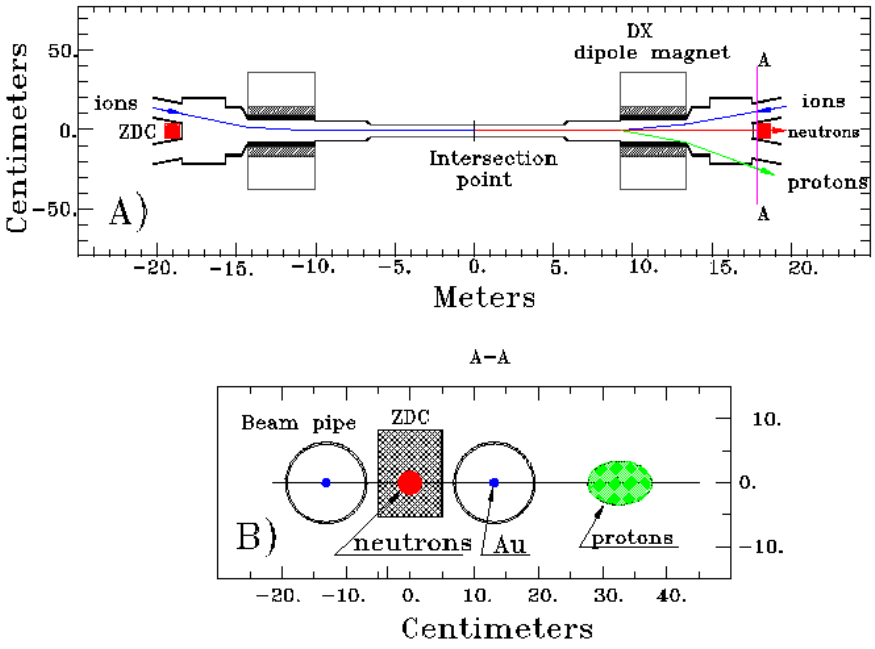

Figure 2.5: top: Schematic top-view of PHENIX interaction region. bottom: Projections of proton and neutron deflection area in the plane of the ZDC.

- Single wire efficiency better than 99%
- Spatial resolution in the beam (z) direction better than 2 mm.

Each arm of the DC consists of a cylindrical titanium frame supporting wire nets with 42 cm in radial width and 180 cm in length. Figure 2.7 shows a schematic view of a drift chamber arm. The active volume of the DC is filled with a 50%/50% mixture of Argon and Ethane gas. The mixture was chosen due to its uniform charge drift velocity, high gain, and low diffusion coefficient. Each arm contains 20 identical keystones covering 4.5° in azimuth. There are six types of wire modules in each keystone, called the X1, U1, V1, X2, U2, and V2, and each wire module contains 4 anode and 4 cathode planes. The X1 and X2 wires run parallel to the beam in order to track in the $r - \phi$ plane. The U,V wires are oriented with about 6° rotation with respect to the X wires, and measure the z-coordinate of the track. In order to allow for pattern recognition with up to 500 tracks, each wire is separated into two electrically isolated halves (in the beam direction) by a 100 μm thick kapton support. The DC contains a total of about 13000 readout channels. In addition to the anode and cathode wires, each plane contains "gate" wires and "back" wires.

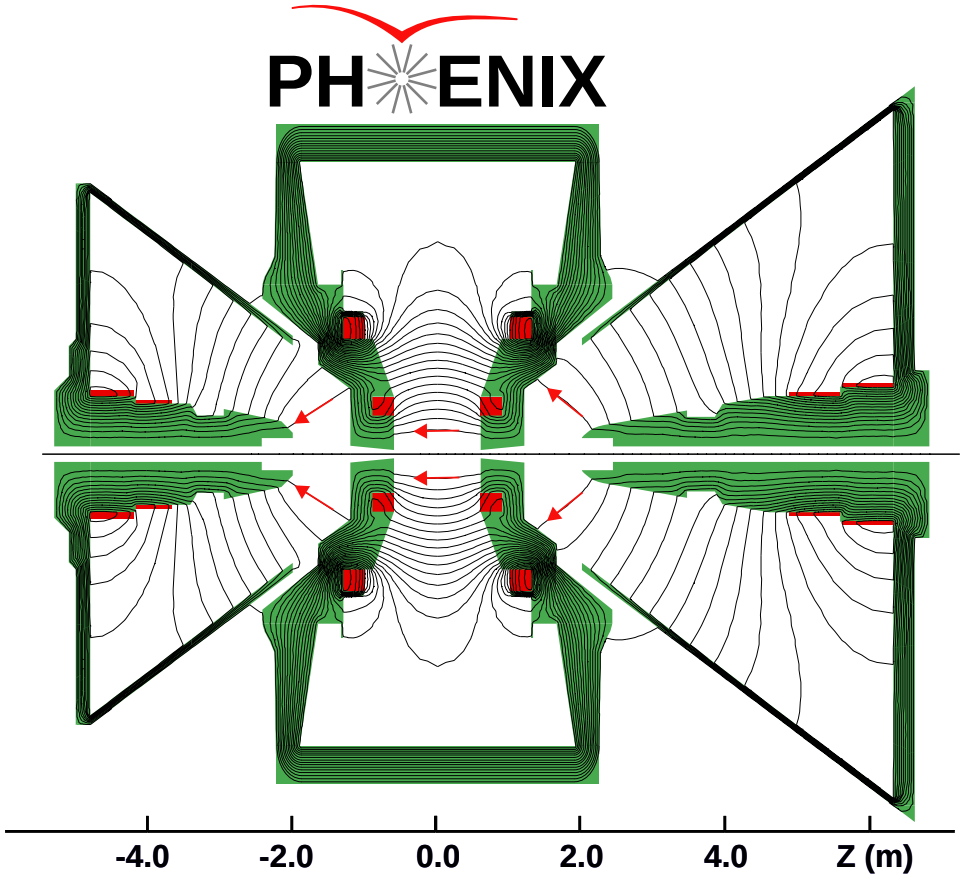

Figure 2.6: Magnetic field lines created by the PHENIX central magnet and muon magnets.

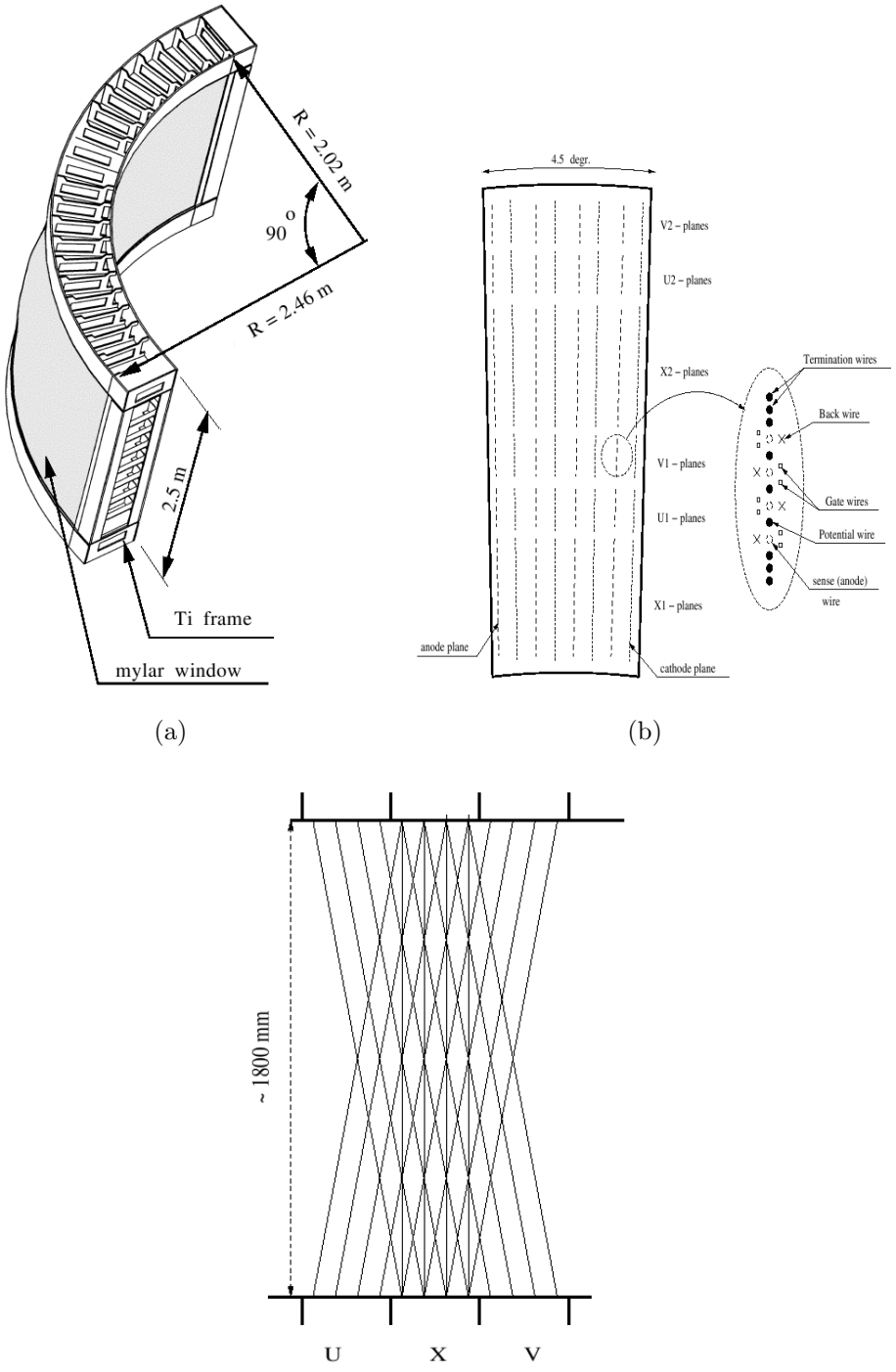

Figure 2.7: (a) Schematic of one arm of the drift chamber. (b) Wire structure of a DC keystone. (c) Top view of the wire orientations.

The gate wires form charge collection regions which limit the track drift length to about 3 mm, reducing the detector occupancy. The back wires contain a low potential to block tracks from one side of the anode, to reduce ambiguity about from which side of the wire the charge had drifted.

Tracking Algorithm

The tracking algorithm using the drift chamber must have a high single track efficiency, while simultaneously being able to perform well in a high multiplicity environment, keeping falsely reconstructed "ghost" tracks to a minimum. A perfect track would deposit 6 hits in both the X1 and X2 sections. The efficiency of each wire varies across channels, but is between 90% and 95% for all wires. If we require tracks to have at least 4 hits in both the X1 and X2 sections, then the single track efficiency is better than 99%. The first stage of the tracking algorithm uses a combinatorial Hough transform [37], assuming the particles have a straight line trajectory inside the drift chamber volume. The ouput of the Hough transform is two angles, ϕ and α, illustrated in Figure 2.8. After the Hough transform is complete, the next step in the algorithm is the removal of background tracks. First, a robust fitting is used to provide tighter contraints on whether a hit is associated with a track. An iterative linear fitting approach is used, weighting hits according to their deviation from the straight line guess for a trajectory. The weighting goes to zero for hits far from the straight line guess so that the fit is not disturbed by hits from noise or other tracks. Finally, it is imposed that each hit can correspond to only a single track. The closest track remaining to a given hit is kept, while the hit is removed from all other associated track candidates. Tracks with fewer than 8 total hits associated are discarded.

The above algorithm only gives track information in the $r-\phi$ plane. If there is a hit in the PC1 (see the next section about the pad chambers) associated with the projection of a track candidate from the X1, X2 section, then the z position of the PC1 hit fixes the track in three dimensions. If there is more than one associated PC1 hit, then the PC1 hit with the most associated hits in the U,V sections of the drift chamber is used.

2.3.3 Pad Chambers

The PHENIX central arms contain three layers of multiwire proportional chambers called the pad chambers. The first layer, PC1, is located just behind the DC in both central arms. PC3 is installed just in front of the EMCal in both arms. PC2 is located behind the RICH in the west arm only. Each chamber contains a single plane of wires inside a gas volume between two cathode

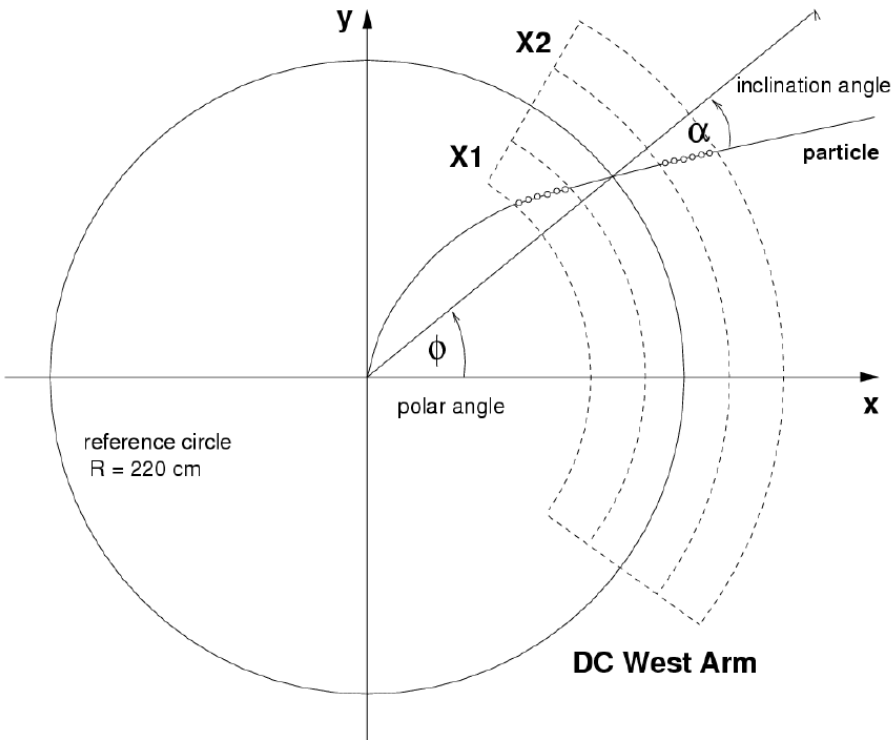

Figure 2.8: Definition of the Hough transform parameters ϕ and α in the DC track reconstruction.

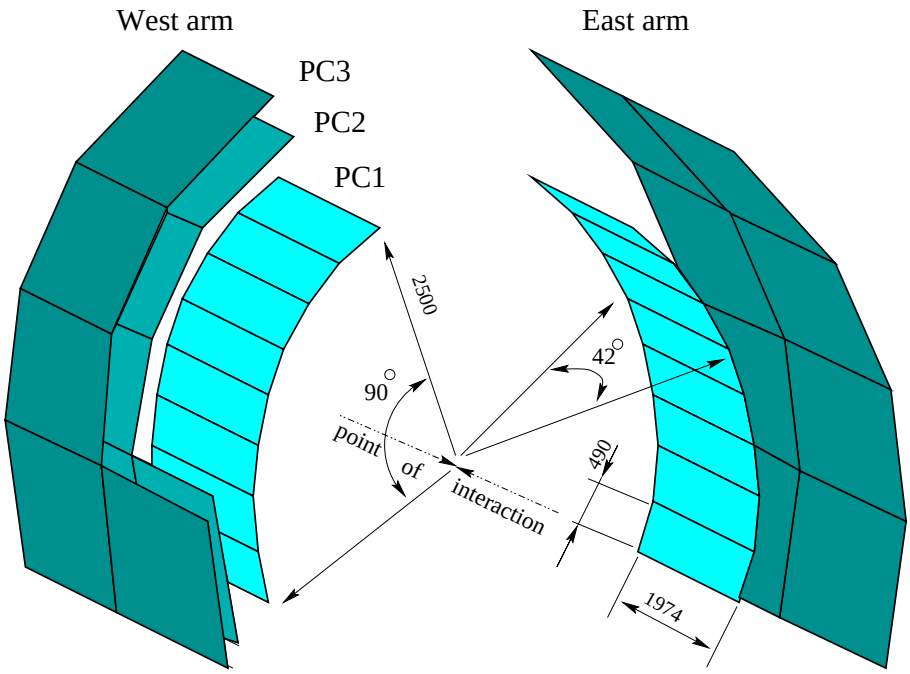

Figure 2.9: Schematic of the PHENIX pad chambers. Some sectors of the PC2 and PC3 sections are removed for clarity.

planes, each of which is segmented into an array of pixels. The basic element of the detector is a "pad" of 9 pixels. The PC measures space points along the straight trajectory of a particle outside of the magnetic field with a resolution of 1.7 mm in the z direction and 2.5 mm in the $r - \phi$ direction. The PC1 measures a point just behind the DC, providing the z-coordinate of a track thus being essential for the reconstruction of the three-dimensional momentum of a particle. Figure 2.9 shows a schematic view of the pad chamber system.

2.3.4 Ring Imaging Cherenkov Detectors

Each of the central arms contains a ring imaging Cherenkov detector (RICH) with the purpose of providing discrimination between electrons and hadrons. The RICH can reject hadrons to better than one part in 10^4 below a momentum of 4.7 GeV/c. For p+p collisions, the RICH also serves as part of a Level-1 trigger for collection of events containing electrons. Figure 2.10 shows a schematic view of the RICH. Each RICH detector has a volume of 40 m^3, entrance window area of 8.9 m^2, and exit window area of 21.6 m^2. The detectors contain 48 mirror panels, formed from two intersecting spherical surfaces, for

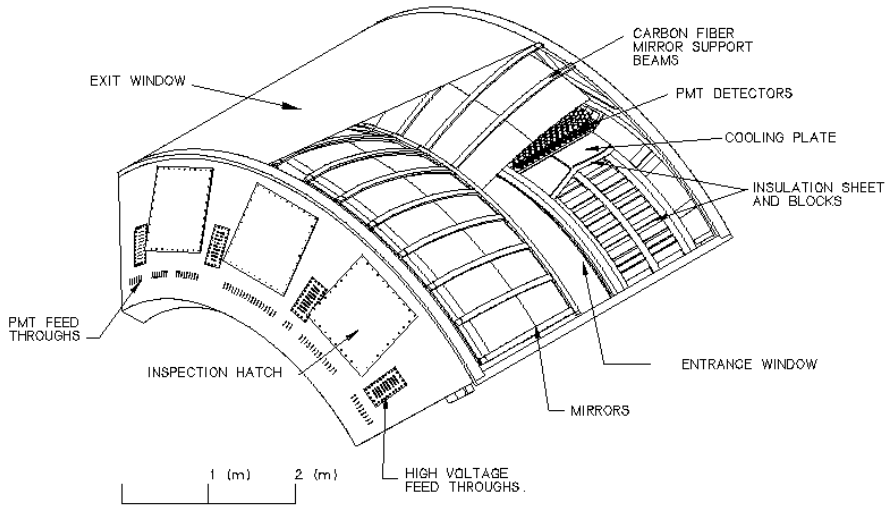

(a)

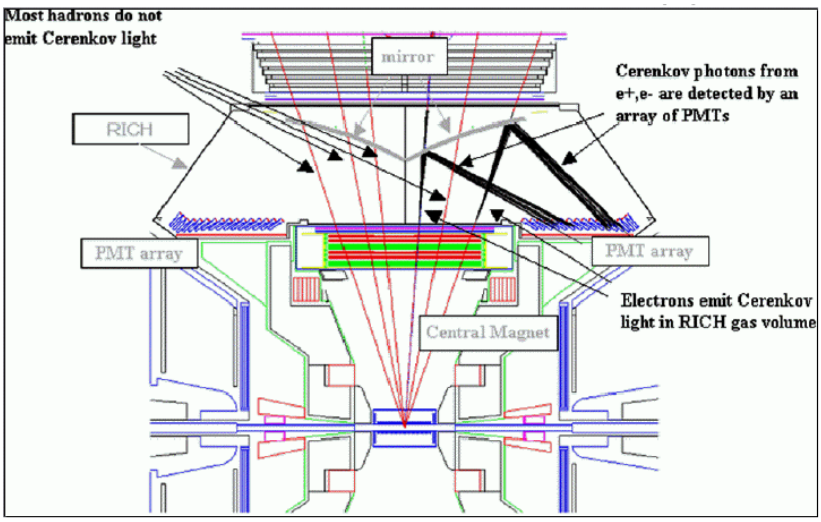

(b)

Figure 2.10: (a) Cut-away view of the RICH. (b) Schematic view of the RICH, with the beam direction corresponding to the horizontal direction in the figure.

a total reflecting area of 20 m^2. The mirrors focus Cherenkov radiation onto two arrays of photomultiplier tubes on either side of the entrance window. The phototube glass absorbs photons with wavelengths below 200 nm. The mirror reflectivity is 83% at 200 nm, and rises to 90% at 250 nm. During Run4 CO_2 was used as the radiator gas, giving a pion Cherenkov momentum threshold of 4.65 GeV/c, and an average of 12 photons per ring, with a diameter of 11.8 cm, for a completely relativistic particle.

2.3.5 Electromagnetic Calorimeters

The electromagnetic calorimeter (EMCal), spanning the full central arm acceptance (see Table 2.1), has the purpose of measuring the position and energy of electrons and photons. The EMCal consists of four sectors of Pb-scintillator sampling calorimeter in the west arm, two more Pb-scintillator calorimeters in the east arm, and two Pb-glass Cherenkov calorimeters in the east arm. The Pb-glass sectors were used previously in the WA98 experiment and were reinstalled in PHENIX. The Pb-scintillator calorimeter is a shashlik type sampling calorimeter made of alternating tiles of Pb and scintillator consisting of 15552 individual towers and covering an area of about 48 m^2. The dimensions of a single tower are $5.25 \times 5.25 \times 37.0 cm^3$. The depth of the EMC corresponds to 18 radiation lengths, chosen to optimize the electron/pion separation via the ratio of energy to momentum of a track. The energy resolution of the Pb-scintillator calorimeter is $2.1 \oplus 8.1\%/\sqrt{E}$, while the energy resolution of the Pb-glass calorimeter is $6\%/\sqrt{E}$. Figure 2.12 shows the energy separation of electrons, pions, and protons in the calorimeter.

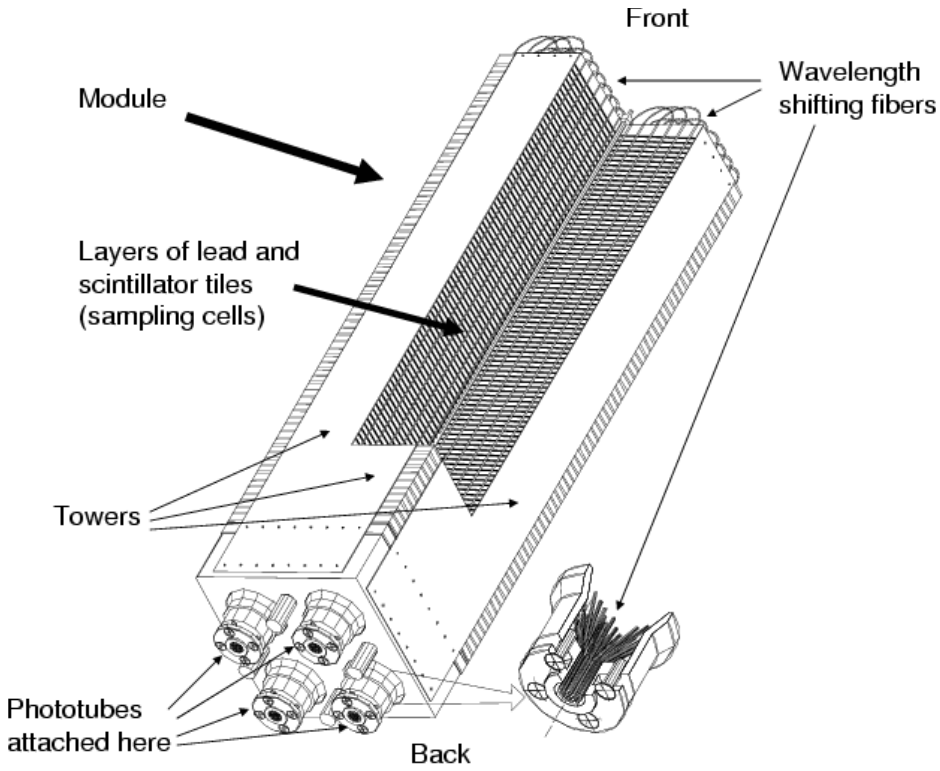

Figure 2.11: Interior view of a Pb-scintillator calorimeter module [36].

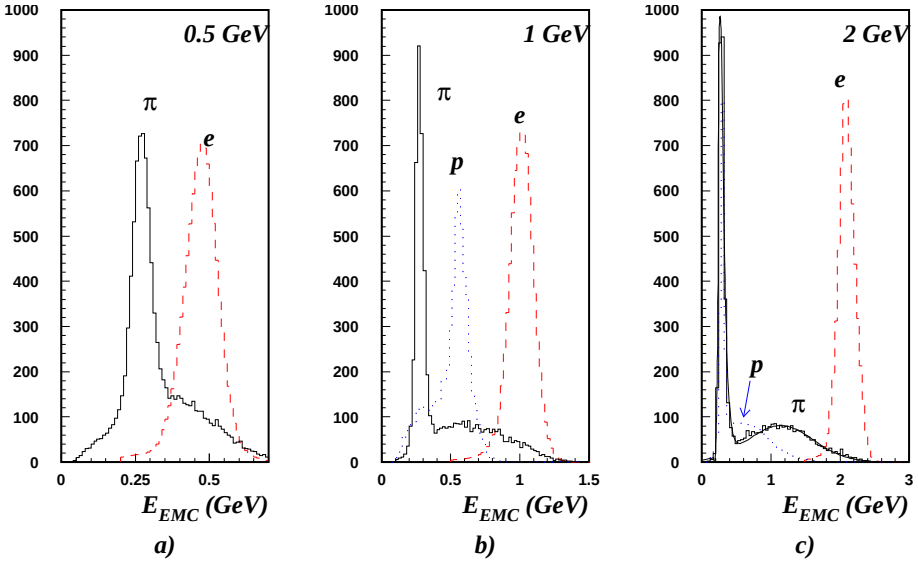

Figure 2.12: Energy spectra measured in the EMCal or electrons, protons, and pions with momentum of 0.5, 1, and 2 GeV/c. [36].

Chapter 3

Data Analysis

This chapter describes the procedure to obtain the invariant yield of electrons and positrons ($(e^+ + e^-)/2$) from Au+Au collisions.

3.1 Electron Track Candidate Selection

In order to identify electron candidates for further analysis, information from each of the detectors discussed in the previous chapter is used. First, a sample of charged tracks is selected from the drift chamber. Any track reconstructed with the Hough transform using both the X1 and X2 sections, with unique corresponding hits from the U and V wires, and also having an associated PC1 hit are used. This is given in tables below as quality of 63 or 31. Next, the projection of this track to the RICH is made. There should be PMTs fired in the RICH around this projection. We make a cut on the number of PMTs fired in a particular mask (either an annulus or a disc), the displacement from the track projection to the center of a ring fit through the PMTs fired, and the χ^2 per photoelectron of the fit. In this text, we refer to these various cuts as they are referred to in the PHENIX analysis framework: the number of RICH hits in the annulus is called n0, and in the disc called n1. The ring displacement in centimeters is called disp, and the quality of the ring fit is called chi2. The number of photoelectrons generated by the RICH in a given ring is called npe0. The final detector used is the Electromagnetic Calorimeter. A cut is made on the displacement of a shower in the EMC from the track projection to the EMC in the z and ϕ dimensions. This cut is made with respect to the average deviation of all tracks from an associated EMC hit. The number of average deviations in the z and ϕ directions is referred to as emcsdz and emcsdphi, respectively. Another cut is made on the ratio of the energy deposited in the calorimeter to the momentum of the track reconstructed from the drift

chamber hits. An electron deposits most of its energy in the EMC, and has a small mass, so the E/p for electrons will be close to 1. Hadrons don't deposit all of their energy in the EMC, and thus typically have E/p smaller than 1. The cut is made with respect to the standard deviation obtained in a gaussian fit to the E/p spectrum at a given momentum. The number of standard deviations away from the mean for a given track is called dep. Finally, a cut on the shape of the EMC shower shape is made. The shape is quantified by calculating $\chi^2 = \sum_i \frac{(E_i^{\rm pred} - E_i^{\rm meas})^2}{\sigma_i}$, where $E_i^{\rm meas}$ is the measured energy in tower i and $E_i^{\rm pred}$ is the predicted energy [38] for an electromagnetic particle of total energy $\sum_i E_i^{\rm meas}$. The value of χ^2, normalized to be between 0 and 1, is called prob.

Due to the large volume of data collected by PHENIX, efforts are made to keep the amount of data that needs to be read for a given analysis to a minimum. For analysis of electrons, tracks are reconstructed using the procedure outlined above using loose electron identification cuts, and these tracks are written to files on hard disks. This analysis of the electron candidates is much faster than having to read in, for instance, information about all charged tracks with every modification to the analysis procedure.

3.2 Run Selection

In this section, we give an overview of the selection of PHENIX runs to analyze. Events (collisions) which are taken between successive starts of the PHENIX data aquisition system (DAQ) correspond to a given PHENIX run. The electron yield per event fluctuates run-by-run due to external factors, such as extra material in the detector, detector dead areas, or unstable DAQ conditions. To simplify the analysis of the data, we try to select runs with common features, which can be represented by the electron yield per event.

Prior to this analysis, runs were divided into 12 groups which passed very loose cuts on electrons per event, difference in dead area between the east and west PHENIX arms, and had a properly functioning magnetic field within the detector. These rungroups are denoted G01-G10, and two "converter" runs C01 and C03, in which a sheet of brass was wrapped around the beam pipe (the purpose of this brass sheet will be described in a later section). Due to problems with collision centrality distribution and fluctuating detector dead areas, rungroups G01-G02 were rejected. Group C03 had a thicker brass converter than C01, and was ignored.

To further the run selection, the number of electrons $N_{\rm inc}$ divided by the number of minimum-bias (MB) events $N_{\rm evt}$ was counted for each run. Table

eID cuts
$0\% <$ Centrality $< 93\%$
$\lvert$bbcz$\rvert < 20$ cm
n0 > 2
-2.0 $<$ dep
$\sqrt{\text{emcsdphi\_e}^2 + \text{emcsdz\_e}^2} < 2.0$
disp < 5.0
chi2/npe0 < 10.0
prob > 0.01
quality $= 63$ || 31
$\lvert$zed$\rvert < 75$ cm
dcarm + emcsect > 0
(phi < 3.0 || phi > 3.1) && (phi < 3.6)
(-1.37 $<$ phi0 && phi0 < 1.0) || (2.14 $<$ phi0 && phi0 < 4.51)

Table 3.1: Electron ID cuts used in run selection

3.1 displays the cuts used to identify tracks as electrons for the purpose of this run selection. The top two cuts of the table are event selection cuts to be used throughout this analysis. The ratio $N_{\text{inc}}/N_{\text{evt}}$ was used to select good runs using the following procedure:

1. Remove obviously bad runs

Runs not passing very loose cuts on $N_{\text{inc}}/N_{\text{evt}}$ were discarded. The cuts used were

- $0.014 < N_{\text{inc}}/N_{\text{evt}} < 0.020$ for nonconverter runs with $0.4\ \text{GeV}/c < p_T < 0.8\ \text{GeV}/c$
- $0.030 < N_{\text{inc}}/N_{\text{evt}} < 0.035$ for converter runs with $0.4\ \text{GeV}/c < p_T < 0.8\ \text{GeV}/c$
- $0.0035 < N_{\text{inc}}/N_{\text{evt}} < 0.0055$ for nonconverter runs with $p_T > 0.8\ \text{GeV}/c$
- $0.0065 < N_{\text{inc}}/N_{\text{evt}} < 0.0095$ for converter runs with $p_T > 0.8\ \text{GeV}/c$

2. Calculate the average of $N_{\text{inc}}/N_{\text{evt}}$ for each rungroup G

$$\langle N_{\text{inc}}/N_{\text{evt}} \rangle_G = \frac{\sum_{\text{run}\in G} N_{\text{inc}}(\text{run})}{\sum_{\text{run}\in G} N_{\text{evt}}(\text{run})} \tag{3.1}$$

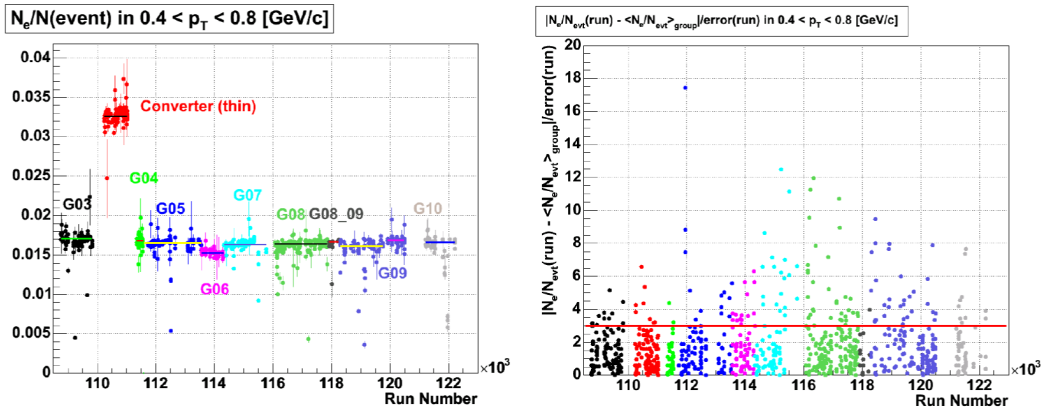

Figure 3.1: Left: Ratio of $N_{\rm inc}/N_{\rm evt}$ for each run in 0.4 GeV/c $< p_T <$ 0.8 GeV/c. Right: Deviation of $N_{\rm inc}/N_{\rm evt}$ from $\langle N_{\rm inc}/N_{\rm evt}\rangle_G$ in units of $\sigma(\mathsf{run})$ for each run. The red line corresponds to a σ of 3.0.

3. Calculate the RMS distance of $N_{\rm inc}/N_{\rm evt}$ from the average $\sigma(\mathsf{run})$ for each run

4. Remove runs with

$$\frac{|N_{\rm inc}(\mathsf{run})/N_{\rm evt}(\mathsf{run}) - \langle N_{\rm inc}/N_{\rm evt}\rangle_G(\mathsf{run})|}{\sigma(\mathsf{run})} > 3.0 \qquad (3.2)$$

5. Iterate steps 2-4 until no runs are removed

The above method is applied separately for tracks with 0.4 GeV/$c < p_T <$ 0.8 GeV/c and $p_T >$ 0.8 GeV/c. Figures 3.1 and 3.2 show $N_{\rm inc}/N_{\rm evt}$ for each run, in the two p_T ranges mentioned above. Iteration of the above algorithm only had to be applied twice before no runs were removed, indicating that removed runs really were outliers. Note that the G08 group was split into two groups called G08 and G08_09 due to a slight change in detector dead area.

3.3 Event Selection

In the analysis, we applied the following event selection cuts.

- MB $\equiv$ BBCLL1 $\geq$ 2 && ZDCNS.
- $|\mathsf{bbcz}| < 20$ [cm].

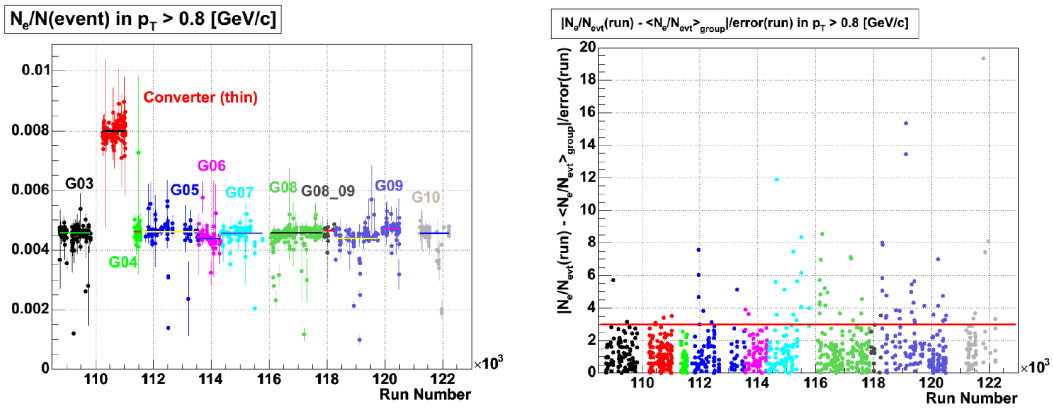

Figure 3.2: Left: Ratio of $N_{\rm inc}/N_{\rm evt}$ for each run in $p_T > 0.8$ GeV/c. Right: Deviation of $N_{\rm inc}/N_{\rm evt}$ from $\langle N_{\rm inc}/N_{\rm evt}\rangle_G$ in units of σ(run) for each run. The red line corresponds to a σ of 3.0.

In this analysis, the events were selected which passed the standard PHENIX minimum-bias trigger using a coincidence between hits in the BBC and ZDC. Events were also required to have a collision vertex within 20 cm of the center of the PHENIX detector. Table 3.2 summarizes the number of MB events for each run group. Collision centrality is obtained by the "clock" method described in the previous chapter. Minimum-bias events are divided into five centrality classes of 0-10%, 10-20%, 20-40%, 40-60% and 60-93%. The number of events used in this analysis is about 30 times greater than that used for the Run 2 analysis [7, 29].

3.4 Track Selection

Two criteria are used when selecting electrons tracks. The first criteria is that the track passes parameter cuts which imply with high probability that the track is an electron. The second criterion is that the track pass fiducial cuts, which ensures that the track is in a region of the detector that is well-understood, that is, behaves similarly in reality and simulation.

3.4.1 Electron Identification Cuts

For tracks with p_T below 4.8 GeV/c, the RICH is only fired by electrons. The RICH is the primary means of electron detection in this p_T region. As

Group name	MB events	0-10 %	10-20 %
G03	4.78688e+07	5.16072e+06	5.18822e+06
G04	1.13048e+07	1.22132e+06	1.21786e+06
G05	9.50698e+07	1.02695e+07	1.02229e+07
G06	5.04338e+07	5.33612e+06	5.38849e+06
G07	8.90391e+07	9.53750e+06	9.56670e+06
G08	2.14707e+08	2.32448e+07	2.32002e+07
G08_09	1.17750e+07	1.27365e+06	1.27422e+06
G09_01	9.71969e+07	1.04973e+07	1.05112e+07
G09_02	8.33905e+07	9.00950e+06	9.03118e+06
G10	4.73697e+07	5.09655e+06	5.12646e+06
Total	7.48156e+08	8.06470e+07	8.07275e+07
C01	5.78950e+07	6.30718e+06	6.29365e+06
Group name	20-40 %	40-60 %	60-93 %
G03	1.03388e+07	1.03648e+07	1.68163e+07
G04	2.42846e+06	2.42847e+06	4.00870e+06
G05	2.04106e+07	2.03664e+07	3.38004e+07
G06	1.08135e+07	1.08421e+07	1.80536e+07
G07	1.91165e+07	1.90910e+07	3.17274e+07
G08	4.61435e+07	4.60030e+07	7.61155e+07
G08_09	2.53406e+06	2.52202e+06	4.17104e+06
G09_01	2.09449e+07	2.08849e+07	3.43587e+07
G09_02	1.79909e+07	1.79190e+07	2.94399e+07
G10	1.02133e+07	1.02314e+07	1.67020e+07
Total	1.60934e+08	1.60653e+08	2.65194e+08
C01	1.24610e+07	1.24254e+07	2.04077e+07

Table 3.2: Number of events for each run group.

described in the previous chapter, two variables are stored in data files which correspond to the number of fired RICH PMTs associated with a given track: n0 and n1. Recall that n0 is the number of PMTs fired in an annulus about the track projection to the RICH, and n1 is the same, except for a disc instead of the annulus. Typically (and in past electron measurements), only n0 was used to identify electrons since Cherenkov radiation has a minimum opening angle. However, during data production a mistake was found in which the track reconstruction software assumed incorrectly the alignment of the RICH mirrors with the rest of the PHENIX detector. The error in misalignment differs as a function of the position of the track in the detector. Due to the misalignment, the PMTs associated with a track are searched for in a disc instead of an annulus. Recall also that the disc used for n1 has a larger outer radius than the annulus used for n0. In most of the detector the alignment problem is small, and the use of n1 instead of n0 eliminates the loss of electron identification efficiency with only a small loss of purity which can be corrected for. But, as will be discussed more later in this chapter, the alignment problem in the east-south region of the detector was severe enough that simply using n1 instead of n0 was not sufficient to correct for the alignment bug, and special care was taken with the section of the detector.

In the data files used for this analysis, all tracks had an implicit cut of n0 ≥ 2. Thus, we cannot simply use a cut on n1 as described above. However, this implicit cut on n0 is loose enough to warrant only a small increase in systematic error. All cuts on the number of PMTs fired involve a cut on n1, in addition to this loose cut on n0. For $p_T < 5$ GeV/c, the same eID cuts are used as in table 3.1, except that the n0 cut was reduced to n0 ≥ 2, and a cut n1 ≥ 3 was added. For $p_T \geq 5$ GeV/c, charged hadrons emit Cherenkov light. In order to cut out most of this hadronic background, addional cuts of n1 ≥ 5 and prob > 0.2 were added.

3.4.2 Fiducial Cuts

The fiducial cuts used in this analysis can be divided into two main classes: cuts that are independent of the rungroup and cuts that depend on the rungroup. Table 3.3 displays the fiducial cuts which are independent of the rungroup. These cuts can be explained as follows:

- |zed| < 75
  The cut is applied to remove inefficient acceptance region in DC.

- $-1.37 <$ phi0 < 1.0 || $2.14 <$ phi0 < 4.51
  The cut is applied to remove electron pairs converted from MVD support pipes.

Basic Fiducial Cuts
$\lvert\mathsf{zed}\rvert < 75$ [cm]
$(\mathsf{phi} < 3.0 \;\|\|\; 3.1 < \mathsf{phi})$ && $(\mathsf{phi} < 3.6)$ [rad]
$(-1.37 < \mathsf{phi0}$ && $\mathsf{phi0} < 1.0) \;\|\|\; (2.14 < \mathsf{phi0}$ && $\mathsf{phi0} < 4.51)$ [rad]

Table 3.3: Basic fiducial cuts.

- $\mathsf{phi} < 3.0 \;\|\|\; 3.1 < \mathsf{phi} < 3.6$
  The cut is applied to remove the inconsistent region of phi between non-converter and converter data.

The acceptance (live area) of the detector was more stable in the G9_02 rungroup than it was in other groups. Because of this, rungroup-dependent fiducial cuts were made on the rest of the data such that the remaining acceptance of all rungroups was similar to that of G9_02. Details on these cuts can be found in the Appendix. For the converter runs, which were used to measure electron background at low p_T, the east-south region of the detector was cut out entirely due to the alignment problem in the RICH described above, and because statistical precision at low p_T is not an issue. Figure 3.3 shows the phi distribution of tracks in the DC from data and Monte-Carlo (MC) simulation. There is a clear discrepancy between data and MC in the east-south region of the detector. In this figure the distribution from simulation is normalized to have the same total number of electron tracks in the west arm.

3.4.3 Hadron Background Subtraction and the E/p Distribution

After applying the electron identification cuts, there still remains background to subtract. To understand what background remains, we can look at the shape of the E/p distribution. For electrons which originate from the vertex, the E/p distribution should be a Gaussian centered at 0.98, as the EMCal is calibrated for measuring energy from photons.

Figures 3.4 and 3.5 show the E/p distribution for various ranges in p_T These plots were generated using the eID cuts of detailed above, separately for p_T below 5 GeV/c and for p_T above 5 GeV/c, with the exception that the dep cut was not applied (because that is essentially the E/p we are looking at). The red points are the estimated distributions of hadron tracks which are randomly associated with a ring in the RICH. This estimation is performed by swapping the north and south sides of the RICH in software, and reconstructing the

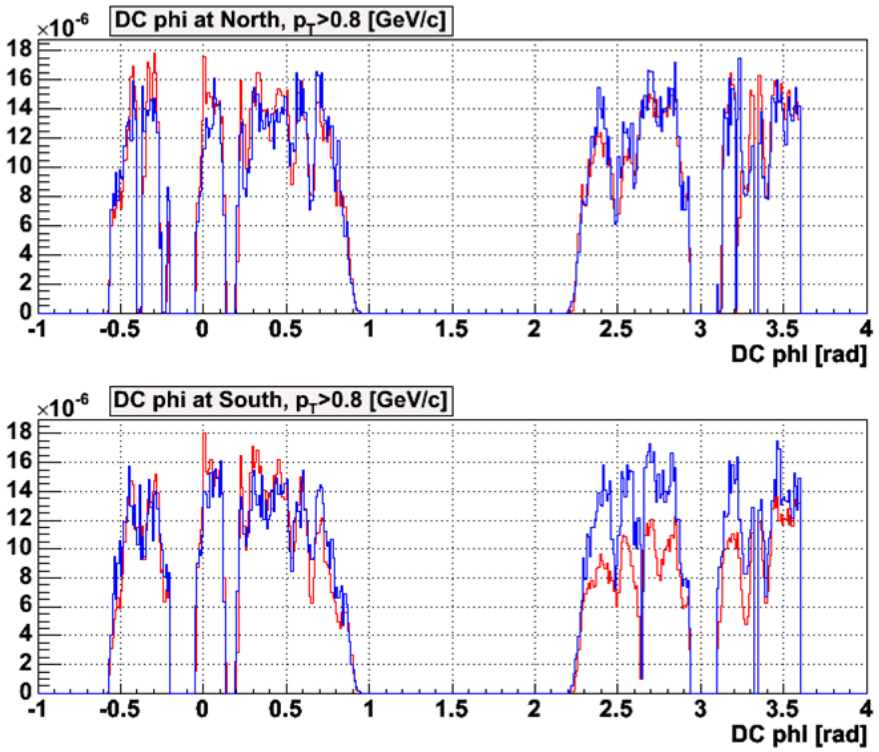

Figure 3.3: DC phi distribution (Red: Data, Blue: Simulation).

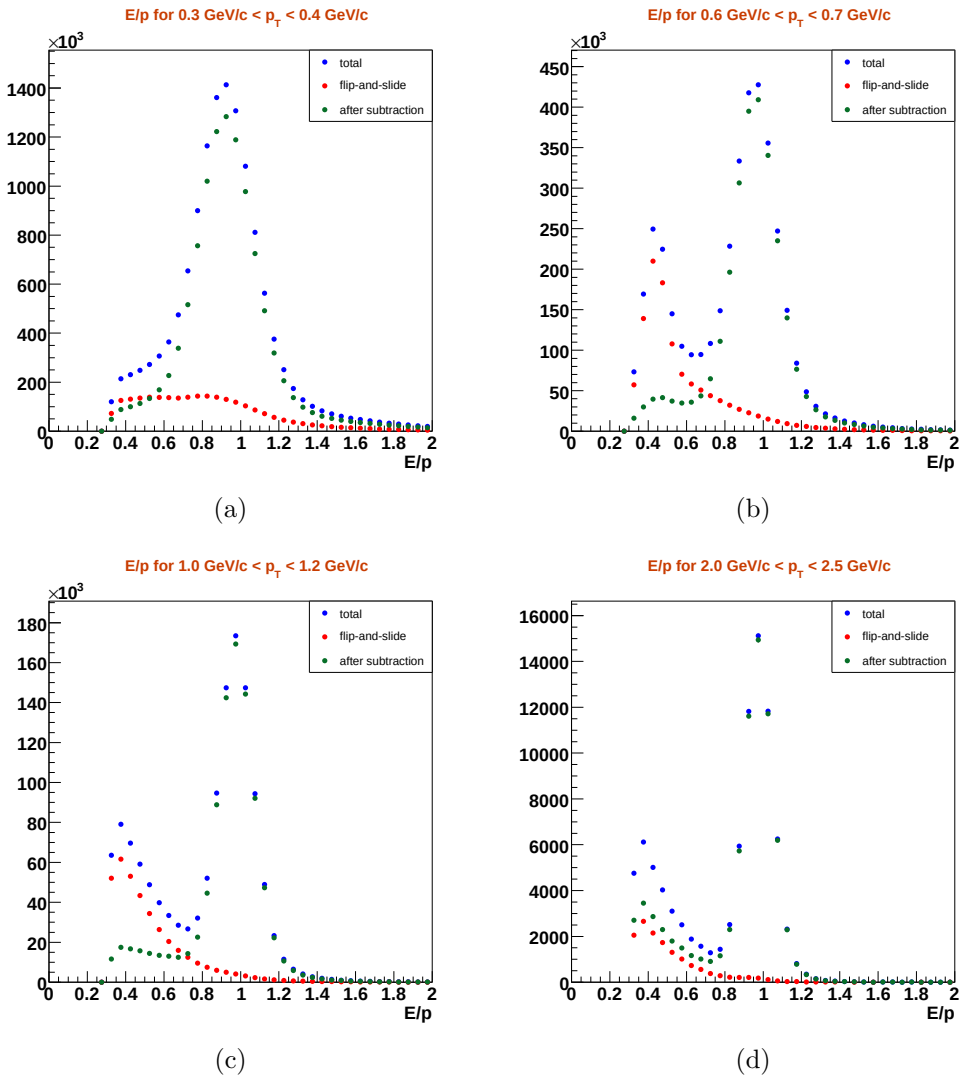

Figure 3.4: E/p distributions for various p_T ranges

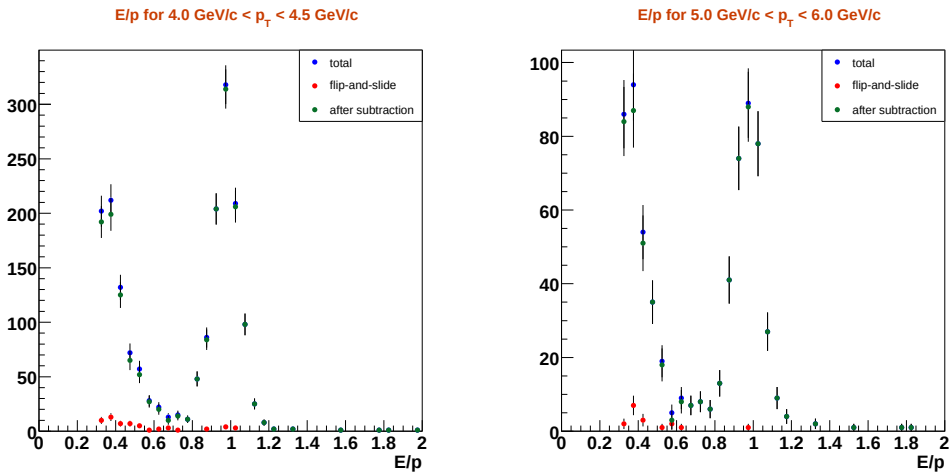

(a)

(b)

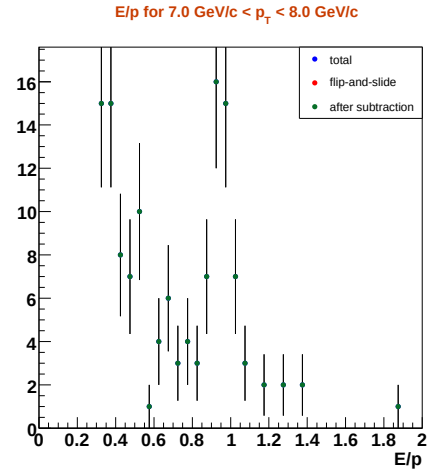

(c)

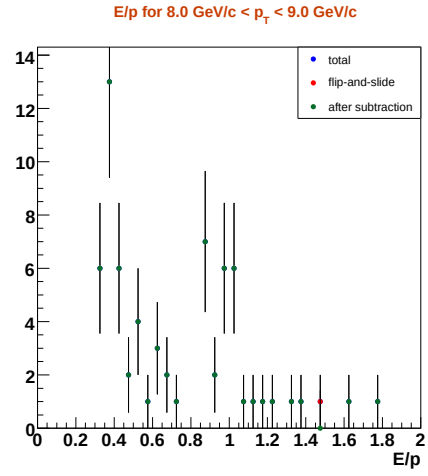

(d)

Figure 3.5: E/p distributions for various p_T ranges

track matching to RICH once again. That is, DC tracks from the south are matched with RICH hits in the north, and vice versa. Hadrons with p_T below 4.8 GeV/c with an associated RICH hit must have been moving parallel to an electron. For a given hadron, there should be little correlation with tracks moving parallel with it on one side of the detector, to such tracks on the other side. To the extent that the active area of the RICH on the two sides of the detector are identical, this method gives a proper statistical estimate of the random hadron associations in the electron sample.

After subtraction of the random hadron associations, an additional low E/p tail remains in the distribution. This tail can be accounted for by electrons from Kaons which decay far from the collision vertex through the K_{e3} channel. The electrons are reconstructed with a momentum higher than the actual momentum of the electrons, and as such have a low E/p. A full GEANT simulation is performed to determine the background from K_{e3}. See the section on the cocktail calculation for more information.

For p_T above 4.8 GeV/c, charged pions begin to radiate Cherenkov light in the RICH. Though the tight RICH cuts and the cut on the shower shape, or prob variable, can do much to eliminate the background from charged pions, some background can still remain. To estimate this background, we rely on the fact that the distribution of the prob variable and E/p distribution is roughly independent of p_T for hadrons at high p_T, and that a cut on prob$<$0.01 eliminates the vast majority of electrons. First, we obtain a sample of hadrons from data files in the p_T range of 1-4 GeV/c by imposing a veto on the RICH. The hadron sample is then divided into two samples, one with prob$>$0.01 and the other with prob$<$0.01. The ratio of these two hadron samples (with the different prob cuts) is taken. Figure 3.6 shows the two hadron samples and their ratio. The E/p distributions for p_T above 5 GeV/c are then prepared from the data with cuts identical to those described above, except with the prob cut reversed to prob$<$0.01. These E/p distributions are then divided by the ratio shown in Figure 3.6(b) to obtain an estimate of the E/p distributions of hadrons passing the prob$>$0.01 cut. Figure 3.7 shows the estimation for the hadronic background along with the total E/p distribution. The estimation is actually an overestimation, as some electrons do pass the prob$<$0.01 cut. This can be seen in 3.7(a) as a peak in the hadronic estimation. From these plots, we determine that any hadronic background below 8 GeV/c is negligible. Between 8-9 GeV/c in p_T, we estimate a background of 20%, with an uncertainty of 10%.

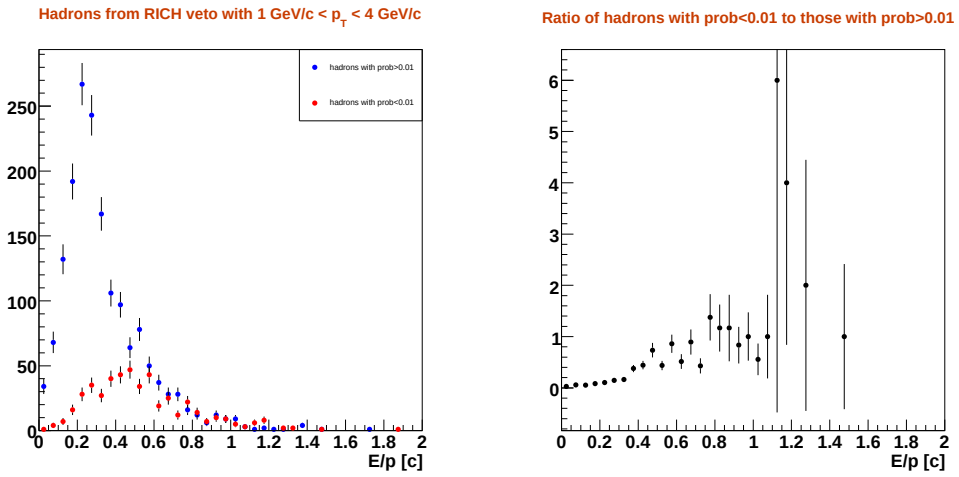

(a) (b)

Figure 3.6: E/p distribution of hadron samples used in contamination study.

3.5 Corrections to the Data

3.5.1 Single Track Acceptance × Efficiency

We are trying to measure the invariant yield of $e^{\pm}$ from Au+Au collisions,

$$E\frac{d^3N}{d^3\boldsymbol{p}} = \frac{c}{2\pi p_T}\frac{d^2N}{dp_T dy} \tag{3.3}$$

where the equality uses the fact that there is no azimuthal dependence on the particle yield. However, there certainly is an azimuthal dependence on the particle yield as seen by the PHENIX central arms, since the arms themselves only cover half of the azimuth (a quarter each). In addition to this factor of 2 discrepancy between the measured PHENIX yield and the actual yield, parts of the detector area are not functioning in a given run. On top of that, the eID and fiducial cuts cut out some electrons as well as cutting out background. In order to correct for these acceptance and efficiency effects, single electrons and positrons were simulated randomly in azimuthal angle, pseudorapidity $|\eta| < 0.5$, and 0 GeV/c $< p_T <$ 15 GeV/c. The $|\eta|$ coverage of the PHENIX central arms is about 0.35. The simulated η range needed to be greater than this range, but not too much greater. The particle yields in Au+Au collisions at RHIC are quite flat for $|\eta| < 0.5$ as seen by the BRAHMS experiment [30], so the simulated range of $|\eta| < 0.5$ seems reasonable. These simulated electrons and positrons are run through a full GEANT based de-

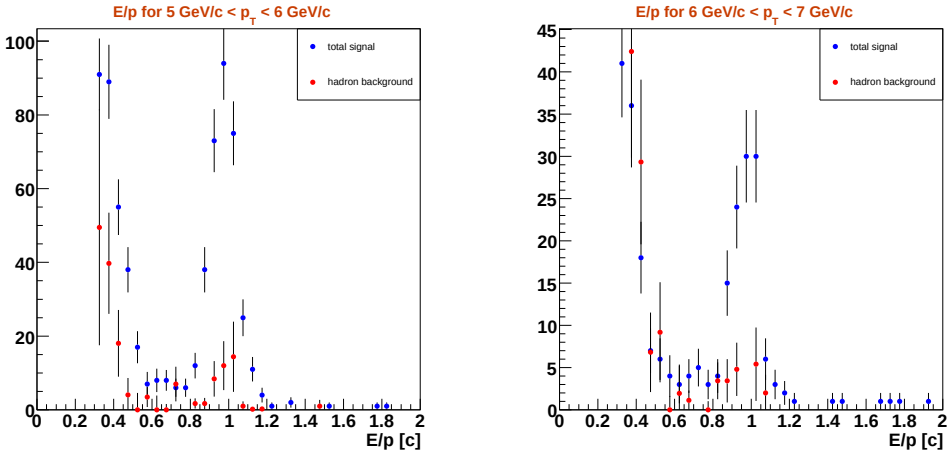

(a)

(b)

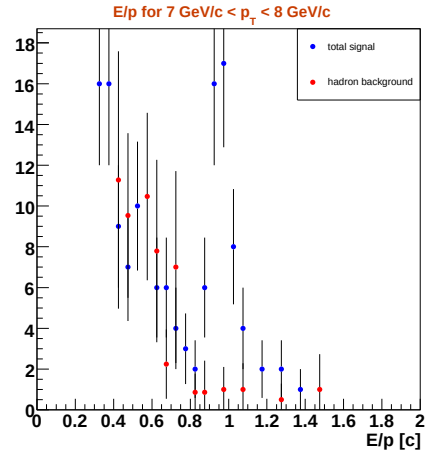

(c)

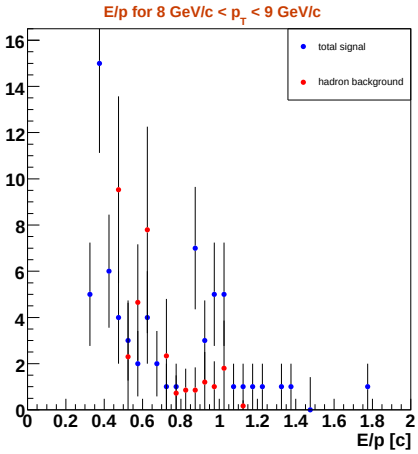

(d)

Figure 3.7: Total E/p distributions compared with estimate of hadronic background, for various p_T ranges

tector simulation, and tracks are reconstructed just as in data. The simulated particles are weighted with a realistic p_T distribution to accurately emulate momentum smearing effects from the finite momentum resolution of the drift chamber. The reconstructed tracks are then compared to the simulated tracks as a function of the *reconstructed* momentum, to give the acceptance $\times$ efficiency of our reconstructed electron sample. Figure 3.8 shows the acceptance

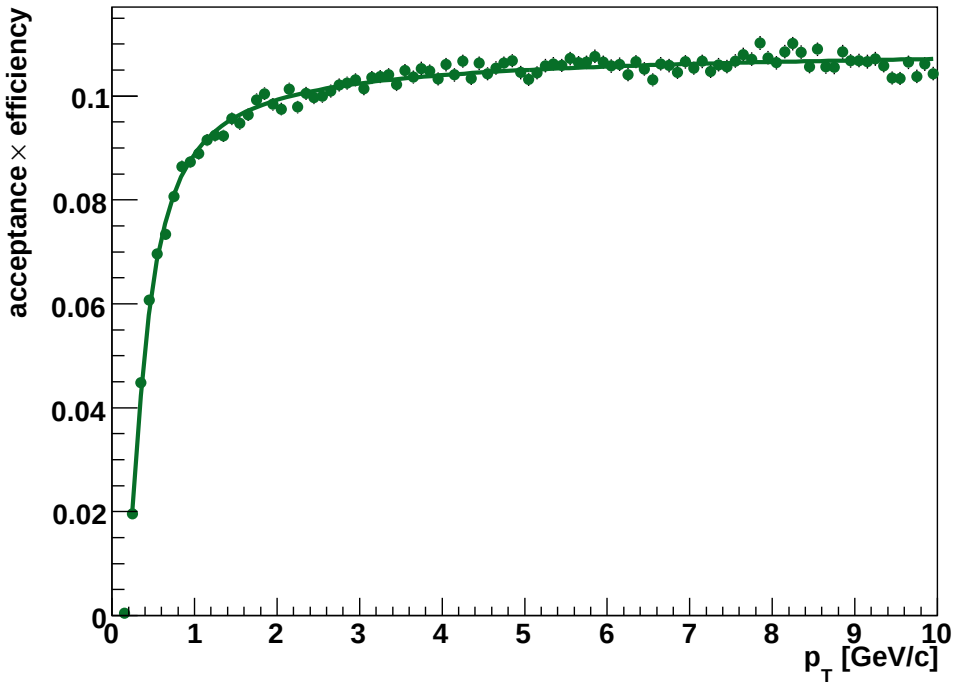

Figure 3.8: acceptance $\times$ efficiency for the eID cuts used for $p_T < 5$ GeV/c, as a function of reconstructed p_T

$\times$ efficiency for the cuts that we use below 5 GeV/c in p_T. The simulation only gives the correct efficiency for tracks which originate close to the collision vertex, so that the reconstructed momentum of the track is close to the actual momentum. Most electrons are expected to originate adequately close to the vertex. The main exception to this rule is the electrons from 3-body decays of Kaons, the so-called K_{e3} decay. The contribution of these electrons to the measured spectrum must be taken into account by a simulation which includes the electron identification cuts and the decay length of the K_{e3} decay, as described in Chapter 4.

Corrections to the Correction

Of course, simulation cannot perfectly describe the response of the detector to an incoming electron. The tighter the cuts that we make on the reconstructed variables, the more error we introduce into the efficiency correction. For $p_T > 5$ GeV/c, the eID cuts used are tight indeed, so if we were to use the efficiency correction from the MC simulation, we would be forced to include a large systematic error. But we suspect, and indeed can see from Figure 3.8, that for $p_T > 2$ GeV/c the efficiency is not strongly dependent on p_T. Furthermore, the slight dependence there is on p_T will mostly be the same whether the loose or tight cuts are used. We can deduce the efficiency for the tight cuts at high p_T empirically assuming that after proper correction the inclusive electron yield is independent of the cuts used, to the extent that the electron sample is pure. This last statement can be written as

$$\frac{1}{2\pi p_T}\frac{d^2N_{\text{loose}}}{dp_T dy}\frac{1}{\epsilon_{\text{loose}}} = \frac{1}{2\pi p_T}\frac{d^2N_{\text{tight}}}{dp_T dy}\frac{1}{\epsilon_{\text{tight}}} \tag{3.4}$$

where $N_{\text{loose(tight)}}$ is the number of $e^{\pm}$ tracks per event passing the loose(tight) cuts, and $\epsilon_{\text{loose(tight)}}$ is the acceptance $\times$ efficiency for the loose(tight) cuts. Equation 3.4 can be rearranged as

$$\epsilon_{\text{tight}} = \frac{N_{\text{tight}}}{N_{\text{loose}}}\epsilon_{\text{loose}}. \tag{3.5}$$

Equation 3.5 is true up to the statistical accuracy of N_{loose} and N_{tight}. If the error from the statistical accuracy in the number of tracks is smaller than the difference in error from the lack of understanding of the detector response to an electron corresponding to the loose and the tight cuts, then it is better to use Equation 3.5 to determine ϵ_{tight} than it is to calculate ϵ_{tight} directly from the MC simulation.

The same argument above for relating the efficiency for different cuts can also be used for relating the efficiency in different azimuthal sections of the detector. Indeed, if we could run the experiment for an arbitrarily long time, then from the point of view of a single particle measurement, such as the measurement which is the topic of this thesis, it would be best to build a very small detector which we understand very well. Well, small in terms of the azimuthal coverage anyway, because the experimental setup (the collider) is azimuthally symmetric. More η coverage gives more information (but costs more time and money). The argument also applies for the efficiency across different data-taking runs. Recall that the number of electron candidates measured per event varies with rungroup. To lessen this variation, fiducial

cuts were applied to make all runs have similar efficiency to those in rungroup G9_02. But fiducial cuts can only do so much. In the case where a part of the detector is dead in rungroup G9_02, but alive in other parts, fiducial cuts do not help at all. Recall also the RICH misalignment bug in the reconstruction software which limits our understanding of the eID efficiency in the east south region of the detector (and has a small effect in the other regions).

In light of the above problems, we decide to restrict the MC efficiency calculation to the G9_02 rungroup with the east south region removed. This method trades the errors associated with the temporal and spatial variations of the detector with statistical error associated with the number of electron candidates measured. At high p_T the statistical error is very large, however the p_T dependence of the difference in efficiency between loose/tight cuts, different rungroups and different detector regions is negligible at high p_T. Figure 3.9 shows the ratio of $e^{\pm}$ per event taking all of these differences into acount. As can be seen from the figure, the p_T dependence of this ratio is small. Also, the statistical errors associated with the entire p_T range are also quite small, which implies that this method is more reliable than trying to understand the different efficiencies separately.

3.5.2 Multiplicity-Dependent Efficiency Correction

In addition to the efficiency for a single electron passing through the detector to pass the fiducial and eID cuts due to detector dead area and the efficiency of the cuts themselves, there is also a finite efficiency loss for particle detection due to the presence of other particles nearby. The fact that this effect is not zero can easily be seen by imagining the limit of infinite multiplicity, in which every channel of the detector fires. Obviously, in this case no particle can be distinguished. To get a quantitative understanding of the multiplicity-dependent efficiency loss, we embed simulated single electrons and positrons into data files containing detector hits from real collisions. The same simulated particles are used in this method as those used to estimate the single particle efficiency loss. The simulated $e^{\pm}$ are run through a GEANT simulation of the central arms, and the hits are added to the data files containing hits from a real Au+Au event. Next, these new files containing the embedded $e^{\pm}$ are run through the entire reconstruction software to produce track candidates containing the variables upon which we make identification cuts. These track variables are then run through a recalibration procedure to produce the variables which are comparable in simulation and data. We then define the

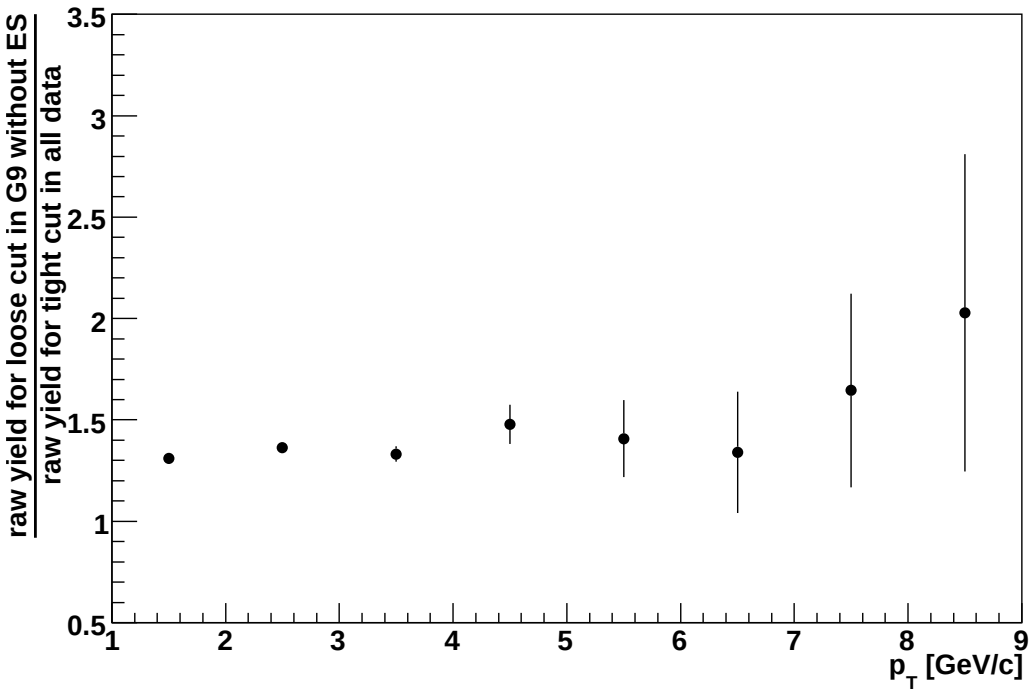

Figure 3.9: Ratio of electrons and positrons per event for the loose cuts (cuts used for $p_T < 5$ GeV/c) in rungroup G9_02 excluding the east south region, to the electrons and positrons per event for the tight cuts in all rungroups with the east south included. Note that a ratio of about 0.75 would imply no difference in the cut efficiency since the east south is about a quarter of the detector live area.

embedding efficiency as

$$\epsilon_{\text{embed}} = \frac{\#\text{ reconstructed } e^{\pm} \text{ from embedded data}}{\#\text{ reconstructed } e^{\pm} \text{ from single track data}} \tag{3.6}$$

where a reconstructed particle from embedded data has most of its DC hits associated with hits from the simulated particle.

As a systematic cross-check on this method for determining the multiplicity-dependent energy loss, a data-driven method was employed. The general strategy of this data-driven method is to select a very pure sample of electrons from the data, applying loose cuts to the electrons. Then, we measure the efficiency loss as a function of collision centrality of tighter cuts (cuts actually used in

the analysis) relative to that of the loose cuts. We then still need simulation to determine the multiplicity-dependent loss due to the loose eID cuts, but simulation is more reliable when we use loose cuts. In order to get a pure sample of electrons, we isolate $e^{\pm}$ pairs from photon-conversions in the beampipe and from π^0 Dalitz decays. We assume, reasonably, that the multiplicity-dependent efficiency loss for these electrons is the same as for all electrons. Figure 3.10

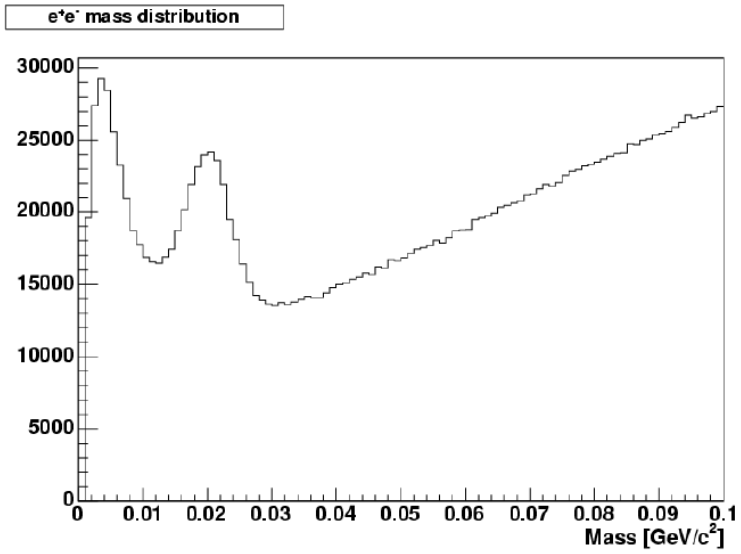

Figure 3.10: Invariant mass distribution of $e^{\pm}$ pairs from data sample used for the multiplicity-dependent efficiency loss estimate.

shows the invariant mass distribution of $e^{\pm}$ pairs from the data. The peak at $\sim$ 20 MeV/c^2 corresponds to the apparent mass of electrons from photon conversions in the beampipe. The peak at $\sim$ 5 MeV/c^2 corresponds to $e^{\pm}$ from π^0 Dalitz decays. As mentioned above, we would like to have electrons identified by using both loose cuts and tight cuts. However, if loose cuts are applied to both the electron and the position in the pair, then the sample will contain contamination from hadrons. In order to make sure that the pair is really an $e^{\pm}$ pair, we apply tight eID cuts to one of the particles in the pair. We restrict ourselves to pairs with one of the particles in the acceptance of the Time of Flight detector so that we can use the TOF for electron identification. This limits the statistics of this analysis, but after all this method is only used as a systematic cross-check.

Tables 3.4 and 3.5 display the loose cuts used for the pair (the cuts which are implicit in the data files, actually), and the cuts used on one of the particles

eID cuts for both tracks of a pair
$\|\mathsf{bbcz}\| \leq 20$ cm (≤ 30cm in cEWG)
$0.15 < p_{\mathrm{T}} < 25$ (in cEWG)
$\mathsf{n0} > 1.0$ ($\mathsf{n0} > 1$ || $\mathsf{sn0} > 1$ in cEWG)
$\mathsf{ecore/mom} > 0.4$ ($0.3 < \mathsf{ecore/mom} < 2.0$ in cEWG)
$\|\mathsf{emcsdphi\_e}\| < 4.0$ in cEWG
$\|\mathsf{emcsdz\_e}\| < 4.0$ in cEWG
$\mathsf{quality} == 63$ || $\mathsf{quality} == 31$

Table 3.4: Minimum cuts.

eID cuts for one track of a pair
$\mathsf{n0} > 3.0$
$\mathsf{disp} < 5.0$
$\mathsf{chi2/npe0} < 10$
$-2.0 < \mathsf{dep} < 3.0$
$\sqrt{\mathsf{emcsdphi\_e}^2 + \mathsf{emcsdz\_e}^2} < 2.0$
$\mathsf{prob} > 0.1$
$\|\mathsf{m2tof}/(\mathsf{mom}^2)\| < 0.3$ || $\|\mathsf{m2emc}/(\mathsf{mom}^2)\| < 0.3$

Table 3.5: eID cuts for one track of a e^-e^+ pair.

in the pair to make sure that the pair is indeed an $e^{\pm}$ pair. The cuts used for the analysis for $p_T < 5$ GeV/c are then applied to the other particle in the pair, and the relative efficiency loss is calculated. As described in the previous section, for $p_T > 5$ GeV/c we obtain the efficiency by the relative electron yield between the samples with the cuts used for the two p_T ranges. This relative yield includes multiplicity-dependent effects, so we only explicitly calculate the multiplicity-dependent efficiency loss for the cuts used for $p_T < 5$ GeV/c. Now, some of the relative efficiency loss using the method just described is due to the single particle efficiency. To obtain an estimate of the multiplicity-dependent component of this relative loss, we divide the relative loss by the loss for peripheral collisions (60%-93% centrality), since the multiplicity-dependent loss in peripheral collisions is very low. So we have defined the multiplicity-dependent efficiency loss from the data-driven method for centrality C as

$$\epsilon_{\text{mult}}^{\text{data},C} = \frac{\epsilon_{\text{eID}}^{\text{data},C}}{\epsilon_{\text{eID}}^{\text{data},60-93\%}} \tag{3.7}$$

with

$$\epsilon_{\text{eID}}^{\text{data},C} = \frac{\epsilon_{\text{tight cuts}}^{C}}{\epsilon_{\text{loose cuts}}^{C}}. \tag{3.8}$$

What we really want to measure is the above efficiency with the loose eID cuts set to no cuts at all. We simply correct the multiplicity-dependent efficiency loss by using the simulation embedding procedure for the loose cuts, $\epsilon_{\text{loose}}^{\text{embed},C}$ to obtain the more accurate estimate of the multiplicity-dependent loss from the otherwise data-driven method. Table 3.6 displays the various embedding

Centrality	$\epsilon^{\text{embed},C}$	$\epsilon_{\text{mult}}^{\text{data},C}$	$\epsilon_{\text{mult}}^{\text{data},C}\,\epsilon_{\text{loose}}^{\text{embed},C}$
0-10%	0.771248	0.81750	0.769380
10-20%	0.835172	0.89725	0.855898
20-40%	0.900285	0.94769	0.924201
40-60%	0.952219	0.98966	0.977470
60-93%	0.982370	1	0.996741
00-93%	0.851747	0.92269	0.887703

Table 3.6: Embedding efficiency.

efficiencies described above. The difference between the left and right columns gives an idea of the systematic error involved in this estimation. The use of the sample of conversion and Dalitz $e^{\pm}$ pairs will be discussed further in the section pertaining to systematic error analysis.

3.5.3 Bin Width Correction

As mentioned before, we are trying to measure

$$\frac{1}{2\pi p_T}\frac{d^2N}{dp_T dy} \times \text{corrections} = \frac{1}{2\pi p_T}\frac{dN}{dp_T}\frac{1}{\Delta y} \times \text{corrections} \tag{3.9}$$

where we have factored out the rapidity dependence since the dependence is flat. By convention, N represents the number of electrons per event plus the number of positrons per event measured, divided by 2. We do not have the (infinite) statistics required to measure dN/dp_T. Instead, we measure, within multiple bins (p_T ranges) with $p_T^{\text{bin}} \in [a^{\text{bin}}, b^{\text{bin}}]$,

$$\begin{aligned}
&\frac{1}{b^{\text{bin}} - a^{\text{bin}}} \sum_{\text{tracks with } p_T \in [a^{\text{bin}}, b^{\text{bin}}]} \frac{1}{p_T} \\
&\overset{\text{within statistics}}{=} \frac{1}{b^{\text{bin}} - a^{\text{bin}}} \int_{N(a^{\text{bin}})}^{N(b^{\text{bin}})} \frac{1}{p_T} dN = \frac{1}{b^{\text{bin}} - a^{\text{bin}}} \int_{a^{\text{bin}}}^{b^{\text{bin}}} \frac{1}{p_T}\frac{dN}{dp_T} dp_T \\
&= \left\langle \frac{1}{p_T}\frac{dN}{dp_T} \right\rangle^{\text{bin}}.
\end{aligned} \tag{3.10}$$

So we end up measuring the average value of the invariant yield within a given p_T bin. But we want to be able to easily compare our measurement to model predictions, and to other measurements which might not use the same binning, so what we really want is to measure the invariant yield at a given value of p_T, say, at the center of the bin. The following procedure is used to convert the average value of the yield into the yield at the center of the bin:

- First, we empirically fit the yield (separately for each centrality) to a function which fits the data. The inclusive yield turns out to obey well a modified power law function of the form

  $$f(p_T) = \frac{A}{(p_0 + p_T)^n} \tag{3.11}$$

  where A, p_0, and n are fitting parameters. The values of these parameters are determined from fitting at each iteration.

- Find the values of p_T at which the above function takes on its average value in each bin $[a, b]$ by solving for p_T in the equation

  $$\langle f \rangle_{[a,b]} \equiv \frac{1}{b-a}\int_a^b f(x)dx = f(p_T^{\text{mean}}). \tag{3.12}$$

Acually, with the particular form of the function f we are using, it is easy to invert the above equation analytically as

$$p_T^{\text{mean}} = \left(\frac{A}{\langle f \rangle} \right)^{1/n} - p_0. \tag{3.13}$$

- Next, move the data point from the center of the bin to p_T^{mean}.

- Iterate the above steps until the parameters of f converge.

The above procedure gives us p_T^{mean} for each bin, and a function which passes through the data points. The final step, is to move the data points from p_T^{mean} for the given bin to $p_T = (b-a)/2$, and scale the yield y and the error on the yield δy by

$$y' = y \times \frac{f(\frac{b-a}{2})}{f(p_T^{\text{mean}})}, \ \delta y' = \delta y \times \frac{f(\frac{b-a}{2})}{f(p_T^{\text{mean}})}. \tag{3.14}$$

This gives us the approximate value of the invariant yield at the value of p_T at which the data point rests, so we can compare to other data and theories in a way which is independent of any particular momentum binning. The assumption which this procedure relies on is that the invariant differential yield as a function of p_T does not wildly oscillate, which is quite reasonable.

3.6 Systematic Errors for the Inclusive Yield

This section details the estimation of systematic errors associated with the yield of inclusive electrons.

3.6.1 Rungroup Correction

The scaling done between the yield in different rungroups, cuts, and with/without the ES sector (sufferring from the RICH alignment problem), relies on the assumption that the ratio in Figure 3.9 is independent of p_T. Also, as described in Subsection 3.5.1, the statistical errors of the ratio of yields goes into the systematic error on the fit. The statistical errors from 1 to 4 GeV/c in p_T in Figure 3.9 warrant an error of less than 0.5%, but we increase the systematic error due to this scaling to 1% in case the assumption of p_T-independence of the ratio at high p_T is not perfectly precise.

3.6.2 Geometrical Acceptance

The G9 rungroup was used as the standard rungroup from which to calculate the single track efficiency since the dead/live area in this rungroup was stable compared to that of other rungroups. The GEANT-based simulation was tuned to have the same dead area as one of the runs in the G9 rungroup. However, the dead area in the G9 rungroup was not perfectly stable across runs. We want to estimate the systematic error due to the instability in dead area in the G9 rungroup, and the ability of the simulation to perfectly reproduce the dead area in a given run. To estimate the relevant error, we integrate the $dN/d\phi$ distribution, shown in Figure 3.3, over the west arm, both in data and simulation. We scale the simulation $dN/d\phi$ such that the integral over the west arm is the same as that in data. We then compare the integral over the east north section of $dN/d\phi$ in data with that of the the scaled $dN/d\phi$ in simulation. The east south is avoided since it is affected by the RICH alignment bug. The difference between the east north in data and simulation using this procedure is 3.7%, which we round up to 4% to be conservative.

3.6.3 Electron Identification Cuts

Determining the systematic error due to the assumption that the simulation accurately reproduces the response of the raw electron yield with respect to varying electron identification cuts is a tricky business. No matter what semi-quantitative means are used to estimate this error, there will remain the analyzer's opinion of how well the detector response is understood. One can look at electrons from beampipe conversions, as was outlined in Section 3.5.2, and see how the efficiency changes as the cuts change. But to get a sample of electrons, some cuts must already be applied to the tracks, and one returns to the problem of guessing just how well the simulation reproduces the detector response for these loose identification cuts.

And then, there is the RICH misalignment bug, mentioned often in this document as source of confusion for this analysis. Even though the east south region of the detector is more affected by this bug than are the other region, no part of the detector is immune from this problem. The effect of using the wrong alignment of the RICH in the track reconstruction grows as the RICH cuts tighten, so we do not trust the simulation to give us the efficiency when tight electron identification cuts are used. One strategy used to get around this is to attempt to emulate the RICH misalignment in the simulation track reconstruction. Such emulation was implemented, and although the distribution of the `n0` and `n1` variables in the data can be reproduced, the track

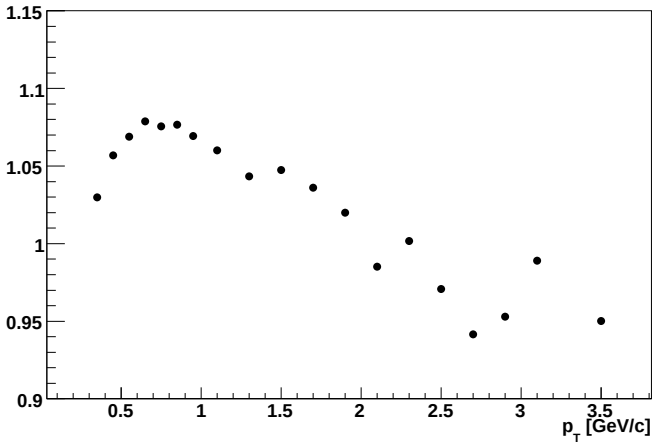

Figure 3.11: Ratio of inclusive 60-92% centrality invariant yield using normal cuts (see text), to that using the loose cuts. The RICH misalignment was emulated in the efficiency correction.

eID cuts
n0 > 2
$\sqrt{\text{emcsdphi\_e}^2 + \text{emcsdz\_e}^2} < 4.0$
disp < 10.0
chi2/npe0 < 20.0
prob > 0.001

Table 3.7: Differences between the loose and normal cuts eID cuts.

displacement from the ring, disp, and the quality of ring-shape, chi2/npe0, are not reproduced well by the RICH misalignment emulation procedure.

Figures 3.11 and 3.12 show the ratio of the 60-92% centrality invariant yield if different cuts are made to obtain both a raw yield and the efficiency correction. Here, normal cuts refer to the cuts used in the standard analysis for p_T below 5 GeV/c, and tight cuts are the cuts used in the analysis for p_T above 5 GeV/c. The differences between the loose cuts and the normal cuts are shown in table 3.7. For Figures 3.11 and 3.12, the acceptance $\times$ efficiency correction was calculated using the RICH misalignment emulation procedure mentioned above. Figures 3.13 and 3.14 show the ratio of invariant yields for different cuts, but not using the RICH misalignment emulation. From Figure

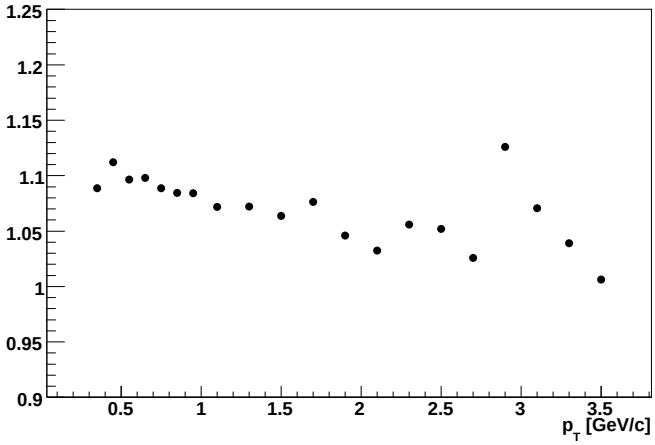

Figure 3.12: Ratio of inclusive 60-92% centrality invariant yield using normal cuts (see text), to that using the tight cuts. The RICH misalignment was emulated in the efficiency correction.

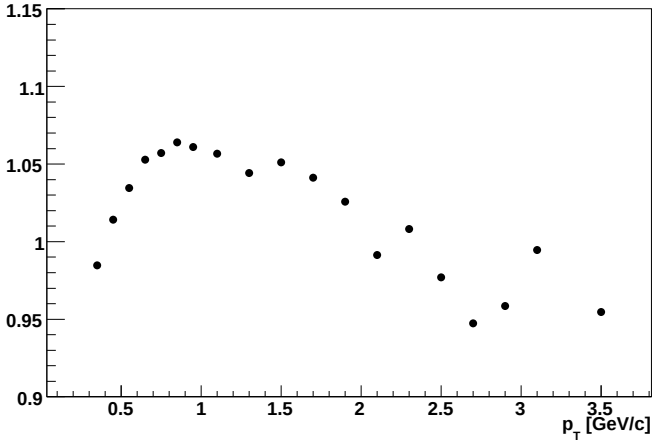

Figure 3.13: Ratio of inclusive 60-92% centrality invariant yield using normal cuts (see text), to that using the loose cuts.

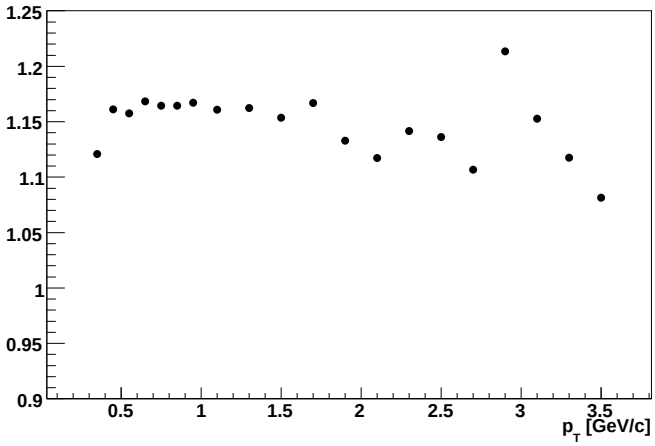

Figure 3.14: Ratio of inclusive 60-92% centrality invariant yield using normal cuts (see text), to that using the tight cuts.

3.14 one can see that when the RICH cut is tightened, the efficiency correction from the simulation becomes unreliable. By looking at the variation in the inclusive spectra using various cuts, and keeping in mind the subtle problems associated with the RICH misalignment emulation in the efficiency simulation, a systematic error of 6% was assigned to the inclusive electron yield. This error implicitly contains the error due to the finite statistics used in the simulation, which from Figure 3.8 can be seen to be small.

For the multiplicity-dependent efficiency loss, the proportional systematic error is taken to be $|\epsilon^{\mathrm{embed},C} - \epsilon^{\mathrm{data},C}_{\mathrm{mult}}\epsilon^{\mathrm{embed},C}_{\mathrm{loose}}|/\epsilon^{\mathrm{embed},C}$ given in Table 3.6.

Origin of error	Relative error
rungroup correction	1%
geometrical acceptance	4%
electron identification	6%
embedding efficiency	$\sim$ 4%

Table 3.8: Summary of systematic errors on the inclusive electron yield.

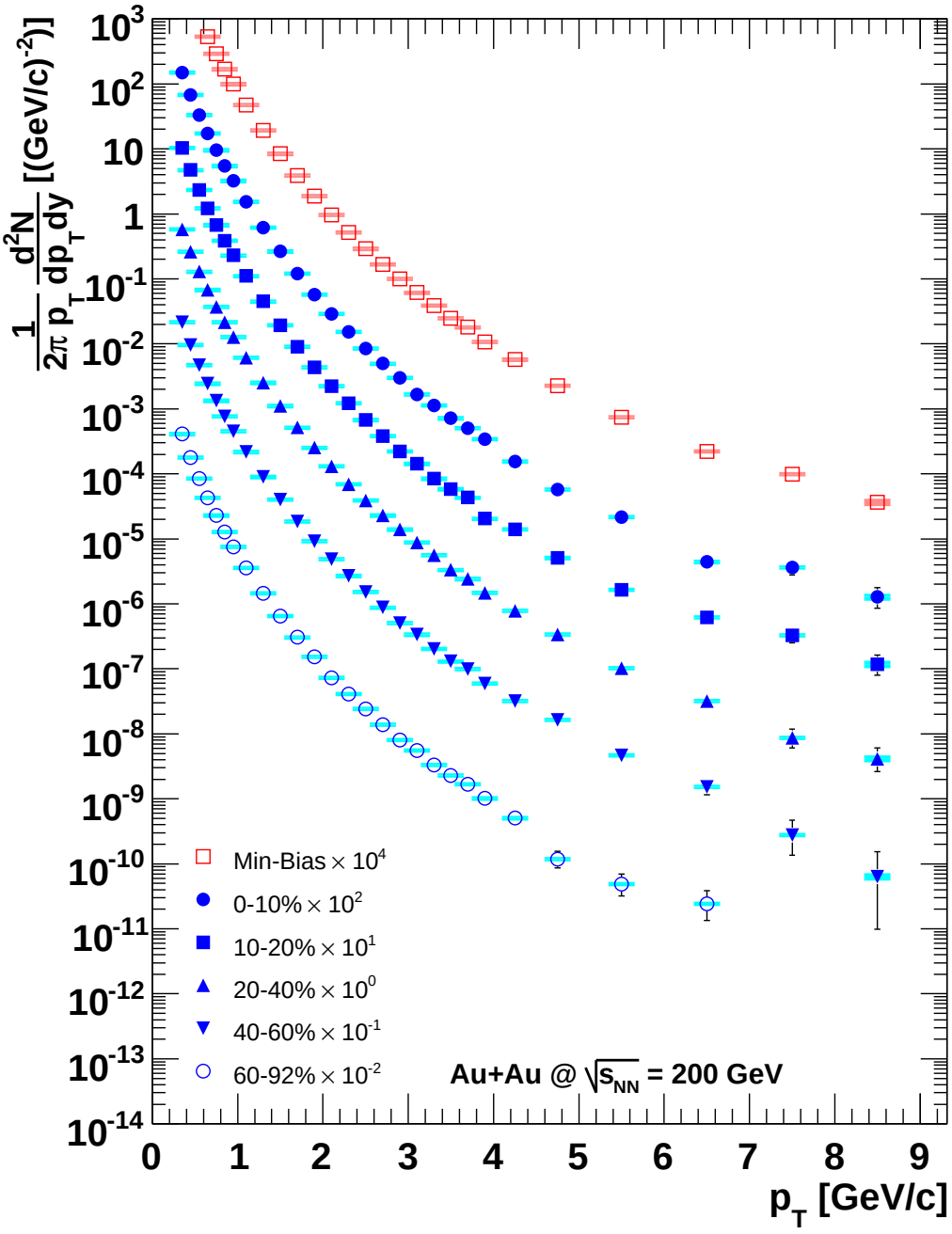

Figure 3.15: Invariant differential yield of inclusive $\frac{e^+ + e^-}{2}$, for various centrality bins. The yield for various centralities have been scaled by powers of 10 for clarity.

3.7 Inclusive Invariant Yield of $\frac{e^+ + e^-}{2}$

The preceeding sections in this chapter outlined the procedure to obtain the invariant yield of inclusive electrons. The differential invariant yield of electrons and positrons is shown in Figure 3.15. In order to obtain the yield of electrons due to decays of hadrons containing open heavy flavor, the electron yield from other sources must be determined and subtracted. This electron background determination is the subject of the next chapter.

3.8 Electron Yield with Respect to the Reaction Plane

The first step in obtaining the v_2 parameter of Equation 1.3 for electrons from heavy flavor decays is to measure v_2 for inclusive electrons. Given the reaction plane angle Ψ, all we need to do is repeat the above analysis methods for the electron yield, but separated into bins of $\phi - \Psi$, where ϕ is the azimuthal angle of the electron track projection through the magnetic field to the collision vertex. Then we can perform a fit to the resulting $dN/d\phi$ of the form of Equation 1.3 to obtain v_2.

3.8.1 Reaction Plane Measurement

The reaction plane is estimated using the method outlined in [26, 27]. The two beam-beam counters are used independently to measure the reaction plane, as they are far separated in rapidity from each other, and from the electrons which we measure, and thus the measurement avoids auto-correlation effects related to measuring the separtion of a particles from the reaction plane, when that particle is used to determine the reaction plane [26]. Instead of summing over particles, as in the above references, a sum is made over the 64 BBC PMTs weighted by the charge on each PMT:

$$Q_y \equiv \sum_{i=1}^{64} w_i \sin(2\phi_i) \tag{3.15}$$

$$Q_x \equiv \sum_{i=1}^{64} w_i \cos(2\phi_i) \tag{3.16}$$

$$\Psi_{\text{obs}} = \frac{\tan^{-1}\left(Q_y/Q_x\right)}{2} \tag{3.17}$$

where ϕ_i is the azimuthal angle of PMT i and w_i is the charge measured in PMT i. Due to detector acceptance and dead-area, the distribution of $\Psi_{\rm obs}$ is not flat, as the true reaction plane distribution should be. To correct for these effects, we flatten the distribution as

$$Q_y^{\rm corr} \equiv \frac{Q_y - \langle Q_y \rangle}{\sigma_y} \tag{3.18}$$

$$Q_x^{\rm corr} \equiv \frac{Q_x - \langle Q_x \rangle}{\sigma_x} \tag{3.19}$$

$$\Psi_{\rm corr} = \frac{\tan^{-1}\left(Q_y^{\rm corr}/Q_x^{\rm corr}\right)}{2} \tag{3.20}$$

where $\langle Q_{y,x} \rangle$ and $\sigma_{y,x}$ are the mean and standard deviation of the distributions of $Q_{y,x}$. The correction is applied separately for 10% centrality bins as the distribution of $Q_{y,x}$ broadens with centrality. After this correction, the distribution of $\Psi_{\rm corr}$ is still not exactly flat. We provide an additional *ad hoc* flattening by approximating the fluctuations by a Fourier expansion:

$$\Delta\Psi \equiv \sum_k (A_k {\rm cos}(2k\Psi_{\rm corr}) + A_k {\rm sin}(2k\Psi_{\rm corr})) \tag{3.21}$$

$$A_k \equiv -\frac{2}{k}\langle {\rm sin}(2k\Psi_{\rm corr})\rangle \tag{3.22}$$

$$B_k \equiv -\frac{2}{k}\langle {\rm cos}(2k\Psi_{\rm corr})\rangle \tag{3.23}$$

$$\Psi = \Psi_{\rm corr} + \Delta\Psi \tag{3.24}$$

where the exansion degree k runs from 0 to 20. These calibrations of the reaction plane were performed separately for each run.

3.8.2 Reaction Plane Resolution

The Fourier coefficient v_2 in the expansion of the azimuthal particle distribution with respect to the real reaction plane can be expressed in terms of the observed v_2 from the distribution with respect to the measured reaction plane as [26, 27]

$$v_2 = \frac{v_2^{\rm meas}}{\langle {\rm cos}(2(\Psi_{\rm meas} - \Psi_{\rm true}))\rangle}. \tag{3.25}$$

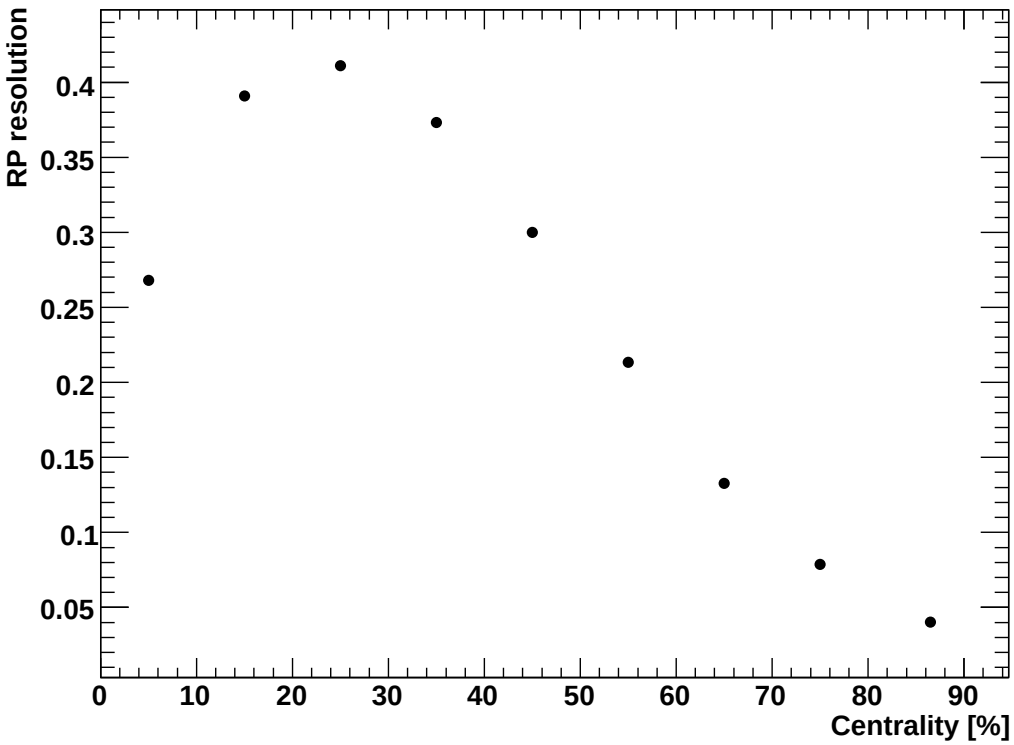

Figure 3.16: Reaction plane resolution as a function of centrality.

Two methods were used to extract $\langle\cos(2(\Psi_{\rm meas} - \Psi_{\rm true}))\rangle$. The first is an analytical calculation [26, 27]

$$\langle\cos(2(\Psi_{\rm meas} - \Psi_{\rm true}))\rangle = \frac{\sqrt{\pi}}{2\sqrt{2}}\chi\exp(-\chi^2/4)[I_0(\chi^2/4) + I_1(\chi^2/4)] \qquad (3.26)$$

where χ is equal to $v_2^{\rm meas}\sqrt{2N}$, and N is the BBC multiplicity. This method was verified to be well approximated by [27]

$$\langle\cos(2(\Psi_{\rm meas} - \Psi_{\rm true}))\rangle \sim \sqrt{2\langle\cos(2(\Psi^N_{\rm meas} - \Psi^S_{\rm meas}))\rangle} \qquad (3.27)$$

with $\Psi^{N(S)}_{\rm meas}$ is the measured reaction plane using only the north (south) BBC. Figure 3.16 shows the reaction plane resolution determined from Equation 3.27.

3.8.3 Inclusive Electron v_2

The v_2 for a given centrality bin $[a, b]$ can be expressed as

$$v_2^{\text{bin}} = \frac{\int_a^b \frac{v_2^{\text{meas}}(C)\frac{dN_{e^+,e^-}}{dC}}{\text{res}(C)} dC}{\int_a^b \frac{dN_{e^+,e^-}}{dC} dC}. \tag{3.28}$$

Due to lack of statistics, Equation 3.28 was approximated by a Riemann sum over 10% centrality bins. It was verified that v_2 is not sensitive to changing the bins for the Riemann sum. This is because the integrand in the numerator of Equation 3.28 is quite flat with centrality, as the resolution grows with both the measured v_2 and the particle multiplicity. The v_2 for a given centrality bin was obtain by dividing the electron yield into 12 bins in $\phi - \Psi$, and fitting to a curve with the form of Equation 1.3 (See Figure 3.17). The systematic error for the inclusive electron v_2 is quite small. There is very little error due to the electron measurement, as most of the uncertainties are scaling uncertainties, and normalization does not effect the value of v_2. A 5% error was assigned to the determination of the reaction plane resolution, determined from the difference in Ψ as determined by the north and south BBC. The statistical error on v_2 from the fitting at high p_T is quite substantial. As this error is independent of the reaction plane measurement, the reaction plane resolution amplifies the statistical error.

Figure 3.18 shows the inclusive electron v_2 for various centrality bins.

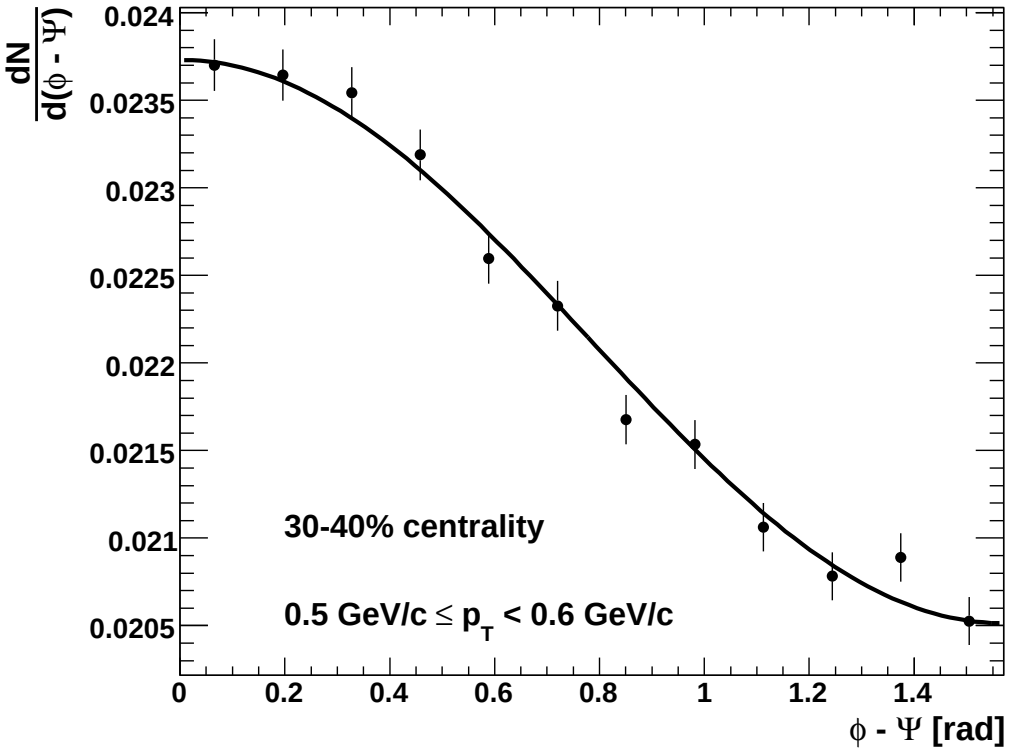

Figure 3.17: $\frac{dN}{d(\phi - \Psi)}$ of $\frac{e^+ + e^-}{2}$ for 30-40% centrality and 0.5 GeV/$c \leq p_T$ $<$ 0.6 GeV/c. The fit to the form of Equation 1.3 is shown as well.

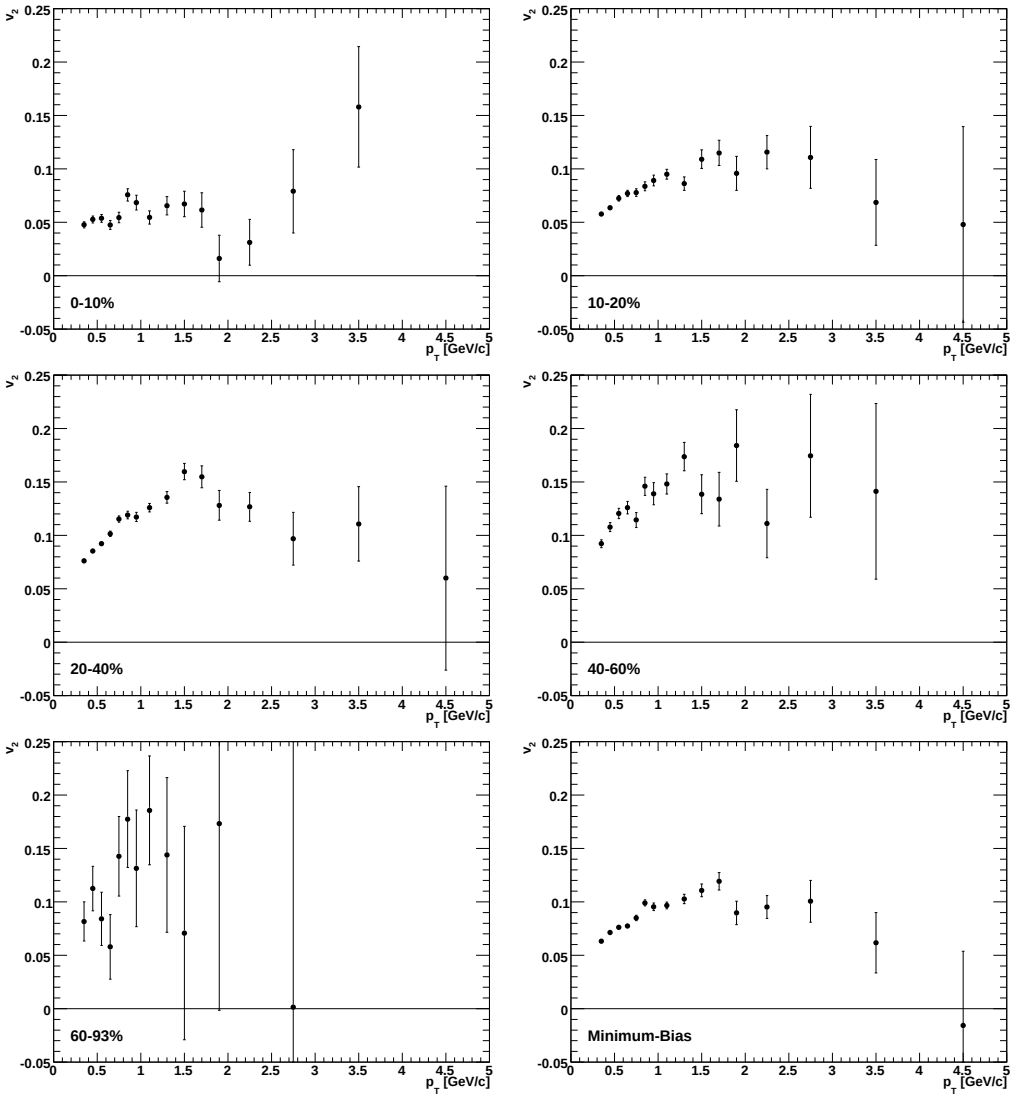

Figure 3.18: The inclusive e^+, e^- v_2 for various centrality bins. A 5% systematic error is not shown.

Chapter 4

Estimation of Electron Background from Photonic Sources

After measuring the invariant yield of inclusive electrons, we want to estimate how much of that yield is due to electrons from semileptonic decay of open heavy flavor mesons by subtracting all other contributions to the electron yield. Two methods were used to estimate the electron background. One method, called the cocktail method, uses PHENIX measurements of electron decay sources to estimate electron background. The other method, called the converter method, involves wrapping a brass sheet around the beampipe to increase the electron yield from photon conversions in material. From the increase in photon conversions with the converter installed, the yield from photon converions and Dalitz decays when the converter is not installed can be deduced.

4.1 Cocktail Method

4.1.1 Introduction

The electron background rate estimation is performed using the EXODUS cocktail generator [53]. The procedure to simulate the "cocktail" of background electrons is as follows:

- Simulate Dalitz decays of light mesons [54].
- Use a realistic input momentum distribution of the mesons using the

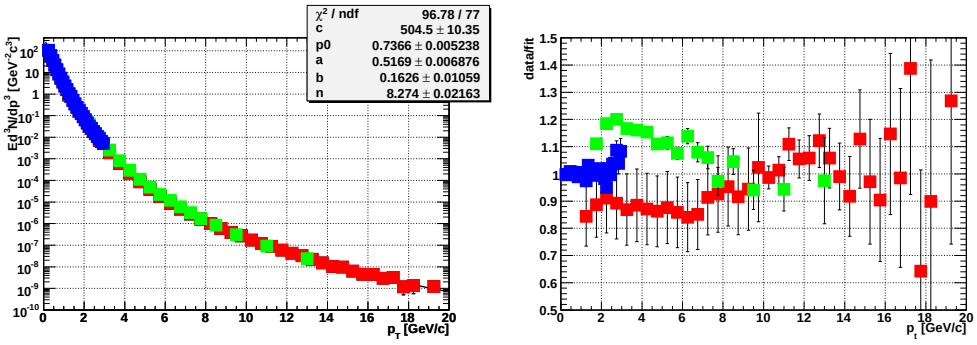

Figure 4.1: Invariant multiplicity of charged pions (blue symbols at low p_T) and neutral pions from Run-2 (green symbols) and Run-4 (red symbols) together with a fit according to Eq. 4.1 (left panel). Ratio of the data to the fit (right panel).

measured π^0 spectrum. The distribution of higher mass mesons is obtained by assuming m_T scaling.

- Determine the rate of electrons from photon conversions using the ratio of conversion electrons to Dalitz electrons found in a full GEANT-based simulation of PHENIX.

4.1.2 Cocktail Input

Neutral pions

The most important cocktail input is the invariant differential multiplicity of neutral pions. This is obtained by a simultaneous fit to the charged pion spectrum from [61] and the neutral pion spectra from [57, 58] with a modified Hagedorn parameterization:

$$E\frac{d^3N}{d^3p} = \frac{c}{(\exp(-ap_T - bp_T^2) + p_T/p_0)^n} \tag{4.1}$$

Fig. 4.1 shows the resulting fit for minimum bias collisions, including the parameters that are used in the subsequent cocktail calculation, and the ratio of the data to the fit. It is obvious that the preliminary neutral pion spectrum from Run-4 is systematically different from the published Run-2 result for $p_T < 8$ GeV/c. To make sure that we do not bias our fit towards the Run-4 spectrum we use total errors for the Run-4 spectrum below 10 GeV/c and statistical errors elsewhere. Otherwise the superior statistics available from

centrality	c $[(\mathrm{GeV/c})^{-2}]$	a $[(\mathrm{GeV/c})^{-1}]$	b $[(\mathrm{GeV/c})^{-2}]$	p_0 [GeV/c]	n	$\mathrm{dN}_{\pi^0}/\mathrm{dy}$
min. bias	504.5	0.5169	0.1626	0.7366	8.274	95.7
0 - 10 %	1331.0	0.5654	0.1945	0.7429	8.361	280.9
10 - 20 %	1001.0	0.5260	0.1628	0.7511	8.348	200.6
20 - 30 %	750.7	0.4900	0.1506	0.7478	8.299	140.5
30 - 40 %	535.3	0.4534	0.1325	0.7525	8.333	93.8
40 - 50 %	364.5	0.4333	0.1221	0.7385	8.261	59.2
50 - 60 %	231.2	0.4220	0.1027	0.7258	8.220	35.0
60 - 70 %	118.1	0.4416	0.0559	0.7230	8.163	17.9
70 - 80 %	69.2	0.2850	0.0347	0.7787	8.532	8.8
80 - 92 %	51.1	0.2470	0.0619	0.7101	8.453	5.0

Table 4.1: Fit parameters for the neutral pion invariant p_t distributions according to Eq. 4.1. In addition, the last column gives the integrated neutral pion yield corresponding to the parametrization.

Run-4 would completely dominate the fit. The remaining difference between our fit and both the Run-2 and preliminary Run-4 pion spectra is unfortunate but unavoidable and we assign a systematic error (see below) to the resulting electron cocktail to accommodate for this ambiguity.

The corresponding fits to the pion spectra in all centrality classes are shown in Figs. 4.2 and 4.3 and the fit parameters are summarized in Tab. 4.1.

centrality	c $[(\mathrm{GeV/c})^{-2}]$	a $[(\mathrm{GeV/c})^{-1}]$	b $[(\mathrm{GeV/c})^{-2}]$	p_0 [GeV/c]	n	$\mathrm{dN}_{\pi^0}/\mathrm{dy}$
min. bias	542.9	0.5289	0.1715	0.7223	8.165	102.7
0 - 10 %	1432.0	0.5758	0.2038	0.7301	8.257	301.3
10 - 20 %	1073.0	0.5346	0.1663	0.7420	8.271	215.1
20 - 30 %	802.9	0.4990	0.1516	0.7393	8.225	150.5
30 - 40 %	571.6	0.4612	0.1306	0.7458	8.267	100.5
40 - 50 %	389.0	0.4405	0.1189	0.7325	8.198	63.4
50 - 60 %	236.4	0.4267	0.0960	0.7227	8.169	36.0
60 - 70 %	124.9	0.4392	0.0441	0.7277	8.145	19.1
70 - 80 %	75.8	0.2668	0.0330	0.7845	8.533	9.5
80 - 92 %	56.0	0.2214	0.0602	0.7209	8.486	5.4

Table 4.2: Fit parameters for the neutral pion invariant p_t distributions according to Eq. 4.1 after moving all charged and neutral pion data points up by their systematic uncertainties. In addition, the last column gives the corresponding integrated neutral pion yield.

centrality	c $[(\mathrm{GeV/c})^{-2}]$	a $[(\mathrm{GeV/c})^{-1}]$	b $[(\mathrm{GeV/c})^{-2}]$	p_0 [GeV/c]	n	$\mathrm{dN}_{\pi^0}/\mathrm{dy}$
min. bias	465.9	0.5004	0.1514	0.7567	8.427	88.8
0 - 10 %	1332.0	0.5368	0.2534	0.7301	8.400	263.1
10 - 20 %	929.0	0.5150	0.1585	0.7632	8.449	186.2
20 - 30 %	698.3	0.4787	0.1491	0.7591	8.399	130.3
30 - 40 %	498.8	0.4439	0.1343	0.7616	8.420	87.1
40 - 50 %	339.7	0.4244	0.1253	0.7469	8.346	55.0
50 - 60 %	216.0	0.4153	0.1099	0.7312	8.294	32.5
60 - 70 %	111.3	0.4405	0.0690	0.7208	8.203	16.7
70 - 80 %	62.2	0.3028	0.0355	0.7780	8.560	8.0
80 - 92 %	46.0	0.2776	0.0642	0.6995	8.426	4.6

Table 4.3: Fit parameters for the neutral pion invariant p_t distributions according to Eq. 4.1 after moving all charged and neutral pion data points down by their systematic uncertainties. In addition, the last column gives the corresponding integrated neutral pion yield.

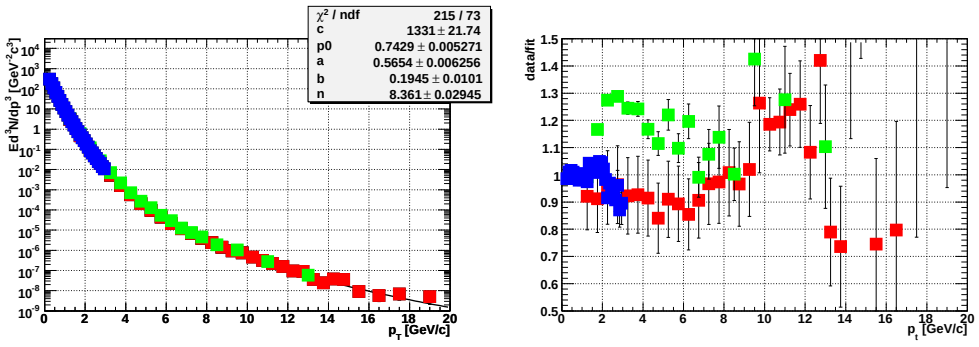

Figure 4.2: Invariant multiplicity of charged pions (blue symbols at low p_T) and neutral pions from Run-2 (green symbols) and Run-4 (red symbols) together with a fit according to Eq. 4.1 for the centrality class of 0-10% (left panels). Ratio of the data to the fit (right panels).

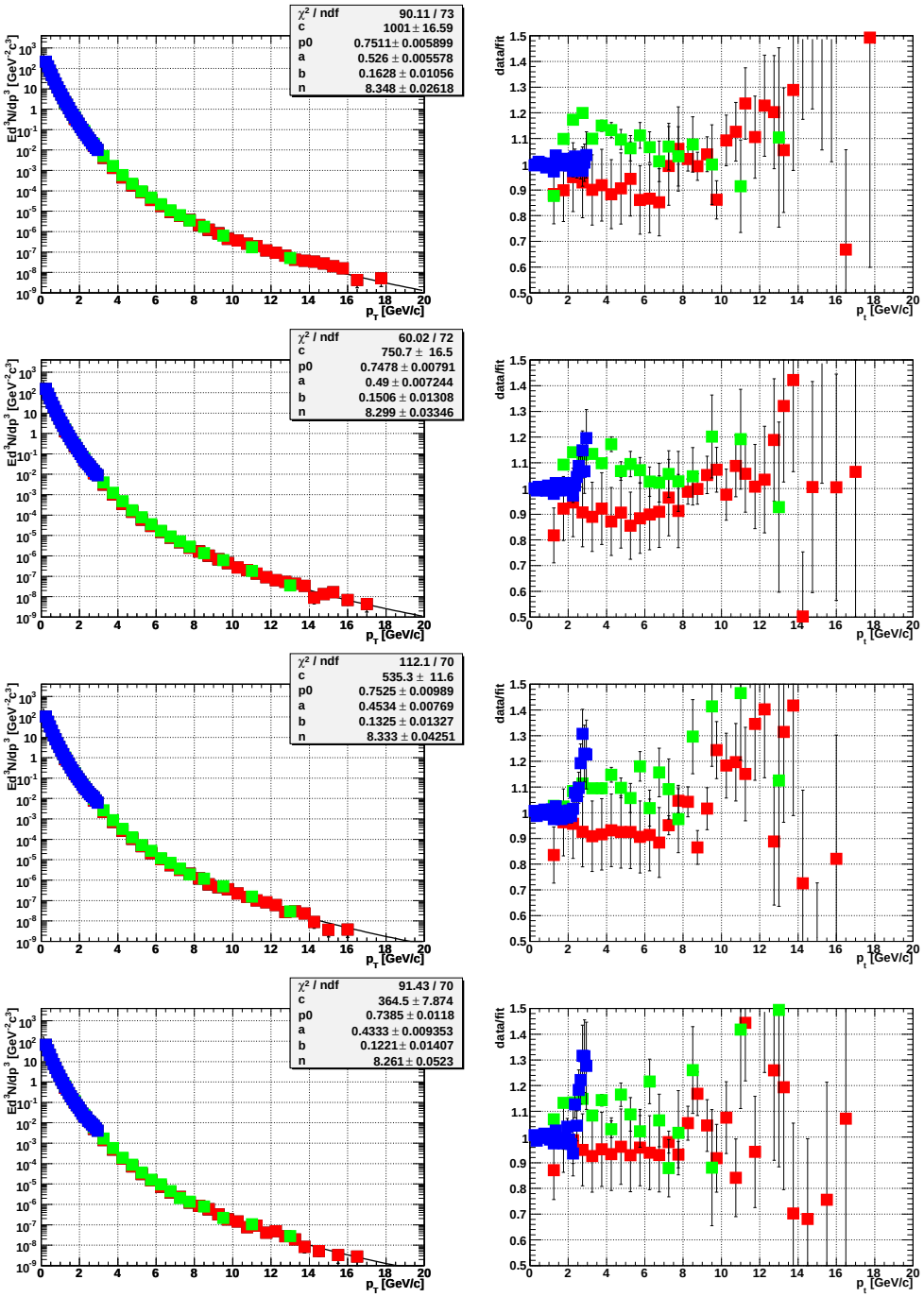

Figure 4.3: Invariant multiplicity of charged pions (blue symbols at low p_T) and neutral pions from Run-2 (green symbols) and Run-4 (red symbols) together with a fit according to Eq. 4.1 for the centrality classes (from top to bottom) 10-20 %, 20-30 %, 30-40 %, and 40-50% (left panels). Ratio of the data to the fit (right panels).

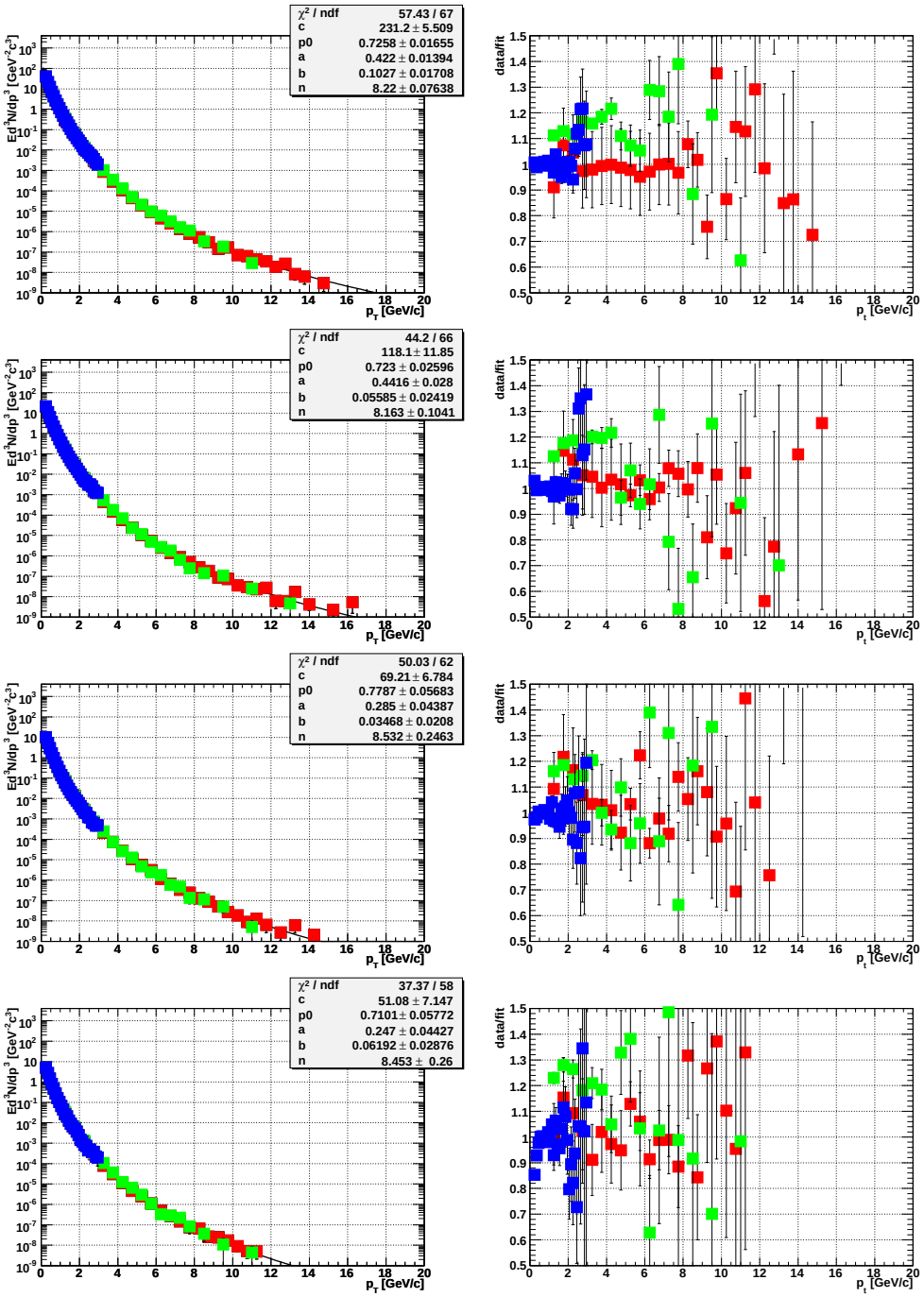

Figure 4.4: Invariant multiplicity of charged pions (blue symbols at low p_T) and neutral pions from Run-2 (green symbols) and Run-4 (red symbols) together with a fit according to Eq. 4.1 for the centrality classes (from top to bottom) 50-60%, 60-70%, 70-80%, and 80-92% (left panels). Ratio of the data to the fit (right panels).

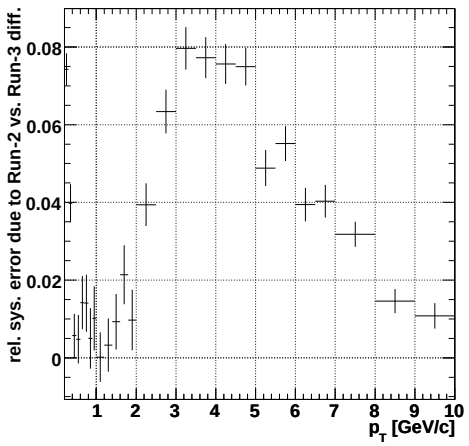

Figure 4.5: Systematic cocktail error introduced through the systematic difference between π^0 spectra from Run-2 [57] and Run-4 [58].

To evaluate the sys. error related to the pion input first the fits are repeated with all data points moved up/down by their individual sys. uncertainties. Repeating the full cocktail calculations with the resulting parameterizations defines a $\pm 1\sigma$ uncertainty band for the pion input. This procedure is exactly the same as was done for earlier cocktails and we don't explicitly show the corresponding fits to the pion spectra after moving them up/down by the systematic errors here. However, tables 4.2 and 4.3 list the resulting fit parameters used for the systematic error evaluation.

To assign a sys. uncertainty due to the discrepancy between the Run-2 and Run-4 input the full cocktail calculation is repeated with only the Run-2 and Run-4 spectra, respectively, as input and compared to the cocktail with the combined input. The resulting relative systematic error is shown in Fig. 4.5 and it is included in the total systematic error discussed below.

Other light mesons

Other light mesons contributing to the electron cocktail are the η, ρ, ω, η', and ϕ mesons, but only the η meson plays a significant role.

The shape of the invariant p_T distributions and the relative normalization to the π^0 are required as input parameters. The p_T spectra are determined from the pion spectrum by m_T scaling, *i.e.* the same modified Hagedorn parameterization is used (Eq. 4.1), only p_T is replaced by $\sqrt{p_T^2 + m_{meson}^2 - m_{\pi^0}^2}$. The resulting ratio η/π^0 agrees well for $p_T > 2$ GeV/c with corresponding

PHENIX data.

The relative normalization to the pion is given by the ratios meson-to-pion at high p_T (5 GeV/c is used here). The following values are used:

- $\eta/\pi^0 = 0.48 \pm 0.10$ [59]
- $\rho/\pi^0 = 1.00 \pm 0.30$ [53]
- $\omega/\pi^0 = 0.90 \pm 0.27$ [60]
- $\eta'/\pi^0 = 0.25 \pm 0.075$ [53]
- $\phi/\pi^0 = 0.40 \pm 0.12$ [53]

Photon conversions

The contribution from photon conversions depends almost entirely on the material present in the detector aperture. As was shown in a full GEANT simulation of π^0 decays the ratio of electrons from the conversion of photons from $\pi^0 \to \gamma\gamma$ decays to electrons from π^0 Dalitz decays is 0.403 with a systematic uncertainty of 10 %, independent of p_T in the range relevant for this analysis. For other mesons, this ratio is rescaled to properly account for the fact that the branching ratio for the Dalitz decay relative to the $\gamma\gamma$ decay grows slightly with increasing parent meson mass.

Kaon decays: K_{e3}

The contribution from the K_{e3} decay of Kaons in flight can only be determined via a full GEANT simulation, taking into account the exact electron ID cuts in addition. The default cocktail includes a parameterization obtained for the p+p Run-2 cocktail [62], which is in reasonable agreement with the data. The momentum of the electrons from K_{e3} decay are typically reconstructed too high, since the decay takes place outside of the PHENIX magentic field. As a result, the reconstruction efficiency of these electrons is very small since they do not pass the E/p cut, and the contribution of K_{e3} decays to the cocktail is small even at low p_T.

Direct radiation

Contributions to the cocktail from virtual direct photons and from the conversion of real direct photons are derived from the measured real direct photon spectra as published in [63] and shown in Fig 4.6 for minimum bias data. Since we use the very same shape of the direct photon spectrum and scale the total

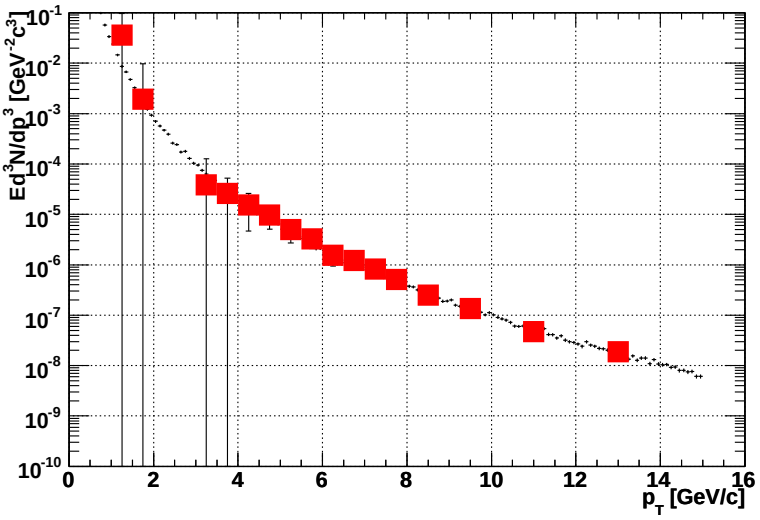

Figure 4.6: Measured direct photon spectrum (large symbols shown in red) compared with the cocktail parameterization (histogram indicated by small 'data points' for minimum bias Au+Au collisions.

yield according to the number of binary collisions, which is supported by the data [63], the agreement between data and parameterization is comparably reasonable for all centrality classes.

The ratio of virtual direct photons to real direct photons depends on p_T because the phase space for dielectron emission increases. The same effect is seen in the Dalitz decays of light neutral mesons, *i.e.* the Dalitz branching ratio relative to the two photon decay branching ratio is larger for the η meson than for the π^0. Since direct radiation is implemented in the cocktail via the decay of modified π^0 with a p_T distribution that gives rise to a photon spectrum consistent with the measured direct photon spectrum, it is important to treat the relative Dalitz branching ratio of this modified π^0 appropriately. What was done up to now was to increase the relative Dalitz branching ratio, which results in the electron spectrum from virtual direct radiation, to the value for the η meson. This is sufficiently accurate for electron spectra up to 5 GeV/c in p_T but underestimates the virtual direct photon yield at high p_T. Therefore, we have implemented a p_T dependent relative branching ratio (Dalitz relative to two photon) for the modified π^0 which follows the expected logarithmic dependence on the parent mass which, in this case, is the virtual photon p_T. The difference between the original and the improved direct radiation implementation in the cocktail is not large, *i.e.* at the highest electron p_T

considered here (9 GeV/c), the improvement leads to an increase in the total cocktail yield of about 20% which is large enough to justify the improved treatment.

The improved handling of direct radiation was also implemented for the Run-5 p+p cocktail [64]. This is of particular importance since the electron spectra from that analysis provide the denominator for the R_{AA} analysis presented in this analysis.

4.1.3 Final Run-4 Electron Cocktails

The resulting electron cocktails for Run-4 Au+Au collisions at 200 GeV are shown in Figs. 4.7 and 4.8.

4.2 Converter Method

4.2.1 Introduction

The goal of the converter method is to extract the relative yield of photonic electrons to the yield of non-photonic electrons. By photonic electrons, we mean electrons from conversions of photons in material and from Dalitz decays. We define the yield of photonic electrons with the converter removed as N_γ, the yield of non-photonic electrons as $N_{\rm non}$, the total electron yield without the converter as $N_{\rm inc}$, and the total electron yield with the converter installed as $C_{\rm inc}$. The ratio of the yield of photonic electrons with the converter installed to that with the converter removed is called R_γ. $C_{\rm inc}$ and $N_{\rm inc}$ can be expressed as

$$C_{\rm inc} = R_\gamma N_\gamma + N_{\rm non} \tag{4.2}$$

$$N_{\rm inc} = N_\gamma + N_{\rm non}. \tag{4.3}$$

N_γ and $N_{\rm non}$ obey the relations:

$$N_\gamma = \frac{C_{\rm inc} - N_{\rm inc}}{R_\gamma - 1} \tag{4.4}$$

$$N_{\rm non} = \frac{R_\gamma N_{\rm inc} - C_{\rm inc}}{R_\gamma - 1}. \tag{4.5}$$

We need to determine R_γ in order to obtain $N_{\rm non}$ using the above relations. The strategy is to simulate π^0 photonic decays in a GEANT detector simulation with and without the converter installed to determine the increase of photonic electrons with the converter installed due to photons from π^0 decays.

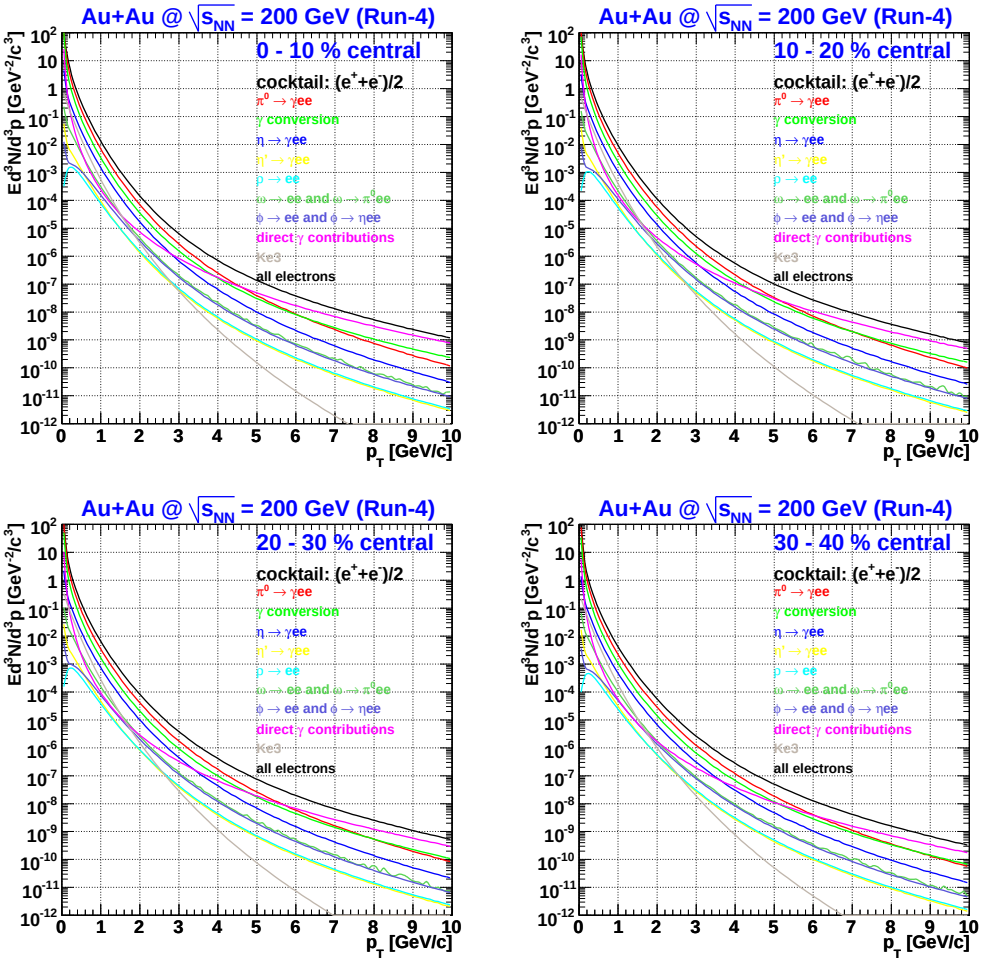

Figure 4.7: Invariant differential multiplicities of electrons from all sources considered in the Au+Au Run-4 cocktails.

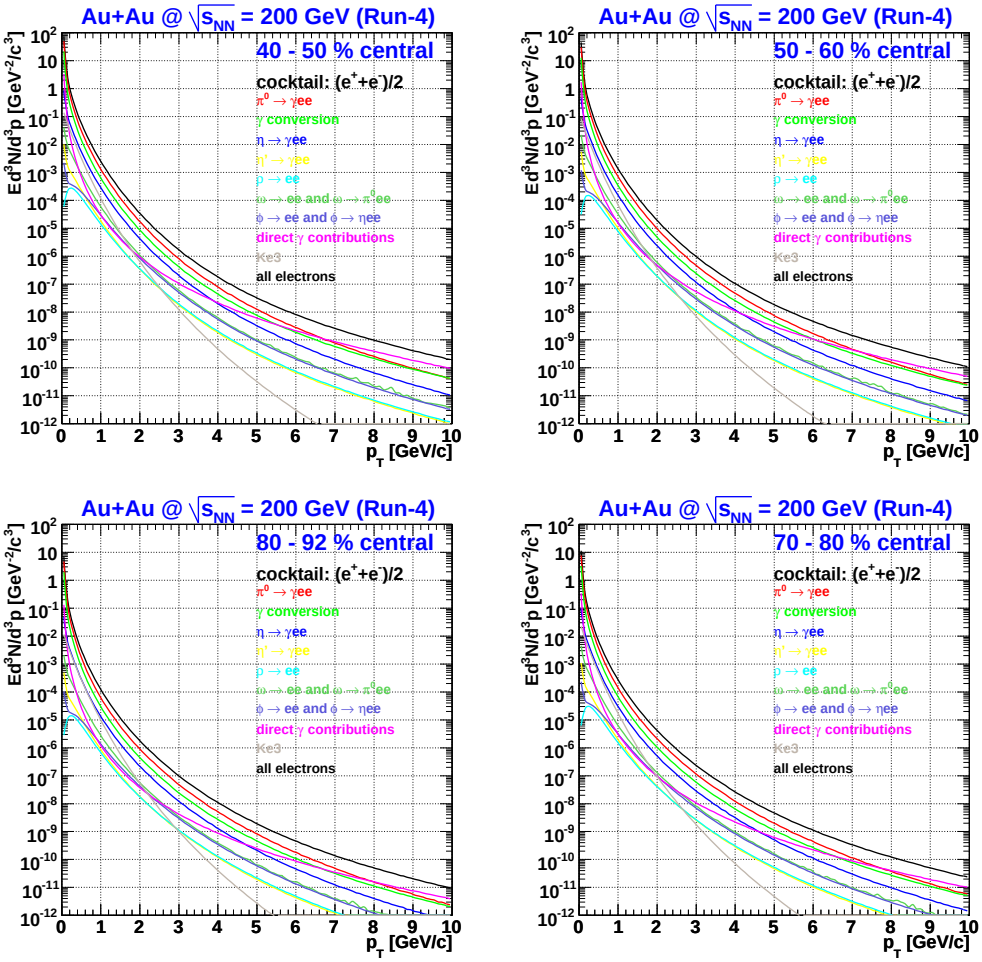

Figure 4.8: Invariant differential multiplicities of electrons from all sources considered in the Au+Au Run-4 cocktails

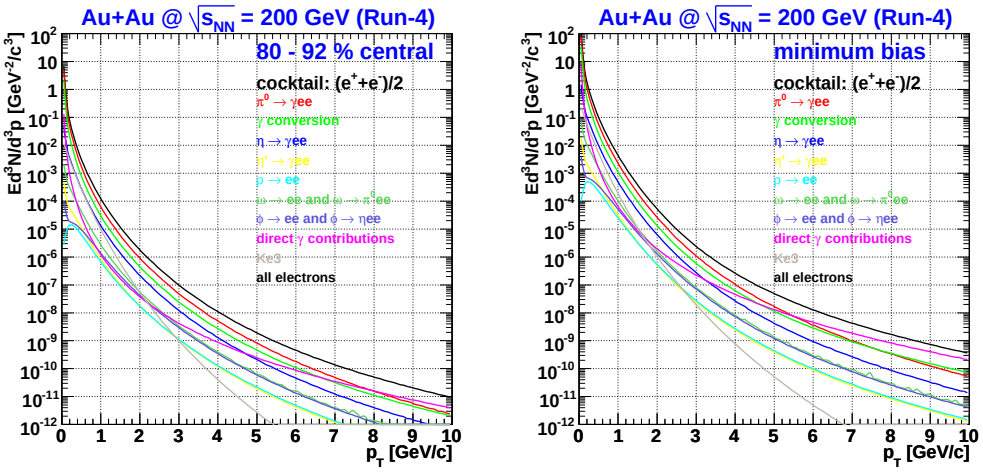

Figure 4.9: Invariant differential multiplicities of electrons from all sources considered in the Au+Au Run-4 cocktails

The electron yield increase due to photons from decays of other hadrons is then estimated.

4.2.2 The Photon Converter

The converter is a 0.0254 cm thick brass sheet. The composition of the converter is 70% Cu, 29.88% Zn, 0.07% Pb, and 0.05% Fe, with an ideal mass density of 8.5 g/cm^3. The sheet is wrapped into a cylinder around the beampipe with an inner radius of 3.85 cm and a length of 60.96 cm. The density of the sheet was measured, by measuring the area, thickness, and mass of the entire sheet, to be 8.4769 g/cm^3. The ideal value of 8.5 g/cm^3 was used as input for the GEANT simulation.

4.2.3 Photonic Electron Yield from π^0 Simulation

Neutral pions were input into a GEANT-based simulation of PHENIX with and without the converter installed using initial π^0 p_T distributions from fits

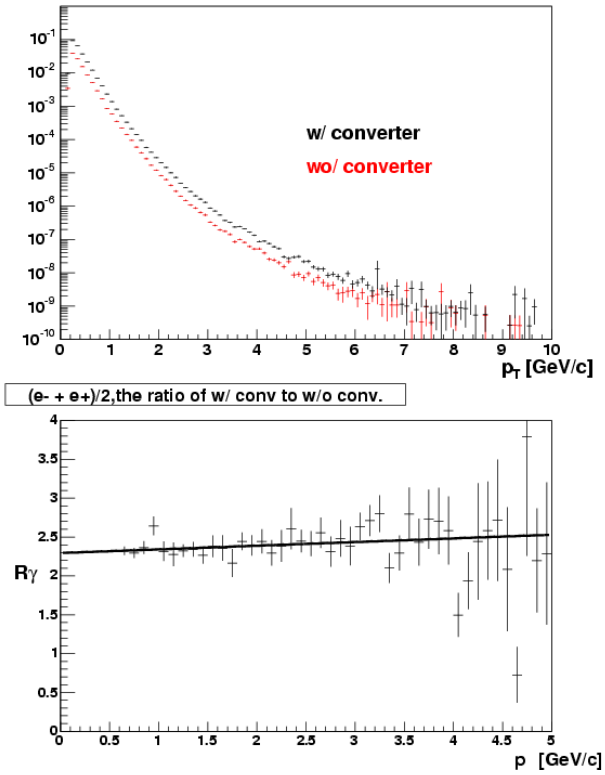

Figure 4.10: Top: The photonic electron yield from the π^0 simulation in units of $(c/\mathrm{GeV})^2$ with and without the converter installed. Bottom: The ratio of the $(e^+ + e^-)/2$ yield with the converter installed to that without the converter installed.

to the PHENIX Run2 π^0 measurement:

$$\frac{1}{2\pi p_T}\frac{d^2N}{dp_T dy} = 416.54[c^2/\mathrm{GeV}^2] \cdot (1 + p_T/(2.3260[\mathrm{GeV}/c]))^{-13.887}, \quad (4.6)$$

$0.2 < p_T < 2.9$ GeV/c

$$\frac{1}{2\pi p_T}\frac{d^2N}{dp_T dy} = 0.418898[c^2/\mathrm{GeV}^2] \cdot (1 + p_T/(3.5691[\mathrm{GeV}/c]))^{-7.63859} \quad (4.7)$$
$$+ 23.2689(p_T/(1[\mathrm{GeV}/c]))^{-8.0},$$

$2.9 < p_T < 25$ GeV/c.

The rapidity distribution of the π^0 was assumed to be flat, and was generated between $-0.5 < \eta < 0.5$. Figure 4.10 shows R_γ from π^0 decays as a function

of p_T. Photons come from decays of heavier hadrons as well. The value of R_γ from π^0 decays, $R_\gamma^{\pi^0}$, can be expressed as

$$R_\gamma^{\pi^0} = \frac{P_{\rm bp} + P_{\rm air} + P_{\rm Dalitz}^{\pi^0} + P_{\rm conv}}{P_{\rm bp} + P_{\rm air} + P_{\rm Dalitz}^{\pi^0}} \tag{4.8}$$

where $P_{\rm bp}$, $P_{\rm air}$, and $P_{\rm conv}$ are the probability for a photon to convert in the beampipe, in air, and in the converter in the PHENIX detector, respectively, and $P_{\rm Dalitz}^{\pi^0}$ is the internal conversion probability of π^0 Dalitz decays. $P_{\rm Dalitz}^{\pi^0}$ has a value of 0.598%. Similarly, R_γ^η can be expressed as

$$R_\gamma^\eta = \frac{P_{\rm bp} + P_{\rm air} + P_{\rm Dalitz}^{\eta} + P_{\rm conv}}{P_{\rm bp} + P_{\rm air} + P_{\rm Dalitz}^{\eta}} \tag{4.9}$$

with $P_{\rm Dalitz}^\eta$ having a value of 0.80%.

R_γ from π^0 and η combined, $R_\gamma^{\pi^0+\eta}$, is calculated by

$$R_\gamma^{\pi^0+\eta} = \frac{R_\gamma^{\pi^0} N_e^{\pi^0} + R_\gamma^\eta N_e^\eta}{N_e^{\pi^0} + N_e^\eta} = \frac{R_\gamma^{\pi^0} + R_\gamma^\eta \epsilon^{\eta/\pi^0}}{1 + \epsilon^{\eta/\pi^0}} \tag{4.10}$$

$$\epsilon^{\eta/\pi^0} \equiv N_e^\eta / N_e^{\pi^0} \tag{4.11}$$

where $N_e^{\pi^0}(N_e^\eta)$ is the electron yield as a result of $\pi^0(\eta)$ decays. Since the Dalitz branching ratio for η mesons is similar to that of heavier mesons (ω, η', ϕ, etc.), to take into account the contribution to R_γ by all hadrons other than the π^0, we simply replace in Equation 4.10 $R_\gamma^{\pi^0+\eta}$ with R_γ and N_e^η with $N_e^{\rm h}$, the yield of photonic electrons from decays of all hadrons heavier than the η. $N_e^{\rm h}$ is determined using the same machinery used in the cocktail.

4.3 Consistency of the Two Methods

If the non-photonic components to the cocktail, such as K_{e3} decay, are removed, then the remaining photonic electron yield from the cocktail should be consistent with the yield obtained by the converter method. Figure 4.11 shows the ratio of the photonic electron yield using the converter method to that of the cocktail method, for various centrality bins. For minimum-bias collisions, the converter yield is a factor of 1.182 times higher than the cocktail yield. At low p_T, the systematic error from the cocktail method is quite high, indeed, it is slightly larger than 18%. Because the converter method is more reliable than the cocktail method at low p_T, the photonic part of the cocktail is scaled by a factor of 1.182. Note that there is a clear centrality

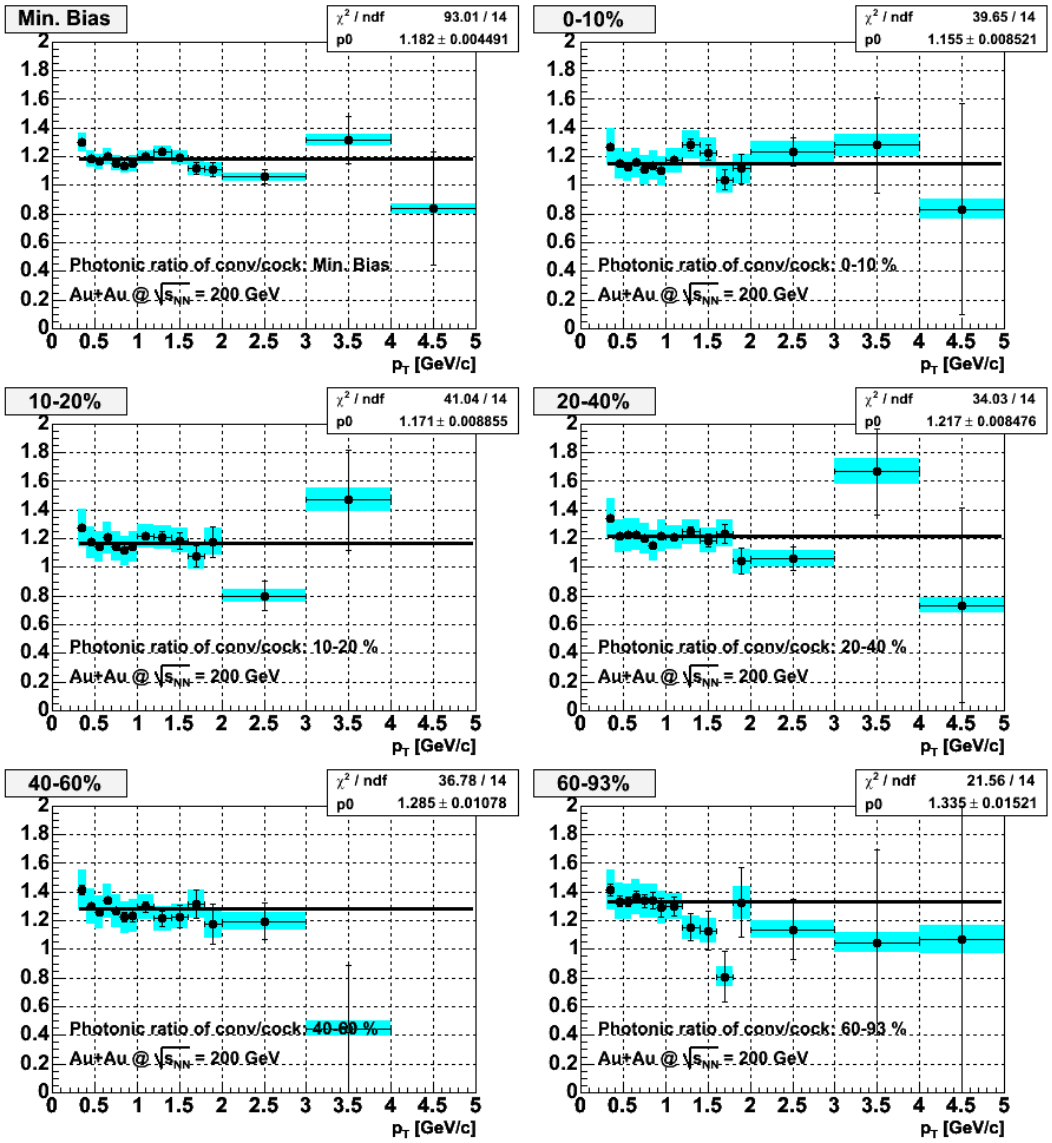

Figure 4.11: Ratio of photonic electron yield determined by the converter method to that determined by the cocktail method.

dependence in the converter to cocktail ratio. This centrality dependence is difficult to understand, and has not been seen in the analysis of p+p data, or in the RHIC Run-2 Au+Au analysis. One difference in this analysis is the discrepancy between the Run2 and Run4 neutral pion data. I tend to think that the centrality dependence of the converter to cocktail ratio comes from this discrepancy. Above p_T of 2 GeV/c, where the signal to background is high, this issue is of little importance. At low p_T, there is room for doubt about the total yield. It is difficult to assign a precise systematic uncertainty due to a discrepancy in measurements (as in the case of the neutral pion spectrum), as it is unclear whether one or both of the measurements is incorrect.

Since the converter method is more trustworthy at low p_T, it is used to perform the background subtraction below 1.6 GeV/c. At higher p_T, the statistics of the converter method are limited, and the cocktail method is used. This makes the problem of the centrality dependence of the converter to cocktail ratio not so important, so long as the cause of the problem is in the cocktail, because the converter method is a direct measurement of the photonic background.

4.4 Systematic Error for the Cocktail Method

Systematic errors are estimated for all cocktail ingredients, propagated to the corresponding electron spectra, and then added in quadrature to determine the total cocktail systematic error.

The following systematic errors are assigned to the various inputs and the resulting 1σ upper and lower systematic errors on the cocktail are shown in Fig. 4.12 for minimum bias collisions:

- pion spectrum (black curves in Fig. 4.12): obtained via full cocktail calculations using pion spectra moved up (down) by the systematic uncertainty of the pion spectrum as input (almost no p_T dependence). The additional systematic uncertainty due to the difference between Run-2 and Run-4 π^0 data is indicated in green.

- meson to pion ratios: the sys. uncertainties are listed above. Since the contributions from all other mesons are much smaller than the contribution from η decay (red curves in Fig. 4.12) the resulting systematic uncertainties are tiny (< 1 %) and, therefore, almost invisible as isolated curves in Fig. 4.12 (almost no p_T dependence).

- conversion material in the aperture (light blue curves in Fig. 4.12): 10 % systematic error (p_T independent)

centrality	$p0$	$p1$ $[(\mathrm{GeV/c})^{-1}]$	$p2$	$p3$ $[\mathrm{GeV/c}^{-1}]$	$p4$ $[(\mathrm{GeV/c}^{-1})^2]$	$p5$ $[(\mathrm{GeV/c}^{-1})^3]$
min. bias	18.23	-1.324	-5.257	9.956	-1.596	0.0787
0 - 10 %	17.91	-2.777	-0.311	9.298	-1.743	0.0959
10 - 20 %	13.79	-1.880	0.347	7.033	-1.265	0.0701
20 - 30 %	16.22	-1.888	-1.366	8.354	-1.462	0.0776
30 - 40 %	17.20	-1.507	-3.683	9.676	-1.698	0.0918
40 - 50 %	16.08	-1.435	-3.187	9.301	-1.572	0.0826
50 - 60 %	161.3	0.1817	-152.9	-30.8	-1.244	-0.388
60 - 70 %	17.36	-1.714	-2.993	10.20	-1.793	0.0977
70 - 80 %	193.6	0.1796	-184.0	-35.2	-1.888	-0.419
80 - 92 %	231.8	0.1865	-222.3	-43.0	-2.834	-0.520

Table 4.4: Fit parameters for the total cocktail systematic error according to Eq. 4.12.

- K_{e3} decay (green curves in Fig. 4.12): 50 % systematic error (relevant only at low p_T)
- direct radiation (blue curves in Fig. 4.12): obtained from the systematic error quoted for the direct photon measurement (only important towards higher p_T)

Since the 1σ upper and lower systematic uncertainties are symmetric as shown in Fig. 4.12, the total cocktail systematic error is calculated by adding the individual contributions in quadrature and averaging the upper and lower uncertainties. The resulting total systematic error is indicated by the data points in Fig. 4.12 together with a fit according to the parameterization:

$$\mathrm{sys.error}[\%] = p0 \times exp(p1 \times p_T) + p2 + p3 \times p_T + p4 \times p_T^2 + p5 \times p_T^3 \quad (4.12)$$

The fit parameters are summarized for all centralities in Tab. 4.4.

When the cocktail is rescaled to the photonic electron spectrum as measured via the converter technique at low p_T, only the uncertainty in the shape of the cocktail relative to the normalization at low p_T is relevant in addition to the uncertainty in the rescaling factor. To evaluate the shape uncertainty, in a first step the systematic error from the material budget is removed from the error calculation since it is p_T independent, and the systematic errors from the meson to pion ratios are (conservatively) reduced by 50 % since these are (almost) p_T independent in the relevant p_T range below 4 GeV/c.. Then it is important to note that the cocktail systematic errors are not point to point

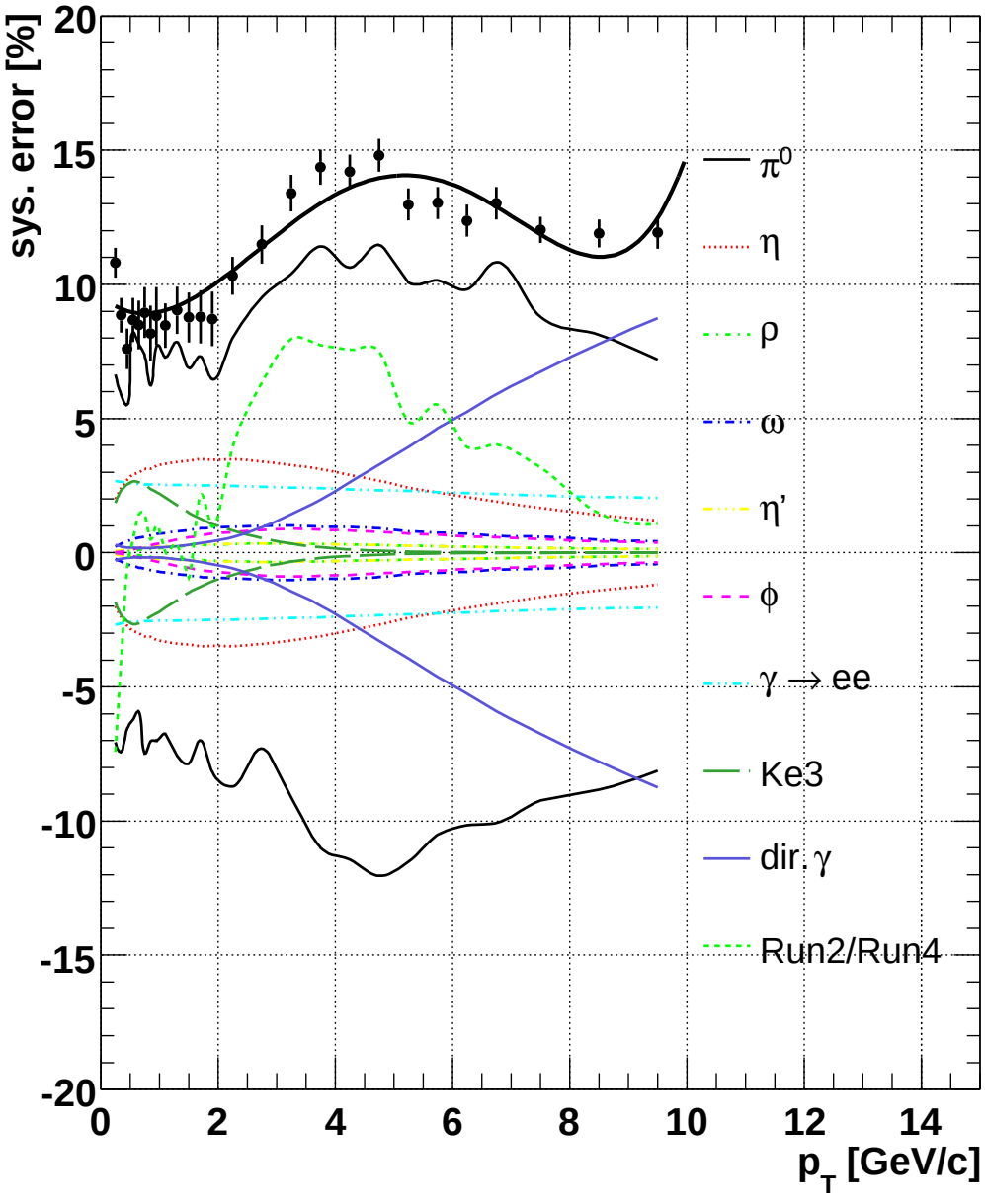

Figure 4.12: Individual contributions to the cocktail systematic error for minimum bias collisions. The total error is depicted by the data points which are shown together with a fit.

centrality	$p0$	$p1$ [(GeV/c)$^{-1}$]	$p2$	$p3$ [GeV/c^{-1}]	$p4$ [(GeV/c^{-1})^2]	$p5$ [(GeV/c^{-1})^3]	$p6$
min. bias	20.0	-1.34	-7.17	10.6	-1.68	0.082	7.05
0 - 10 %	19.6	-2.78	-1.74	9.74	-1.81	0.099	7.00
10 - 20 %	15.5	-1.84	-1.45	7.59	-1.34	0.074	7.30
20 - 30 %	17.9	-1.90	-2.97	8.82	-1.53	0.081	7.00
30 - 40 %	18.9	-1.52	-5.46	10.2	-1.78	0.096	7.15
40 - 50 %	17.6	-1.46	-4.78	9.77	-1.64	0.086	7.45
50 - 60 %	21.1	-1.48	-8.57	11.4	-1.96	0.108	5.70
60 - 70 %	18.6	-1.76	-4.22	10.5	-1.84	0.100	7.60
70 - 80 %	20.3	-1.53	-6.51	12.6	-2.35	0.136	8.10
80 - 92 %	78.6	-0.64	-66.7	41.0	-7.11	0.410	8.85

Table 4.5: Fit parameters for the shape only cocktail systematic error according to Eq. 4.12.

errors but are highly correlated as a function of p_T. Therefore, the difference between the systematic error at a given p_T and the one at low p_T (here: 2 GeV/c) is a good measure for the systematic error of the cocktail shape relative to the normalization point at 2 GeV/c. The parameterization chosen to fit the shape systematic error is:

$$SE_{\text{shape}}(p_T)[\%] = \sqrt{|(p_0 e^{p_1 p_T} + p_2 + p_3 p_T + p_4 p_T^2 + p_5 p_T^3)^2 - p_6^2|} \qquad (4.13)$$

The resulting fit parameters for all centrality classes are summarized in Tab. 4.5

4.5 Systematic Error for the Converter Method

To study the systematic error in the estimation of the photonic electron background using the converter method, e^+e^- pairs from conversions in the beampipe (or converter) were extracted using the method outlined in Section 3.5.2. The apparent mass of conversion pairs from the converter will be about the same as that for conversions from the beampipe, because the converter is wrapped just around the beampipe. Figure 4.13 shows the p_T distribution of e^+e^- pairs with a mass cut of 0.000 - 0.035 [GeV/c^2]. The ratio of the number of electrons from conversions with the converter installed to without the converter installed is within 4% of that obtained by the π^0 simulation method, and this difference was assigned to the systematic error for the photonic background using the converter method. An additional 1% uncertainty

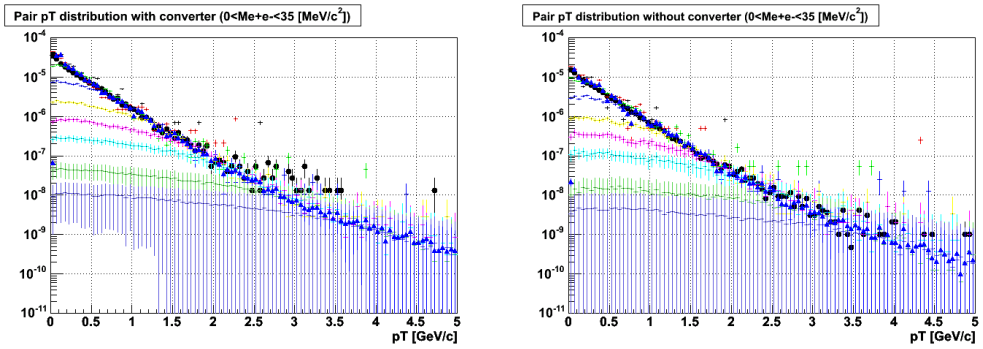

Figure 4.13: The ${p_T}^{e^+e^-}$ distribution of conversion e^+e^- pair (0.000 - 0.035 [GeV/c^2]) in real data (MB) and simulation. Left: with converter installed. Right: with converter removed.

was added to take into account energy loss of electrons as they pass through the converter.

4.6 Cocktail Calculation with Respect to the Reaction Plane

To generate the v_2 of electrons from photonic sources, the same basic method was used as in the cocktail calculation outlined above. The difference is that the input p_T distribution of pions, which subsequently decay into two photons (or Dalitz decay) was modulated as a function of angle with respect to the reaction plane by the v_2 of hadrons as measured by PHENIX [65, 66, 67]. Note from [67] that v_2 of pions and kaons are identical as a function of the transverse kinetic energy. This result, which is predicted by hydrodynamic calculations, is used for the input v_2 for eta mesons in the cocktail calculation. The resulting photonic electron spectra were divided into 12 bins in angle from the reaction plane, and fits were made for each p_T to determine the photonic electron v_2. The v_2 of sources other than decays of pions, eta, etc., such as direct photons, was assumed to be negligible. Since overall normalization does not affect the value of v_2, the relative systematic error on the photonic electron v_2 from the normalization was ignored. However, the error due to the relative admixture of various photonic sources was found to give an error of about 4% on the photonic electron v_2. The statistical error on the photonic electron v_2 is non-zero due to the finite statistics generated by the simulation (100 million events per centrality). The statistical error is p_T independent since the

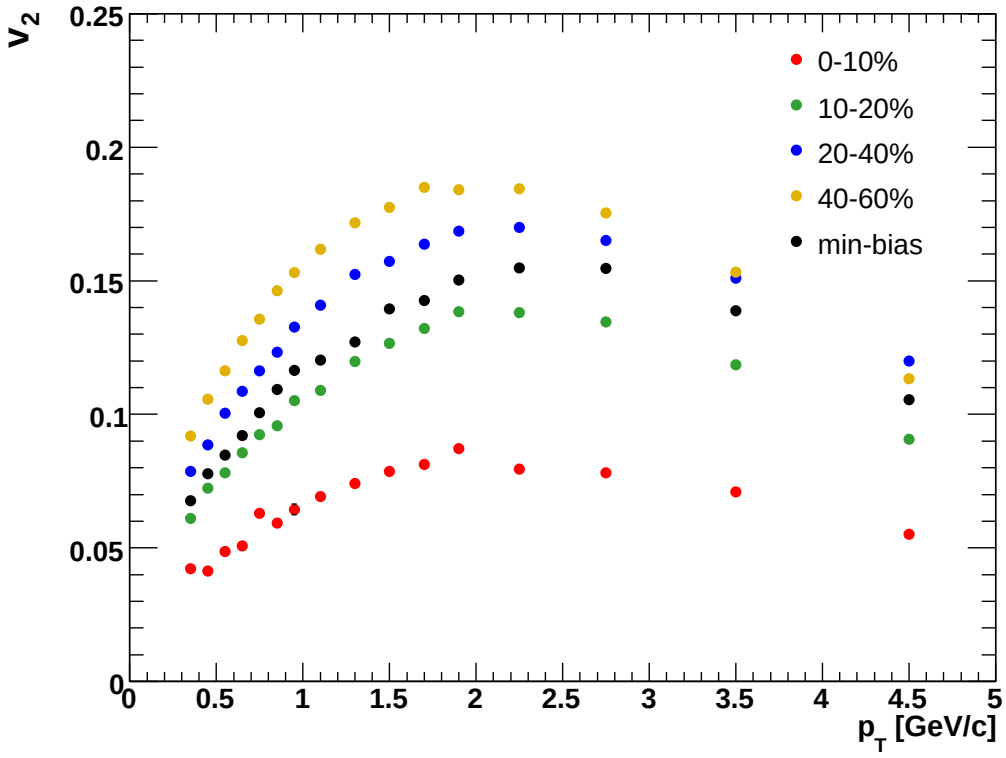

Figure 4.14: v_2 of electrons originating from sources other than heavy flavor decays from the cocktail calculation for various centralities.

simulation generates input particles with a flat p_T distribution.

The pion v_2 measurement at PHENIX was done for 10% centrality bins up to 60% centrality, and also for minimum-bias collisions (0-93%). As there was no measurement of the 60-93% centrality v_2, we do not make a cocktail estimation of the photonic electron v_2 in that centrality range. In principle, with the minimum bias measurement and the 0-60% measurement, one could extract the the 60-93% v_2. However, the yield in the peripheral bin is very small compared to the total yield, and thus error in the minimum-bias v_2 propagated is highly amplified in the peripheral bin. As such, a direct measurement of the v_2 for pions in the 60-93% centrality bin is required for extraction of the heavy flavor electron v_2 in that bin.

Chapter 5

Results and Discussion

5.1 Experimental Results

5.1.1 Invariant Yield of Electrons from Heavy Flavor Decays

The invariant yield of electrons from heavy flavor decays is obtained by subtracting the photonic yield estimated by the cocktail (scaled to match th converter data) from the measured invariant yield of inclusive electrons, as a function of p_T and centrality. Systematic errors are calculated by adding in quadrature the systematic error on the inclusive yield with the systematic error on the cocktail estimation. The statistical error on the heavy flavor electron yield is taken to be the statistical error on the inclusive yield, as the cocktail statistical errors are negligible. At low p_T, where the signal to background level is small, the relative error in the heavy flavor yield is enhanced by the background subtraction. Figure 5.1 shows the invariant heavy flavor electron yield for various Au+Au centrality bins and p+p collisions, compared to FONLL [68] fits to the p+p cross section [64] scaled by the nuclear overlap integral $\langle T_{AA} \rangle$ [69]. Suppression at high p_T in the 0-10% centrality bin relative to the fit to the binary-scaled p+p spectrum can be clearly seen from Figure 5.1. To get a better view of the suppression, we calculate the ratio of the spectra to the curves in Figure 5.1.

5.1.2 Nuclear Modification Factor R_{AA}

Recall the definition of the nuclear modification factor

$$R_{AA} \equiv \frac{dN_{AA}}{T_{AA} \times d\sigma_{pp}} = \frac{dN_{AA}}{\langle N_{coll} \rangle \times dN_{pp}}. \tag{5.1}$$

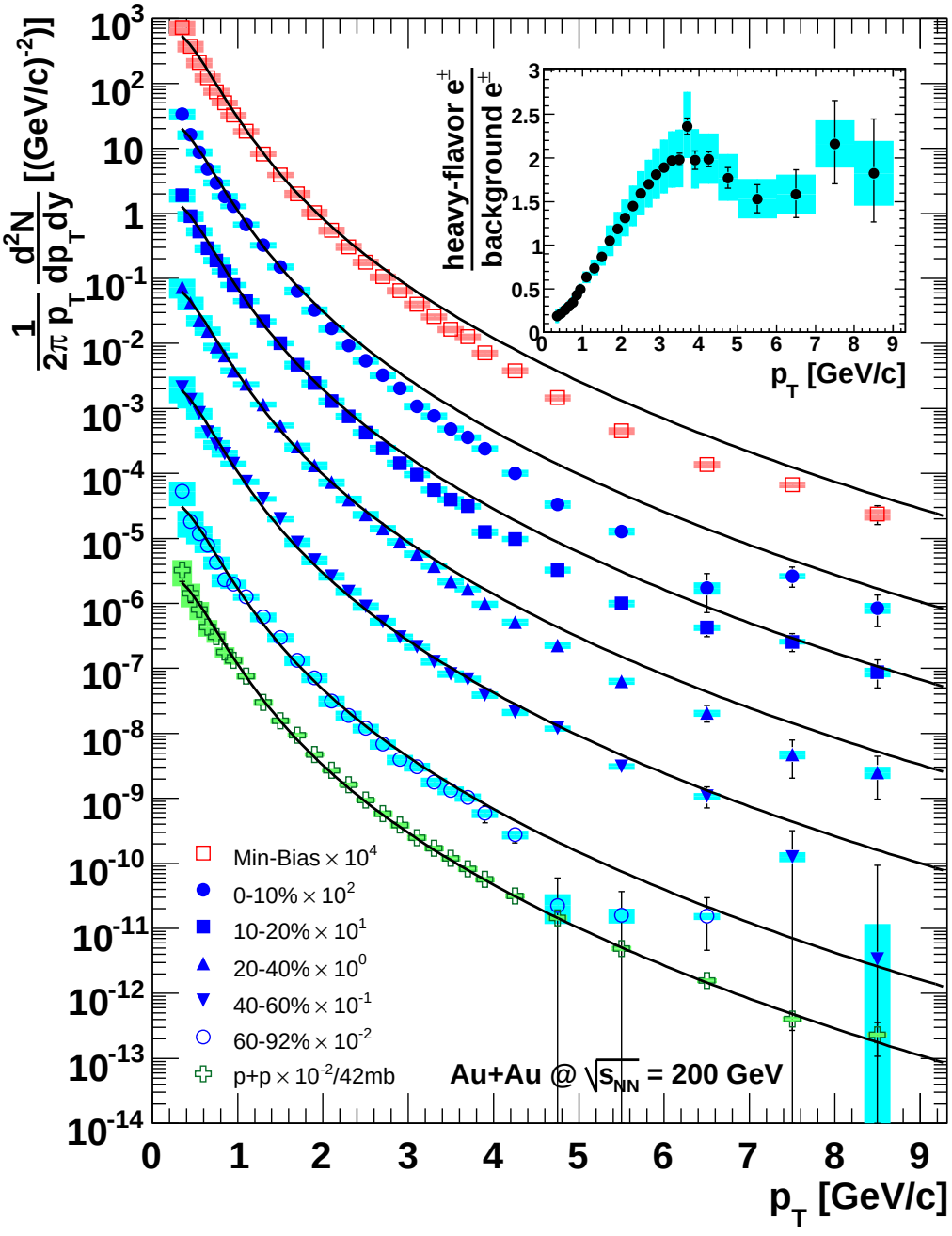

Figure 5.1: Invariant yield of $\frac{e^+ + e^-}{2}$ from decays of heavy flavor hadrons. The yields for various centrality bins have been scaled by powers of 10 for clarity. The curves shown are fixed-order-plus-next-to-leading-log calculations [68] of the p+p cross section, scaled by the nuclear overlap integral [69]. Also shown is the invariant yield from p+p collisions [64].

Below p_T of 1.6 GeV/c, the R_{AA} was obtained by dividing by the T_{AA}-scaled p+p heavy flavor electron spectra point-by-point. Statistical and systematic error, with the exception of the systematic error from the π^0 simulation for the increase in electrons due to the installation of the converter, was propagated by adding in quadrature the change in R_{AA} by moving changing the p+p spectra by one standard deviation, to the change in R_{AA} by changing the Au+Au spectra by one standard deviation. The error from the π^0 simulation should be correlated between p+p and Au+Au since the same simulation was used for both analyses. The latter error was calculated by simultaneously moving the Au+Au and p+p spectra up and down by the error due to the π^0 simulation, and was added in quadrature to the remaining systematic error.

For p_T greater than 1.6 GeV/c, the p+p spectral shape is consistent with a FONLL calculation [64] (see Figure 5.1). For this range in p_T, the R_{AA} was obtained by dividing the Au+Au spectra by the scaled FONLL fit to the p+p spectra. Statistical error on the fit was considered as a systematic error on the normalization in the denominator for R_{AA}. Figures 5.2 - 5.7 (a) show the R_{AA} as a function of p_T for various collision centralities. There is evidence for suppression of high-p_T heavy flavor electrons relative to p+p across all centrality bins in Au+Au collisions. For the most central collisions, there is noticable suppression above p_T of 2 GeV/c. It is interesting to note that the R_{AA} for heavy flavor electrons is equal within errors to the R_{AA} for neutral pions above p_T of 5 GeV/c, though for lower p_T the electron R_{AA} falls more slowly than does the pion R_{AA}. Figure 5.8 shows the R_{AA} as a function of the number of participating nucleons in a collision (collision centrality). The total charm production above 0.3 GeV/c can be seen to be consistent with binary scaling, though the errors at low p_T are rather large.

5.1.3 Azimuthal anisotropy parameter v_2

The azimuthal anisotropy parameter v_2 for heavy flavor electrons is shown in Figures 5.2 - 5.7 (b), for the same centralities as the R_{AA} save for the 60-93% centrality bin. To extract the heavy flavor electron v_2, recall Equation 1.3

$$\frac{dN}{d(\phi - \Psi)} = N_0(1 + 2v_2\cos(2(\phi - \Psi))).$$

The inclusive electron azimuthal distribution can be expressed in terms of the heavy flavor electron and photonic electron distributions as

$$\frac{dN_{\rm inc}}{d(\phi - \Psi)} = \frac{dN_{\rm hf}}{d(\phi - \Psi)} + \frac{dN_{\rm pho}}{d(\phi - \Psi)} \tag{5.2}$$

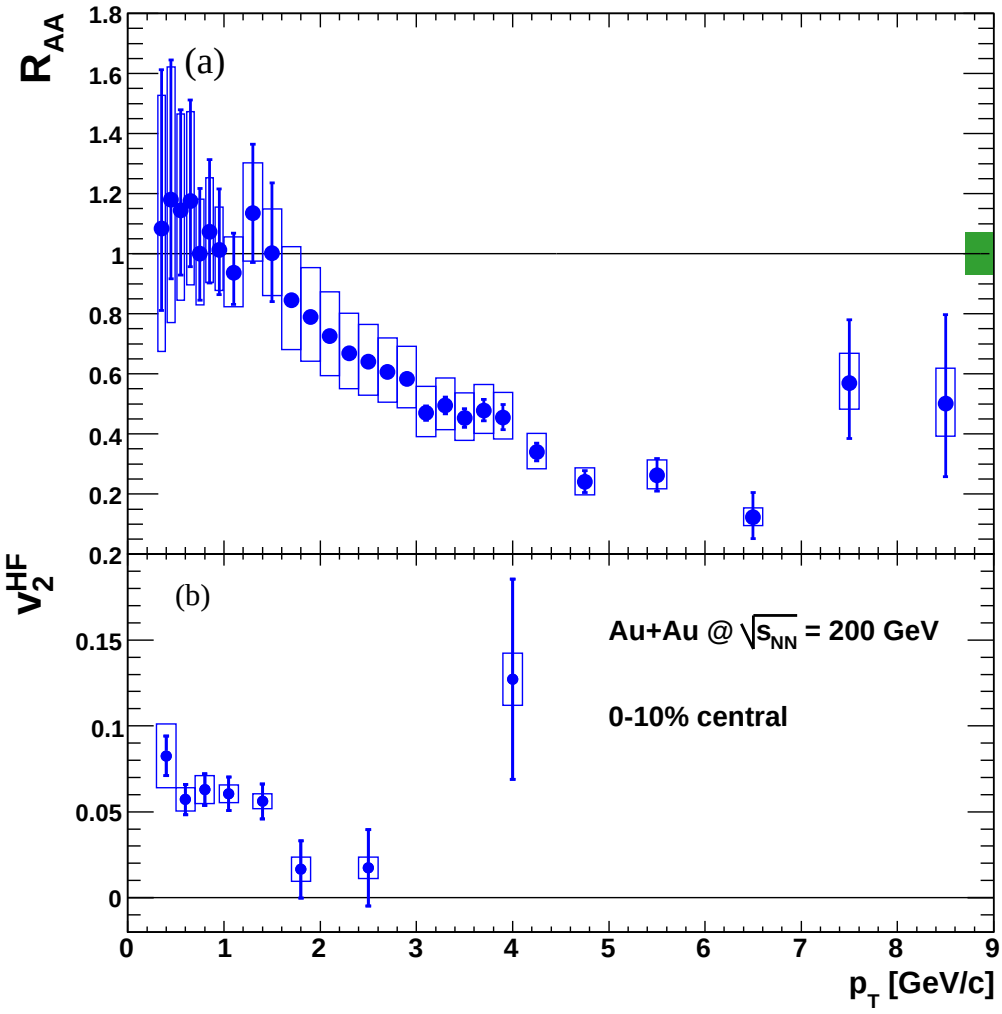

Figure 5.2: Nuclear modification factor R_{AA} (a) and azimuthal anisotropy parameter v_2 (b) as a function of p_T for 0-10% centrality. Boxes represent systematic errors, and lines represent statistical errors. The shaded band on the right represents a scaling error due to error in T_{AA}.

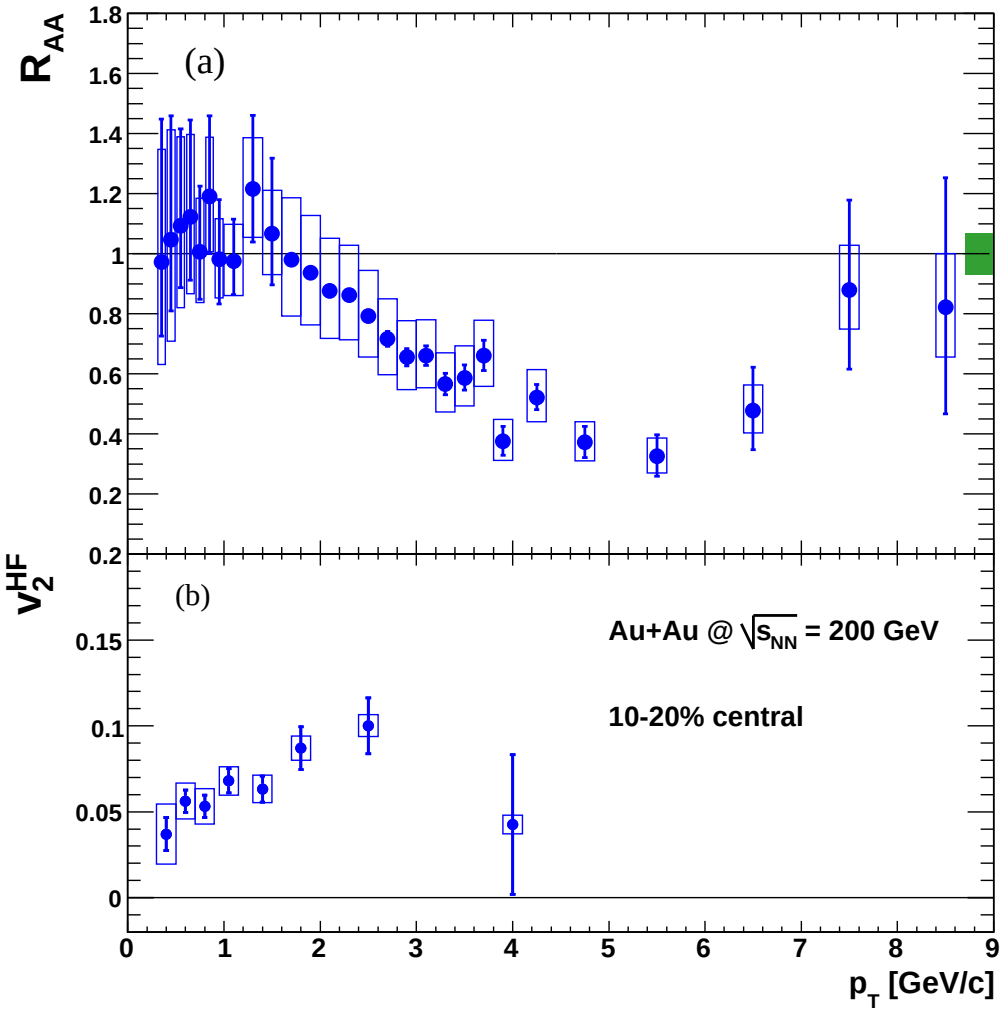

Figure 5.3: Nuclear modification factor R_{AA} (a) and azimuthal anisotropy parameter v_2 (b) as a function of p_T for 10-20% centrality. Boxes represent systematic errors, and lines represent statistical errors. The shaded band on the right represents a scaling error due to error in T_{AA}.

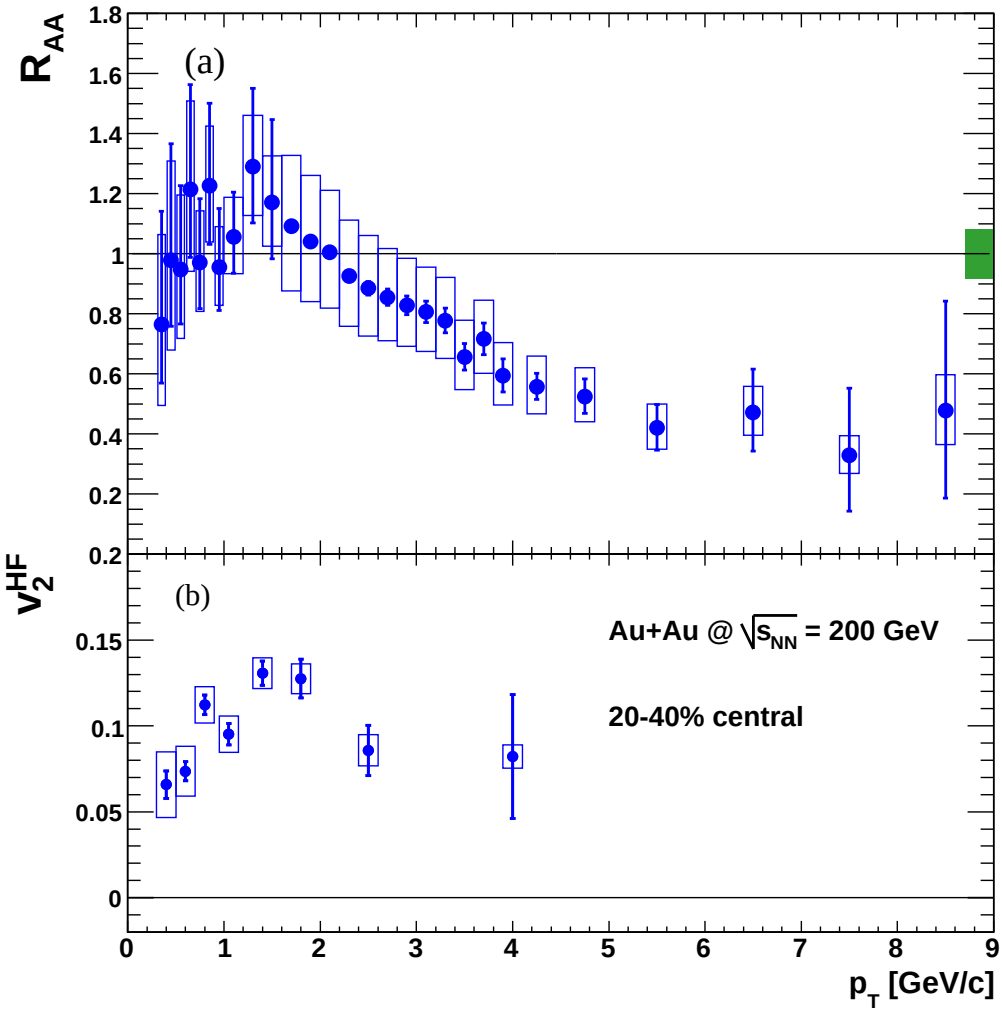

Figure 5.4: Nuclear modification factor R_{AA} (a) and azimuthal anisotropy parameter v_2 (b) as a function of p_T for 20-40% centrality. Boxes represent systematic errors, and lines represent statistical errors. The shaded band on the right represents a scaling error due to error in T_{AA}.

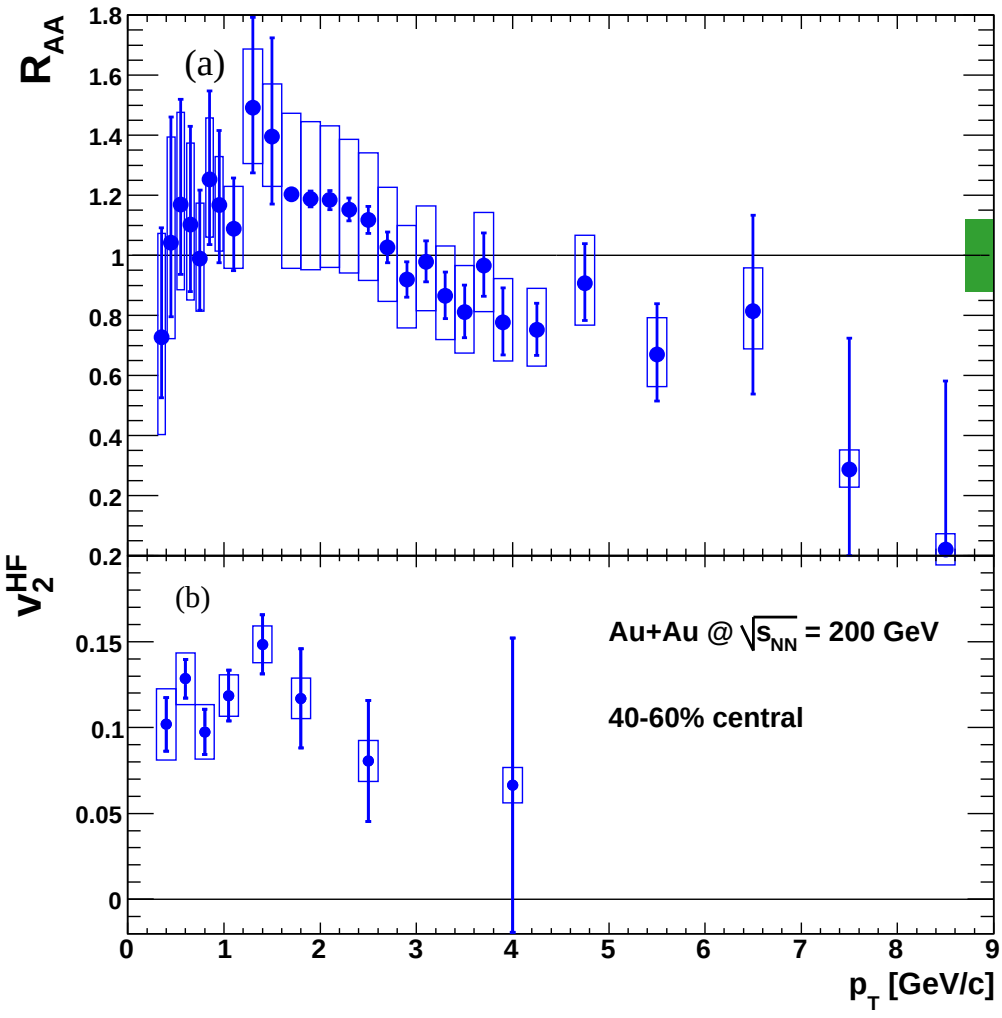

Figure 5.5: Nuclear modification factor R_{AA} (a) and azimuthal anisotropy parameter v_2 (b) as a function of p_T for 40-60% centrality.

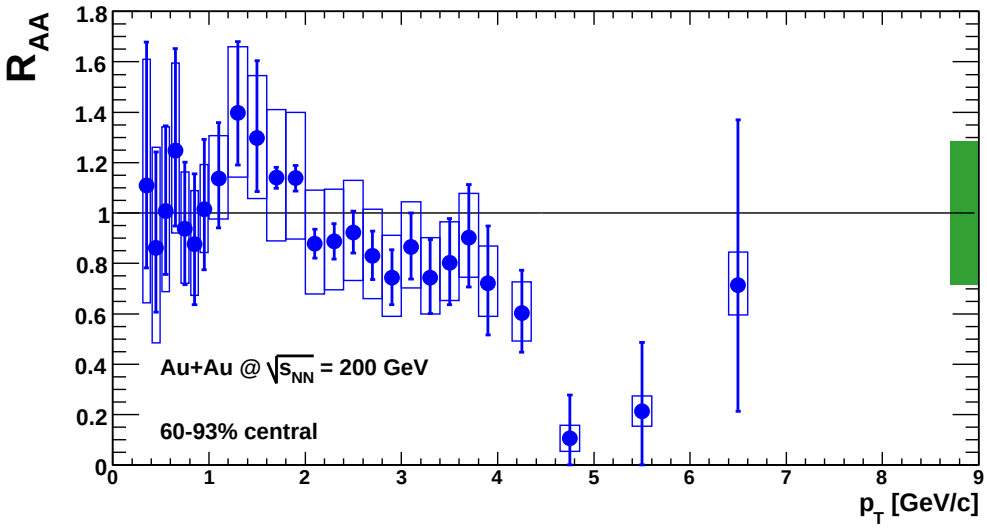

Figure 5.6: Nuclear modification factor R_{AA} as a function of p_T for 60-93% centrality. Boxes represent systematic errors, and lines represent statistical errors. The shaded band on the right represents a scaling error due to error in T_{AA}.

which can also be expressed as

$$N_0^{\rm inc}\Big(1+2v_2^{\rm inc}\cos\left(2\left(\phi-\Psi\right)\right)\Big) = \tag{5.3}$$
$$N_0^{\rm hf}\Big(1+2v_2^{\rm hf}\cos\left(2\left(\phi-\Psi\right)\right)\Big)+N_0^{\rm pho}\Big(1+2v_2^{\rm pho}\cos\left(2\left(\phi-\Psi\right)\right)\Big)$$

which then implies

$$v_2^{\rm hf}=\frac{v_2^{\rm inc}\left(N_0^{\rm hf}+N_0^{\rm pho}\right)-v_2^{\rm pho}N_0^{\rm pho}}{N_0^{\rm hf}} \tag{5.4}$$

since $N_0^{\rm inc}=N_0^{\rm hf}+N_0^{\rm pho}$. In terms of the signal to background ratio

$$S\equiv\frac{N_0^{\rm hf}}{N_0^{\rm pho}} \tag{5.5}$$

Equation 5.4 can be expressed as

$$v_2^{\rm hf}=v_2^{\rm inc}\left(1+\frac{1}{S}\right)-\frac{v_2^{\rm pho}}{S}. \tag{5.6}$$

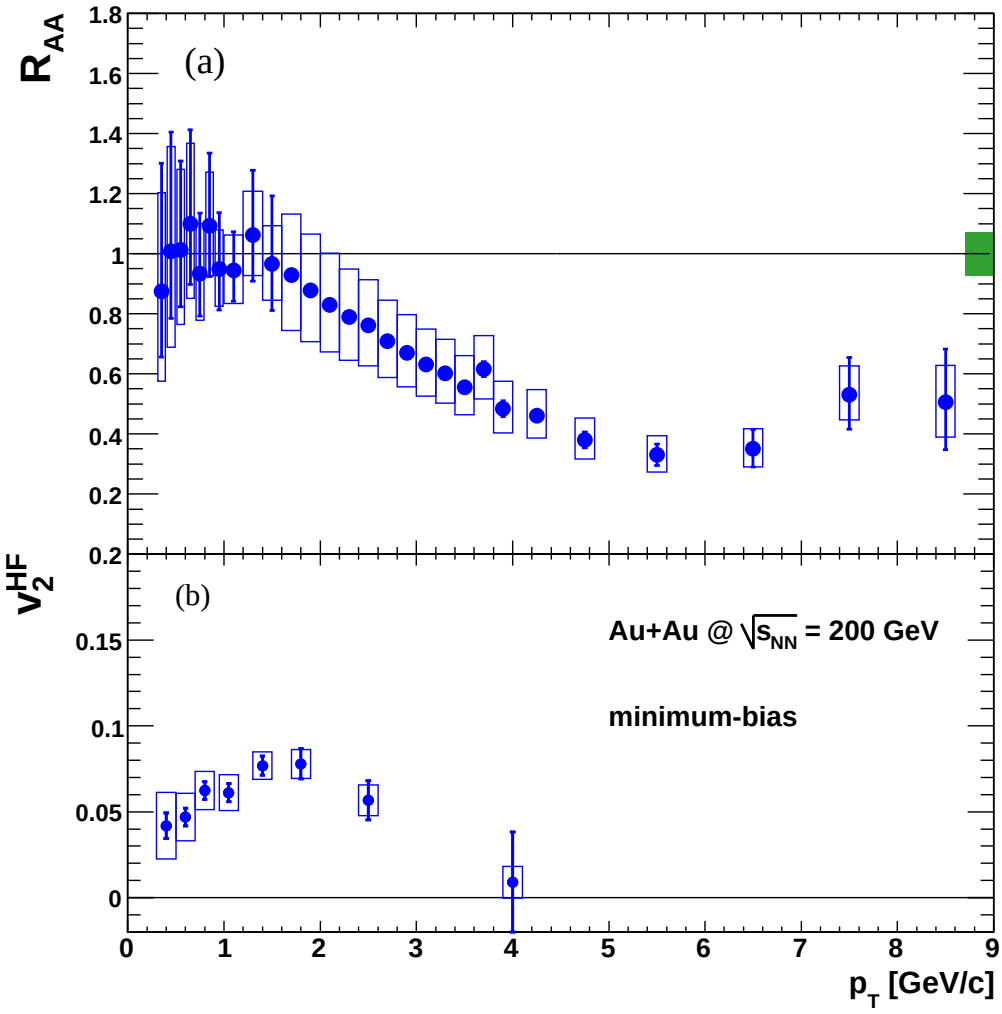

Figure 5.7: Nuclear modification factor R_{AA} (a) and azimuthal anisotropy parameter v_2 (b) as a function of p_T for minimum-bias collisions. Boxes represent systematic errors, and lines represent statistical errors. The shaded band on the right represents a scaling error due to error in T_{AA}.

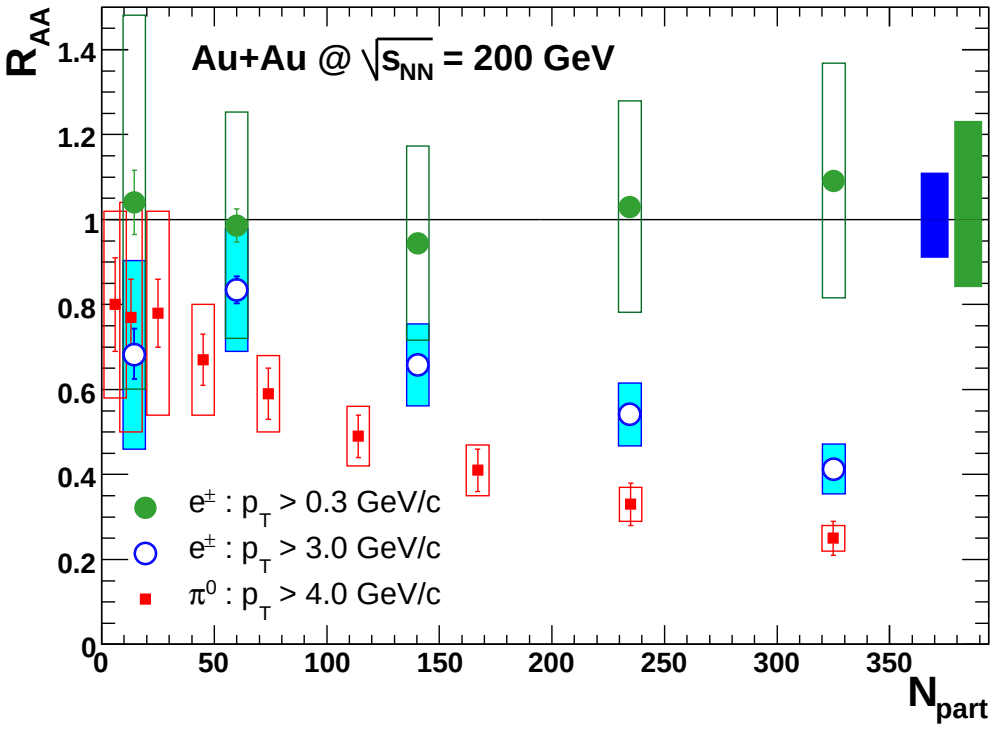

Figure 5.8: Nuclear modification factor R_{AA} as a function of the number of participating nucleons in the collision for electrons integrated above 0.3 GeV/c, and above 3.0 GeV/c. Also shown in the π^0 R_{AA} integrated of 4.0 GeV/c. The bands on the right represent systematic errors due to the p+p reference spectrum.

The error on $v_2^{\rm hf}$ is propagated as

$$\left(\Delta v_2^{\rm hf}\right)^2 = \left(\Delta v_2^{\rm inc}\right)^2 + \left(\frac{1}{S}\right)^2 \left(\Delta\left(v_2^{\rm inc} - v_2^{\rm pho}\right)\right)^2 + \left(\frac{1}{S}\right)^4 (\Delta S)^2 \left(v_2^{\rm inc} - v_2^{\rm pho}\right)^2. \tag{5.7}$$

The determination of the error in the second term in Equation 5.7 depends on the source of the error. Both the inclusive and photonic v_2 have error due to the determination of the reaction plane resolution. But the reaction plane is determined independently of what is measured in the central arm detectors. So for the error due to the reaction plane resolution the error in the second term is determined as

$$\Delta\left(v_2^{\rm inc} - v_2^{\rm pho}\right) = \Delta v_2^{\rm inc} - \Delta v_2^{\rm pho}. \tag{5.8}$$

For the remaining uncorrelated systematic error we have

$$\left(\Delta\left(v_2^{\rm inc} - v_2^{\rm pho}\right)\right)^2 = \left(\Delta v_2^{\rm inc}\right)^2 + \left(\Delta v_2^{\rm pho}\right)^2. \tag{5.9}$$

The correlated and uncorrelated systematic errors are then added in quadrature.

The increase in the anisotropy parameter v_2 for more peripheral collisions corresponds to the greater initial spatial anisotropy in the more peripheral collisions. The centrality dependence of the v_2 of electrons from heavy flavor decays is similar to that of the light hadrons [67]. This is evidence that charm quarks do indeed flow at RHIC. Comparison of v_2 and R_{AA} of heavy flavor electrons to various model calculations will be shown in the next sections.

5.2 Comparison to Theory

In this section, calculations from various theoretical models for the interaction of heavy quarks in the medium are compared to the heavy flavor electron R_{AA} and v_2.

5.2.1 Energy-Loss Based Models

In the first chapter, two models to calculate radiative energy loss, called DGLV and BDMPS, were briefly described, and the calculations based on these models were compared to PHENIX data from RHIC Run 2. Figure 5.9 shows the DGLV energy loss calculation with and without elastic scattering [33] compared to the R_{AA} of electrons from heavy flavor from 0-10% central Au+Au

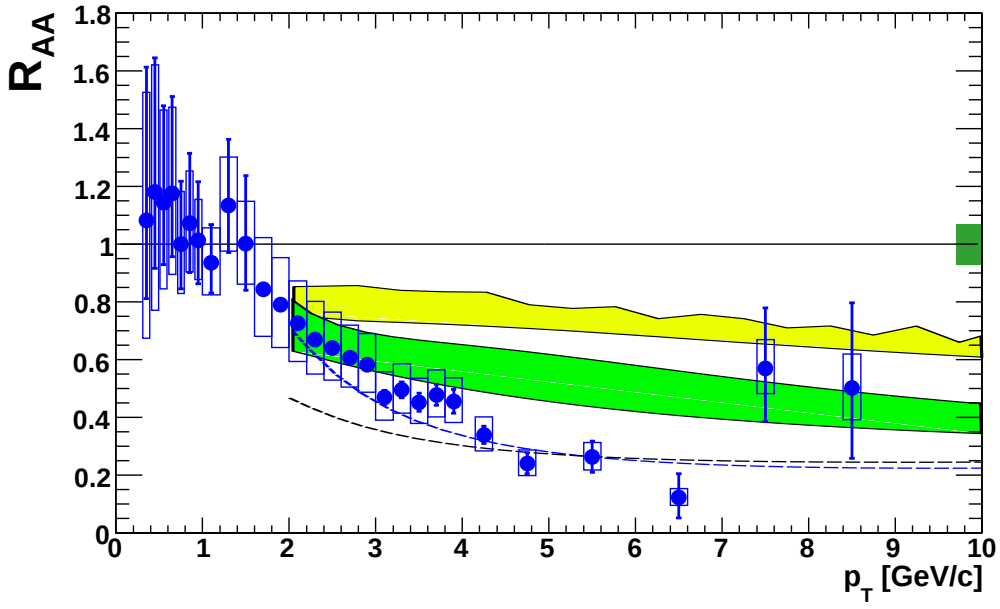

Figure 5.9: Nuclear modification factor R_{AA} for electrons from heavy flavor decays for 0-10% centrality, compared to the DGLV radiative energy loss calculations [33]. The upper and middle bands correspond R_{AA} for electrons from B and D decays. The middle band includes elastic energy loss as well as radiative energy loss. The dashed curves are calculations for R_{AA} for electrons from D decays only.

collisions determined in this analysis. The bands in Figure 5.9 are calculations of the R_{AA} of electrons from both B and D mesons. The dashed lines in the figure are calculations for D meson decays only. While the model underestimates the suppression of heavy flavor electrons, the data agree with the model for electrons from D meson decays. No measurement for the relative admixture of D and B mesons has been made at RHIC. The DGLV calculation uses a FONLL prediction for the D/B ratio. As seen in [64], a perturbative FONLL calculation agrees with the heavy flavor electron spectrum from p+p collisions. Reference [33] notes that this discrepancy points to missing perturbative QCD physics, incomplete understanding over initial heavy quark production, and/or novel perturbative mechanisms affecting partonic physics out to $p_T > 10$ GeV/c. This discrepancy will likely be unresolved at least until measurements of the D/B ratio can be made.

Comparison of the 0-10% R_{AA} to the BDMPS model [32] can be seen in Figure 5.10. This model too underpredicts the high p_T heavy flavor suppres-

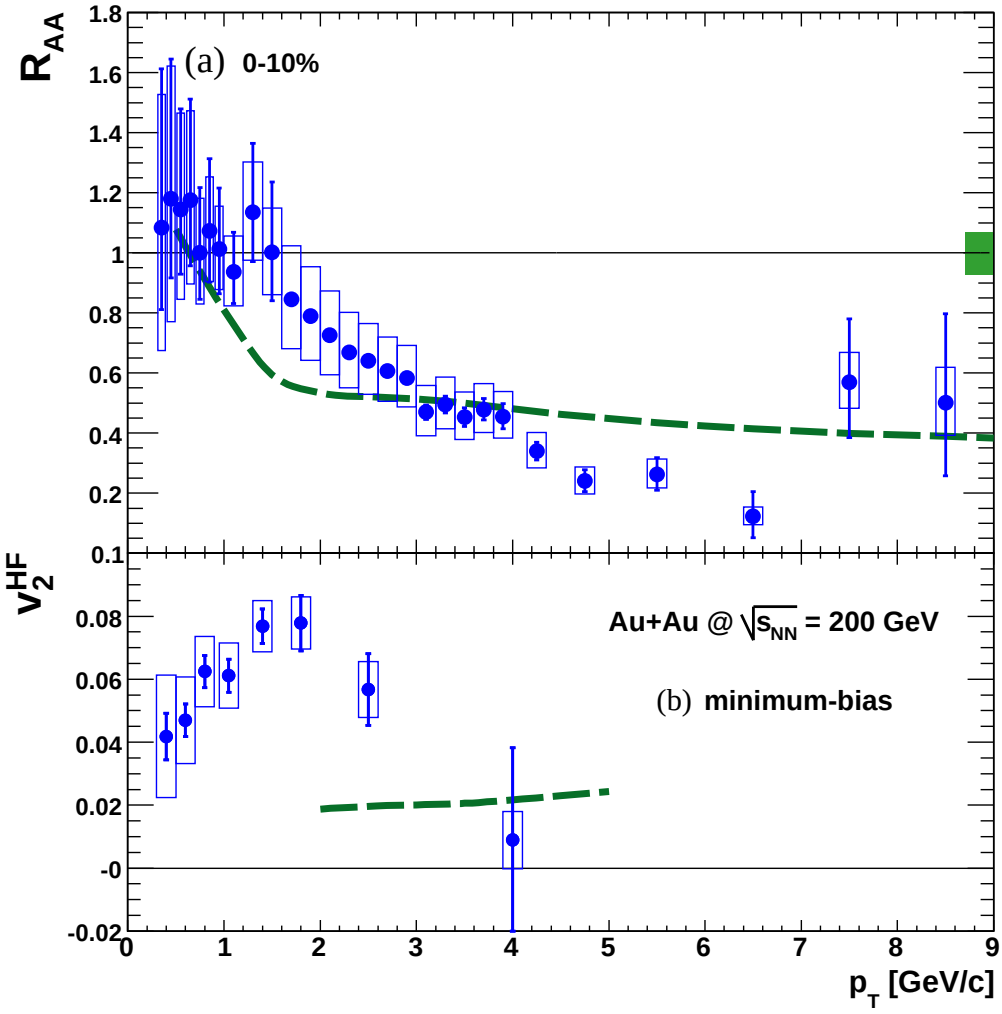

Figure 5.10: Nuclear modification factor R_{AA} for electrons from heavy flavor decays for 0-10% centrality, and azimuthal anisotropy parameter v_2 for minimum-bias collisions, compared to the BDMPS radiative energy loss calculations [32] with $\hat{q} = 14$ GeV^2/fm.

sion. The BDMPS model is also sensitive to the D/B ratio. Unlike DGLV, the BDMPS R_{AA} saturates for transport coefficient $\hat{q}$ greater than about 20 GeV^2/fm. So for the BDMPS model, increasing the density in the medium much more would not change R_{AA}, as heavy mesons emmitted from the surface of the medium are not suppressed. In light of this difference between the models, perhaps a good way to distinguish the BDMPS model from the DGLV model would be to look at the centrality dependence of the R_{AA}. Hopefully in the near future such calculations will be made. Nevertheless, it remains that radiative energy loss models do not describe the data well given that pQCD predicts the D/B admixture reasonably well.

The v_2 of heavy flavor electrons is also calculated in the BDMPS model, as shown as the dashed curve in Figure 5.12. Gluon bremstrahlung radiation gives rise to a positive v_2 since a quark moving perpendicular to the reaction plane traverses more material than a quark moving in-plane, and thus has a greater chance of radiating a gluon, which changes the direction of the quark. Unfortunately, the data at high p_T, where this effect might be dominant, has too great an uncertainty to favor any particular model. However, the data point between 2 and 3 GeV/c gives pretty convincing evidence that energy loss alone does not describe the azimuthal anisotropy of heavy quarks, though such an effect might still be an important contributor.

5.2.2 Hydrodynamical Models

The v_2 of light hadrons at low p_T agrees very well with predictions from hydrodynamical calculations [25], though at higher p_T one perhaps needs to take into account viscous corrections. It has recently been pointed out that the eccentricity of the produced medium may be underestimated due to fluctuations in the nucleon positions in the colliding nuclei [72], in which case hydrodynamical calculations overpredict the v_2, though a model based on slightly incomplete thermalization still works well to describe the anisotropy [73]. The v_2 of the heavy quark electron spectrum can provide an additional constraint on the evolving picture of the medium as a fluid. In addition, if the medium does indeed thermalize, the charm quark v_2 should be sensitive to the thermalization time. It should take multiple scatterings to push a charm quark along with the medium. That is, the charm quark relaxation time is expected to be higher that of light quarks, and since the pressure gradient is strongest in the early stages of the collision, the predicted charm quark v_2 in hydrodynamical models depends on when the charm quark begins to flow.

Recently, it has been shown that a Langevin-based heavy quark transport calculation by Moore and Teaney [42] can, at least qualitatively, explain a large suppression and azimuthal anisotropy of electrons from heavy flavor de-

cays. The model places a heavy quark into a thermal medium, and assumes that the interaction of the heavy quark with the medium can be described by uncorrelated momentum kicks. Contrary to the models described above, the interaction in the Langevin model is given exclusively by elastic collisions, which is a good approximation for quarks which are not ultrarelativistic in the center of mass frame of the collision. The parameter which is tuned in this model is the heavy quark diffusion coefficient. Figure 5.11 shows the 0-10% R_{AA} and the minimum-bias v_2 compared to the Langevin calculations for heavy quark diffusion coefficient values of $D_{\mathrm{HQ}} = 3/2\pi T$ and $D_{\mathrm{HQ}} = 12/2\pi T$.

While the above Langevin model fails to simultaneously describe R_{AA} and v_2 for a single value of the diffusion coefficient, another Langevin-based model [46] is in good agreement with both the suppression and anisotropy. In this model, the elastic scattering is mediated by resonance excitation of D and B-like states in the medium. The theoretical evidence for the existence of such resonance states comes from lattice computations. The bands in Figure 5.11 show the calculations of this model for R_{AA} and v_2. The width of the band corresponds to various values of the resonance scattering width. The resonance scattering reduces the relaxation time of the heavy quark in the medium, allowing the quark to flow with the medium earlier and thus increasing v_2. If gluon radiation would be taken into account, perhaps the prediction for R_{AA} would be in better agreement with the data above p_T of 5 GeV/c. This model gives a value of $D_{\mathrm{HQ}} \times 2\pi T$ between 4 and 6.

One result from [42] is that $D_{\mathrm{HQ}} \sim 6 \times \eta/(\epsilon + p)$, where η is the viscosity of the medium and $\epsilon + p$ is the enthalpy. Using the relation that $\epsilon + p = Ts$ at $\mu_B = 0$, with s the entropy, we get an estimate for the viscosity to entropy ratio η/s between $\frac{4}{3}/4\pi$ and $2/4\pi$. This estimate for η/s is close to the conjectured quantum bound of $1/4\pi$ obtained using the anti-de Sitter/conformal-field-theory (AdS/CFT) correspondence [47, 48]. The AdS/CFT correspondence exploits a duality between strongly coupled gauge theories and semiclassical gravitational physics to obtain predictions for gauge theories in the infinite-coupling limit. While such a theory is not equivalent to QCD, it may give a good way to obtain qualitative features of QCD which can be further explored by other methods. The AdS/CFT method has also been applied to estimate $\hat{q}$ [49] and D_{HQ} [50, 51, 52]. If there really is a quantum limit for η/s of $1/4\pi$, then there is evidence that the medium produced at RHIC is near a perfect fluid.

Figure 5.12 shows a comparison of a hydrodynamical model [41] with the minimum-bias heavy flavor electron v_2, given that the charm quark itself has a v_2 equal to that of light quarks (upper solid curve), and given that the charm quark v_2 is zero. At low p_T, the electron v_2 agrees well with the case that the

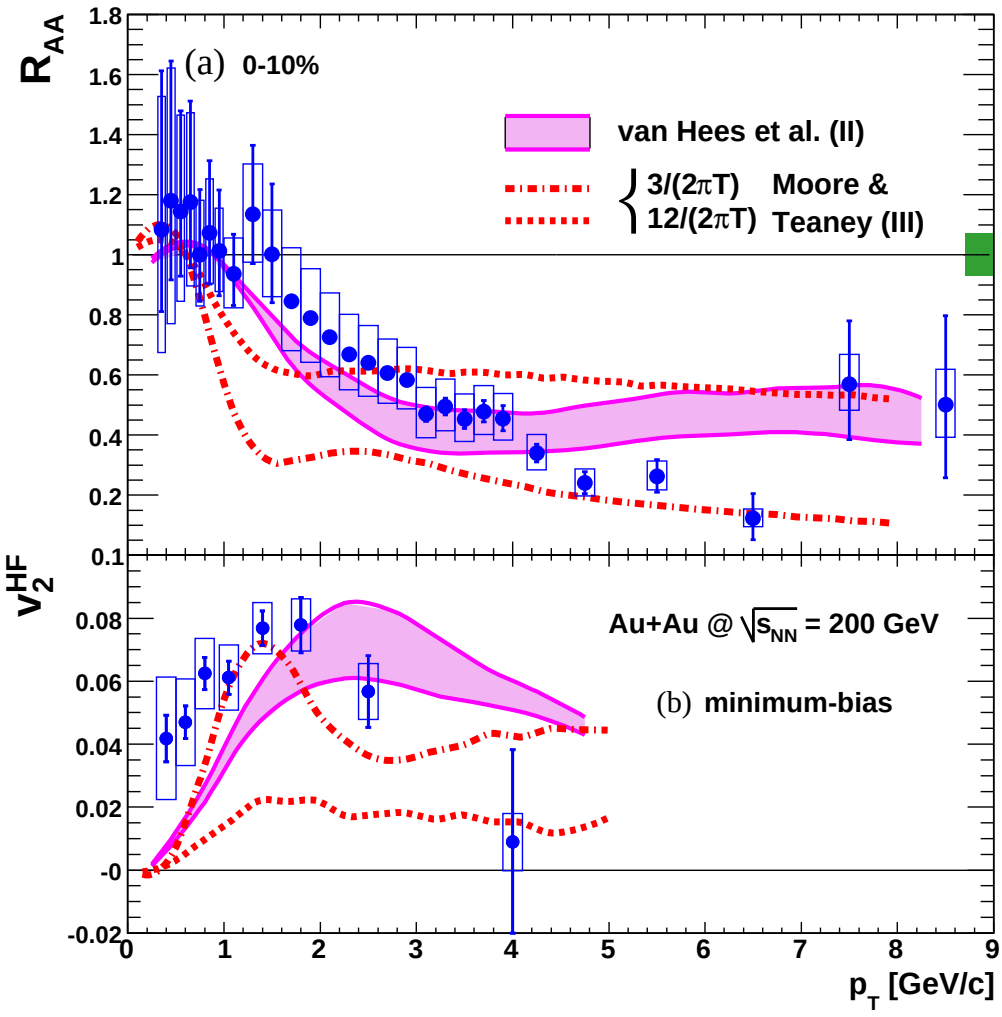

Figure 5.11: Comparison of the Langevin-based models from [42, 46] to the heavy flavor electron R_{AA} for 0-10% centrality and v_2 for minimum-bias collisions.

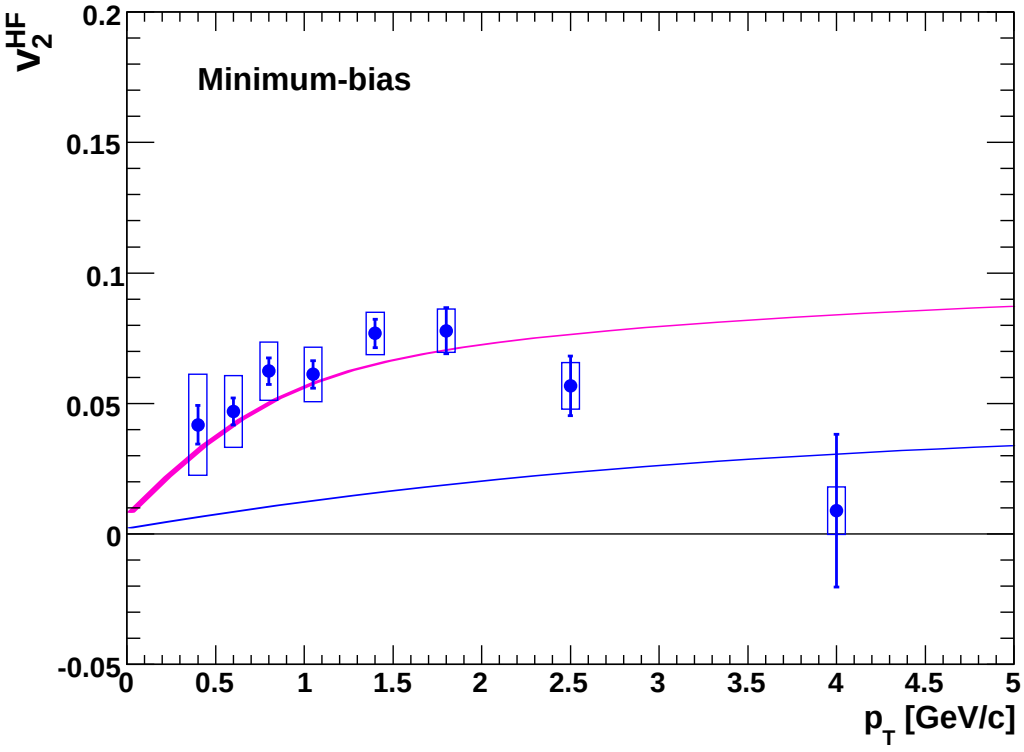

Figure 5.12: v_2 of electrons from heavy flavor decays shown along with various models. The top solid curve [41] and bottom solid curve are hydrodynamical predictions of the heavy flavor electron v_2, assuming that the charm quark v_2 is the same as the v_2 of light quarks, and that the charm quark v_2 is zero, respectively.

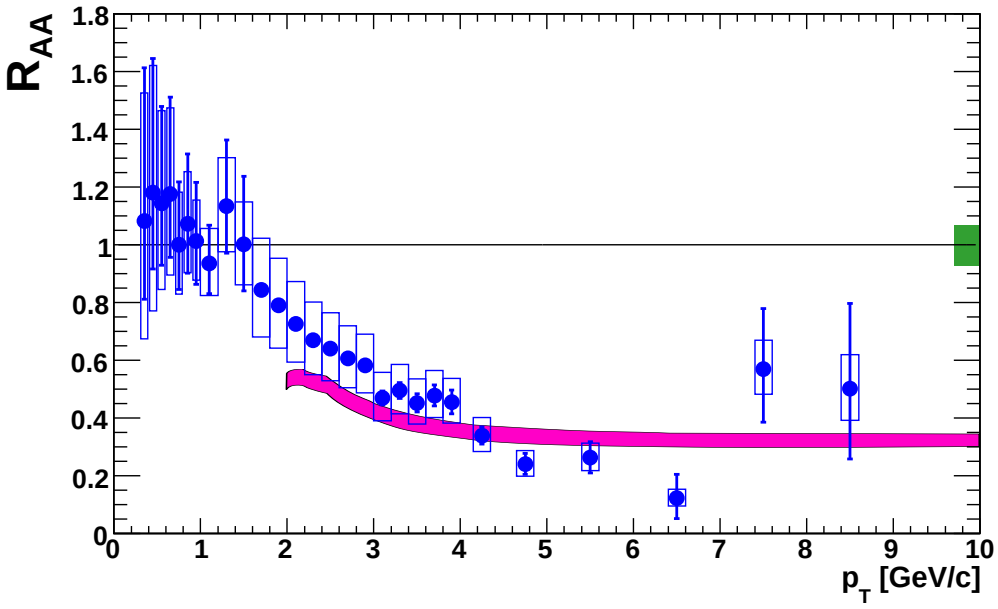

Figure 5.13: R_{AA} for 0-10% compared to a collisional dissociation model from Vitev [39].

charm quark flows just as do the light quarks. This would require the cross section for heavy quark elastic scattering to be surprisingly large.

5.2.3 Other Ideas

Figure 5.13 shows a comparison to a model [39] in which D and B mesons form and then dissociate while still in the medium. An interesting aspect of this model is that suppression is the same for both charm and bottom mesons. In the future, if the D and B contributions can be separated, then the prediction of this model can be tested. It would also be useful if the effect, if any, of the collisional dissociation on the v_2 could be calculated.

Another possibility for describing some of the suppression of the heavy flavor electron spectrum is related to the anomalous baryon/meson enhancement [19]. Figure 5.14 shows the effect of a possible baryon/meson enhancement for charmed hadrons as calculated in [40]. The suppression of the electron spectrum with respect to that of p+p collisions in this model is due to the fact that the semileptonic branching ratio of the Λ_c is smaller than that of the D meson, and that the Λ_c has a softer electron decay spectrum as well. Direct reconstruction of D meson decays in order to accurately measure the D me-

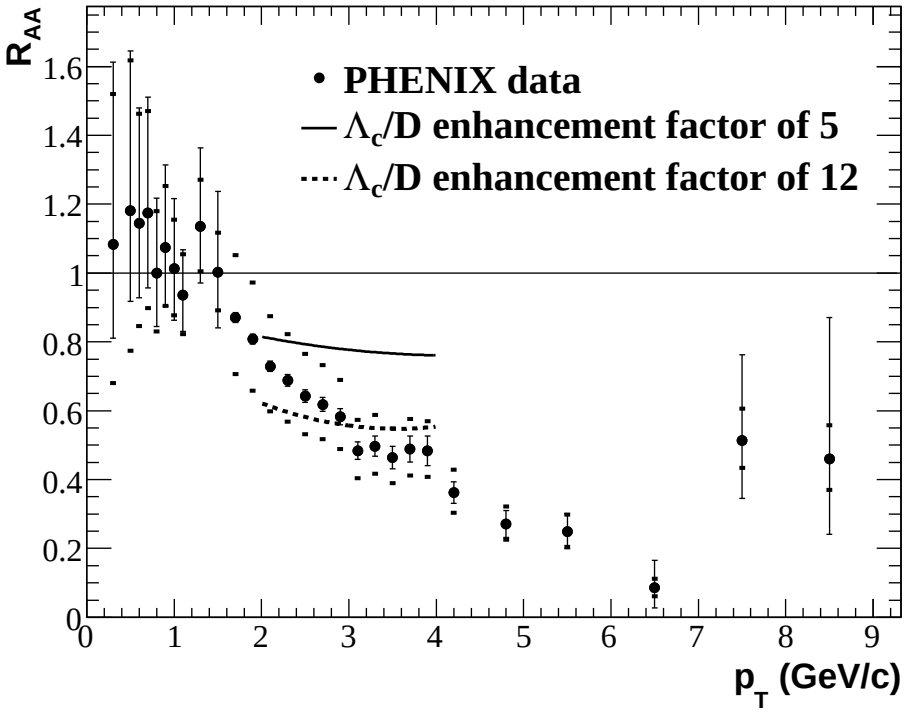

Figure 5.14: Comparison of the R_{AA} for 0-10% centrality to the effect of Λ_c/D enhancement [40].

son cross section will be required to verify the assumption of a baryon/meson enhancement for charm hadrons.

Chapter 6

Summary and Conclusions

This thesis has presented the analysis of the invariant yields of electrons from semileptonic decays of open heavy flavor mesons in Au+Au collisions, as well as the azimuthal anisotropy of the heavy flavor electrons. The nuclear modification factor R_{AA} was calculated from the invariant yield in Au+Au collisions and in p+p collisions. The suppression of heavy flavor electrons from Au+Au collisions relative to those from p+p collisions was shown to be as large as the suppression of light hadrons at high p_T. This unexpected result has generated much theoretical work. It has been found that energy loss models do not describe the heavy flavor suppression very well. Interestingly, if the bottom quarks are ignored, the energy loss calculations agree with the heavy flavor electron R_{AA}. It would perhaps be even more surprising that the bottom quarks were so suppressed than that the suppression is not described by energy loss, especially since perturbative calculations agree nicely with the electron yields from p+p collisions and bottom quark production should occur only in the initial hard scattering of the collision. Secondly, the azimuthal anisotropy v_2 of heavy flavor electrons is significantly underpredicted by energy loss models. This comes as no surprise, since such models, while describing the R_{AA} for light quarks well, also underpredict the v_2 of light quarks.

For a complicated system such as a heavy-ion collision, confidence in a theoretical model comes only by the successful description of multiple observables. Currently the models which do this best are based on collective motion of the medium, i.e. hydrodynamical models. It has been seen that the light quark v_2 is consistent with viscous hydrodynamics (or even ideal hydrodynamics at low p_T). The Langevin-based models described in the previous section do a decent job describing both v_2 and R_{AA}. It would be beneficial to try to describe R_{AA} for the light quarks based on diffusion as well, though the Langevin approach relies on non-relativistic quarks, which makes it unreliable for description of the light quark dynamics. Secondly, the hydrodynamical models should take

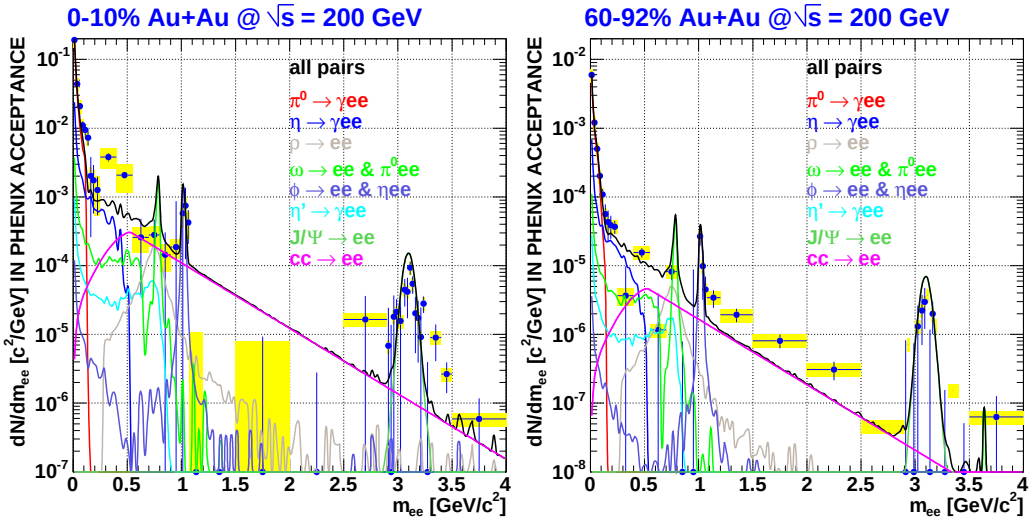

Figure 6.1: Dilepton invariant mass spectrum in central and peripheral Au+Au collisions at $\sqrt{s_{NN}} = 200$ GeV.

gluon radiation effects into account. This would require additional model parameters, and thus also additional experimental observables.

One such additional heavy quark observable is the invariant mass spectrum of dileptons in the mass region between 1-3 GeV/c^2. Although the errors are large, there is evidence for suppression of the mass spectrum in central collisions to that of peripheral collisions in this mass range as can be seen in Figure 6.1. The spectrum in the intermediate mass region is expected to be dominated by correlated decays of charmed mesons. The suppression can come from energy loss alone, but it can also come from scattering of the charm quark. If the charm quarks change direction while traversing the medium, the reconstructed mass of the dileptons from the decay of a charm quark and antiquark will be shifted to a lower value even if there is no energy loss, since the opening angle of the decay changes. It will be interesting to see whether various models for charm quark suppression and flow give different values of the suppression of the dilepton spectrum. Another observable is the correlation between electrons and muons in PHENIX. So far there has not been a successful measurement of such a correlation, partly because the occupancy in the muon arms in central Au+Au collisions is very high.

It is becoming clear that the medium produced at RHIC undergoes collective behavior. Description of obervables is a many-body problem and should be treated as such. That heavy quarks serve as a valuable probe of the medium properties is increasingly clear. But work towards a definitive picture of heavy

quark properties in the medium is just beginning. Currently installed detector upgrades at PHENIX will allow improved measurements of the dilepton invariant mass spectrum and the azimuthal anisotropy. The hadron blind detector [70] will allow much-increased background rejection for the dilepton analysis. A new reaction plane detector allows for improved accuracy in determining the reaction plane. In a few years' time, the Silicon Vertex Detector (VTX) [71] will give accurate reconstruction of the collision vertex and secondary decay vertices, allowing the separation of decays from charm and bottom mesons by their different decay lengths. The separate measurement of charm and bottom hadrons will rule out many of the models currently proposed for heavy quark behavior in the medium. Complimentary to the VTX, the Forward Silicon Upgrade will make the measurement of electron-muon correlations in PHENIX straightforward. The proposed luminosity upgrade to RHIC (RHIC II) would allow the clean reconstruction of B meson decays via $B \rightarrow J/\psi X$. Secondly, the upgrade would provide enough statistical precision to measure the azimuthal anisotropy of open heavy flavor mesons at high p_T. Hopefully, the expansion of the experimental program and theoretical developments will allow for deep insights into the physics of the strong interaction. The data presented in this thesis offer a hint as to the direction these insights will take.

Appendix A

Tables of Inclusive Spectra

p_T	inv. yield	stat. error (+)	stat error (-)	sys. error (+)	sys. error (-)
0.35	1.491883e+00	1.495285e-03	1.495285e-03	1.175850e-01	1.175850e-01
0.45	6.811214e-01	7.671313e-04	7.671313e-04	5.368360e-02	5.368360e-02
0.55	3.325545e-01	4.188075e-04	4.188075e-04	2.621078e-02	2.621078e-02
0.65	1.731617e-01	2.539295e-04	2.539295e-04	1.364800e-02	1.364800e-02
0.75	9.534054e-02	1.620664e-04	1.620664e-04	7.514407e-03	7.514407e-03
0.85	5.453810e-02	1.096479e-04	1.096479e-04	4.298502e-03	4.298502e-03
0.95	3.215971e-02	7.713359e-05	7.713359e-05	2.534716e-03	2.534716e-03
1.10	1.532539e-02	3.299440e-05	3.299440e-05	1.207894e-03	1.207894e-03
1.30	6.167935e-03	1.845100e-05	1.845100e-05	4.861350e-04	4.861350e-04
1.50	2.641616e-03	1.092136e-05	1.092136e-05	2.082029e-04	2.082029e-04
1.70	1.206937e-03	6.776056e-06	6.776056e-06	9.512656e-05	9.512656e-05
1.90	5.759132e-04	4.356358e-06	4.356358e-06	4.539146e-05	4.539146e-05
2.10	2.889565e-04	2.907355e-06	2.907355e-06	2.277454e-05	2.277454e-05
2.30	1.527533e-04	1.981638e-06	1.981638e-06	1.203948e-05	1.203948e-05
2.50	8.535344e-05	1.413361e-06	1.413361e-06	6.727259e-06	6.727259e-06
2.70	4.973165e-05	1.028955e-06	1.028955e-06	3.919674e-06	3.919674e-06
2.90	3.021237e-05	7.603154e-07	7.603154e-07	2.381233e-06	2.381233e-06
3.10	1.666807e-05	5.557380e-07	5.457396e-07	1.313719e-06	1.313719e-06
3.30	1.131693e-05	4.382421e-07	4.291110e-07	8.919605e-07	8.919605e-07
3.50	7.161654e-06	3.397015e-07	3.310735e-07	5.644565e-07	5.644565e-07
3.70	5.043559e-06	2.708260e-07	2.630656e-07	3.975157e-07	3.975157e-07
3.90	3.418182e-06	2.226880e-07	2.149946e-07	2.694091e-07	2.694091e-07
4.25	1.552044e-06	8.952983e-08	8.677989e-08	1.223267e-07	1.223267e-07
4.75	5.729084e-07	5.229313e-08	4.979773e-08	4.515463e-08	4.515463e-08
5.50	2.160928e-07	2.750324e-08	2.570863e-08	1.703168e-08	1.703168e-08
6.50	4.410488e-08	1.146060e-08	1.004800e-08	3.476192e-09	3.476192e-09
7.50	3.628886e-08	9.740928e-09	8.506728e-09	2.860160e-09	2.860160e-09
8.50	1.273069e-08	5.008909e-09	4.123076e-09	1.620954e-09	1.620954e-09

Table A.1: Invariant inclusive $\frac{e^+ + e^-}{2}$ yield, 0-10% centrality. The p_T is in units of GeV/c. The yield and correspondings errors are in units of $(\mathrm{GeV}/c)^{-2}$

p_T	inv. yield	stat. error (+)	stat error (-)	sys. error (+)	sys. error (-)
0.35	1.035092e+00	1.082975e-03	1.082975e-03	8.158229e-02	8.158229e-02
0.45	4.731756e-01	5.559455e-04	5.559455e-04	3.729405e-02	3.729405e-02
0.55	2.327606e-01	3.066667e-04	3.066667e-04	1.834538e-02	1.834538e-02
0.65	1.222868e-01	1.879430e-04	1.879430e-04	9.638217e-03	9.638217e-03
0.75	6.710356e-02	1.212087e-04	1.212087e-04	5.288868e-03	5.288868e-03
0.85	3.867275e-02	8.289411e-05	8.289411e-05	3.048050e-03	3.048050e-03
0.95	2.292925e-02	5.875647e-05	5.875647e-05	1.807203e-03	1.807203e-03
1.10	1.106289e-02	2.557710e-05	2.557710e-05	8.719379e-04	8.719379e-04
1.30	4.499731e-03	1.449822e-05	1.449822e-05	3.546530e-04	3.546530e-04
1.50	1.944079e-03	8.699666e-06	8.699666e-06	1.532255e-04	1.532255e-04
1.70	9.016054e-04	5.459064e-06	5.459064e-06	7.106138e-05	7.106138e-05
1.90	4.375263e-04	3.555597e-06	3.555597e-06	3.448429e-05	3.448429e-05
2.10	2.232886e-04	2.386101e-06	2.386101e-06	1.759882e-05	1.759882e-05
2.30	1.226831e-04	1.672451e-06	1.672451e-06	9.669454e-06	9.669454e-06
2.50	6.739623e-05	1.184031e-06	1.184031e-06	5.311935e-06	5.311935e-06
2.70	3.819877e-05	8.501218e-07	8.501218e-07	3.010693e-06	3.010693e-06
2.90	2.227142e-05	6.244596e-07	6.244596e-07	1.755355e-06	1.755355e-06
3.10	1.428692e-05	4.822257e-07	4.734447e-07	1.126045e-06	1.126045e-06
3.30	8.425257e-06	3.598510e-07	3.516000e-07	6.640492e-07	6.640492e-07
3.50	5.795897e-06	2.890635e-07	2.813543e-07	4.568123e-07	4.568123e-07
3.70	4.313812e-06	2.421894e-07	2.349432e-07	3.399995e-07	3.399995e-07
3.90	2.048477e-06	1.639150e-07	1.570157e-07	1.614538e-07	1.614538e-07
4.25	1.406983e-06	8.037591e-08	7.793030e-08	1.108935e-07	1.108935e-07
4.75	5.084738e-07	4.698805e-08	4.471936e-08	4.007613e-08	4.007613e-08
5.50	1.653589e-07	2.210882e-08	2.059862e-08	1.303301e-08	1.303301e-08
6.50	6.167122e-08	1.278496e-08	1.148933e-08	4.860710e-09	4.860710e-09
7.50	3.274686e-08	8.790158e-09	7.676423e-09	2.580993e-09	2.580993e-09
8.50	1.173105e-08	4.615598e-09	3.799322e-09	1.493673e-09	1.493673e-09

Table A.2: Invariant inclusive $\frac{e^+ + e^-}{2}$ yield, 10-20% centrality. The p_T is in units of GeV/c. The yield and correspondings errors are in units of $(\mathrm{GeV}/c)^{-2}$

p_T	inv. yield	stat. error (+)	stat error (-)	sys. error (+)	sys. error (-)
0.35	5.777272e-01	4.993642e-04	4.993642e-04	4.553444e-02	4.553444e-02
0.45	2.619481e-01	2.554925e-04	2.554925e-04	2.064583e-02	2.064583e-02
0.55	1.292670e-01	1.428990e-04	1.428990e-04	1.018837e-02	1.018837e-02
0.65	6.747644e-02	8.833516e-05	8.833516e-05	5.318257e-03	5.318257e-03
0.75	3.719881e-02	5.775140e-05	5.775140e-05	2.931880e-03	2.931880e-03
0.85	2.150696e-02	3.981809e-05	3.981809e-05	1.695104e-03	1.695104e-03
0.95	1.274666e-02	2.832221e-05	2.832221e-05	1.004647e-03	1.004647e-03
1.10	6.142736e-03	1.245251e-05	1.245251e-05	4.841489e-04	4.841489e-04
1.30	2.519798e-03	7.143485e-06	7.143485e-06	1.986016e-04	1.986016e-04
1.50	1.106377e-03	4.328261e-06	4.328261e-06	8.720073e-05	8.720073e-05
1.70	5.157613e-04	2.739036e-06	2.739036e-06	4.065050e-05	4.065050e-05
1.90	2.528893e-04	1.801350e-06	1.801350e-06	1.993185e-05	1.993185e-05
2.10	1.313262e-04	1.224091e-06	1.224091e-06	1.035067e-05	1.035067e-05
2.30	6.926251e-05	8.460499e-07	8.460499e-07	5.459028e-06	5.459028e-06
2.50	3.919449e-05	6.060842e-07	6.060842e-07	3.089172e-06	3.089172e-06
2.70	2.289108e-05	4.429241e-07	4.429241e-07	1.804194e-06	1.804194e-06
2.90	1.391530e-05	3.338818e-07	3.338818e-07	1.096755e-06	1.096755e-06
3.10	8.762441e-06	2.545458e-07	2.545458e-07	6.906249e-07	6.906249e-07
3.30	5.600370e-06	1.985568e-07	1.947626e-07	4.414015e-07	4.414015e-07
3.50	3.332995e-06	1.492396e-07	1.456562e-07	2.626950e-07	2.626950e-07
3.70	2.407945e-06	1.228363e-07	1.194876e-07	1.897858e-07	1.897858e-07
3.90	1.475929e-06	9.273583e-08	8.964196e-08	1.163276e-07	1.163276e-07
4.25	7.791039e-07	4.091595e-08	3.976856e-08	6.140624e-08	6.140624e-08
4.75	3.379409e-07	2.541977e-08	2.441136e-08	2.663532e-08	2.663532e-08
5.50	1.030127e-07	1.187262e-08	1.116650e-08	8.119098e-09	8.119098e-09
6.50	3.188463e-08	6.239917e-09	5.638985e-09	2.513034e-09	2.513034e-09
7.50	8.709383e-09	3.209666e-09	2.671035e-09	6.864430e-10	6.864430e-10
8.50	4.148566e-09	1.918784e-09	1.533938e-09	5.282224e-10	5.282224e-10

Table A.3: Invariant inclusive $\frac{e^+ + e^-}{2}$ yield, 20-40% centrality. The p_T is in units of GeV/c. The yield and correspondings errors are in units of $(\mathrm{GeV}/c)^{-2}$

p_T	inv. yield	stat. error (+)	stat error (-)	sys. error (+)	sys. error (-)
0.35	2.161603e-01	2.689255e-04	2.689255e-04	1.703699e-02	1.703699e-02
0.45	9.648425e-02	1.362416e-04	1.362416e-04	7.604550e-03	7.604550e-03
0.55	4.713641e-02	7.734091e-05	7.734091e-05	3.715127e-03	3.715127e-03
0.65	2.437187e-02	4.822474e-05	4.822474e-05	1.920905e-03	1.920905e-03
0.75	1.333348e-02	3.177033e-05	3.177033e-05	1.050898e-03	1.050898e-03
0.85	7.655278e-03	2.198957e-05	2.198957e-05	6.033622e-04	6.033622e-04
0.95	4.513813e-03	1.567617e-05	1.567617e-05	3.557629e-04	3.557629e-04
1.10	2.166729e-03	6.921961e-06	6.921961e-06	1.707740e-04	1.707740e-04
1.30	8.955507e-04	4.012455e-06	4.012455e-06	7.058417e-05	7.058417e-05
1.50	4.007672e-04	2.463149e-06	2.463149e-06	3.158707e-05	3.158707e-05
1.70	1.844468e-04	1.556029e-06	1.556029e-06	1.453745e-05	1.453745e-05
1.90	9.212353e-05	1.031909e-06	1.031909e-06	7.260854e-06	7.260854e-06
2.10	4.896816e-05	7.127592e-07	7.127592e-07	3.859499e-06	3.859499e-06
2.30	2.687883e-05	5.030455e-07	5.030455e-07	2.118495e-06	2.118495e-06
2.50	1.532359e-05	3.617840e-07	3.617840e-07	1.207752e-06	1.207752e-06
2.70	8.771987e-06	2.628182e-07	2.628182e-07	6.913773e-07	6.913773e-07
2.90	5.077255e-06	1.958888e-07	1.918220e-07	4.001715e-07	4.001715e-07
3.10	3.357194e-06	1.524513e-07	1.487403e-07	2.646022e-07	2.646022e-07
3.30	2.033574e-06	1.169245e-07	1.133445e-07	1.602792e-07	1.602792e-07
3.50	1.302158e-06	9.069113e-08	8.734977e-08	1.026315e-07	1.026315e-07
3.70	9.953119e-07	7.636287e-08	7.327552e-08	7.844700e-08	7.844700e-08
3.90	5.966597e-07	5.758593e-08	5.468855e-08	4.702663e-08	4.702663e-08
4.25	3.213008e-07	2.516385e-08	2.412622e-08	2.532380e-08	2.532380e-08
4.75	1.649897e-07	1.731351e-08	1.637070e-08	1.300391e-08	1.300391e-08
5.50	4.678935e-08	7.823765e-09	7.167395e-09	3.687773e-09	3.687773e-09
6.50	1.525660e-08	4.239693e-09	3.686576e-09	1.202472e-09	1.202472e-09
7.50	2.771164e-09	1.917935e-09	1.405804e-09	2.184134e-10	2.184134e-10
8.50	6.351683e-10	8.999537e-10	5.362385e-10	8.087376e-11	8.087376e-11

Table A.4: Invariant inclusive $\frac{e^+ + e^-}{2}$ yield, 40-60% centrality. The p_T is in units of GeV/c. The yield and correspondings errors are in units of $(\mathrm{GeV}/c)^{-2}$

p_T	inv. yield	stat. error (+)	stat error (-)	sys. error (+)	sys. error (-)
0.35	4.100043e-02	8.508511e-05	8.508511e-05	3.231510e-03	3.231510e-03
0.45	1.778249e-02	4.231038e-05	4.231038e-05	1.401554e-03	1.401554e-03
0.55	8.440256e-03	2.404261e-05	2.404261e-05	6.652314e-04	6.652314e-04
0.65	4.272161e-03	1.493407e-05	1.493407e-05	3.367168e-04	3.367168e-04
0.75	2.284887e-03	9.799166e-06	9.799166e-06	1.800868e-04	1.800868e-04
0.85	1.282523e-03	6.725017e-06	6.725017e-06	1.010839e-04	1.010839e-04
0.95	7.513735e-04	4.782037e-06	4.782037e-06	5.922063e-05	5.922063e-05
1.10	3.570618e-04	2.120976e-06	2.120976e-06	2.814236e-05	2.814236e-05
1.30	1.448999e-04	1.218421e-06	1.218421e-06	1.142051e-05	1.142051e-05
1.50	6.515799e-05	7.515784e-07	7.515784e-07	5.135524e-06	5.135524e-06
1.70	3.054614e-05	4.790410e-07	4.790410e-07	2.407540e-06	2.407540e-06
1.90	1.541536e-05	3.198374e-07	3.198374e-07	1.214985e-06	1.214985e-06
2.10	7.312805e-06	2.082584e-07	2.082584e-07	5.763697e-07	5.763697e-07
2.30	4.096996e-06	1.504984e-07	1.475208e-07	3.229108e-07	3.229108e-07
2.50	2.419069e-06	1.107567e-07	1.080390e-07	1.906625e-07	1.906625e-07
2.70	1.380235e-06	8.014572e-08	7.766824e-08	1.087853e-07	1.087853e-07
2.90	8.067091e-07	5.922068e-08	5.692562e-08	6.358198e-08	6.358198e-08
3.10	5.531647e-07	4.749508e-08	4.535682e-08	4.359851e-08	4.359851e-08
3.30	3.328159e-07	3.631055e-08	3.425944e-08	2.623138e-08	2.623138e-08
3.50	2.301419e-07	2.906474e-08	2.718191e-08	1.813898e-08	1.813898e-08
3.70	1.685150e-07	2.426391e-08	2.248892e-08	1.328176e-08	1.328176e-08
3.90	1.013590e-07	1.849309e-08	1.681408e-08	7.988763e-09	7.988763e-09
4.25	5.048438e-08	7.746687e-09	7.145835e-09	3.979002e-09	3.979002e-09
4.75	1.181578e-08	3.703789e-09	3.169707e-09	9.312781e-10	9.312781e-10
5.50	4.862496e-09	2.061578e-09	1.674892e-09	3.832449e-10	3.832449e-10
6.50	2.426394e-09	1.417004e-09	1.079866e-09	1.912398e-10	1.912398e-10
7.50	0.000000e+00	0.000000e+00	0.000000e+00	0.000000e+00	0.000000e+00
8.50	0.000000e+00	0.000000e+00	0.000000e+00	0.000000e+00	0.000000e+00

Table A.5: Invariant inclusive $\frac{e^+ + e^-}{2}$ yield, 60-93% centrality. The p_T is in units of GeV/c. The yield and correspondings errors are in units of $(\mathrm{GeV}/c)^{-2}$

p_T	inv. yield	stat. error (+)	stat error (-)	sys. error (+)	sys. error (-)
0.35	4.603955e-01	2.372134e-04	2.372134e-04	3.628676e-02	3.628676e-02
0.45	2.086941e-01	1.212217e-04	1.212217e-04	1.644854e-02	1.644854e-02
0.55	1.021802e-01	6.678366e-05	6.678366e-05	8.053482e-03	8.053482e-03
0.65	5.323798e-02	4.081688e-05	4.081688e-05	4.196031e-03	4.196031e-03
0.75	2.924040e-02	2.630659e-05	2.630659e-05	2.304626e-03	2.304626e-03
0.85	1.679785e-02	1.794619e-05	1.794619e-05	1.323947e-03	1.323947e-03
0.95	9.928285e-03	1.269067e-05	1.269067e-05	7.825126e-04	7.825126e-04
1.10	4.765189e-03	5.506862e-06	5.506862e-06	3.755755e-04	3.755755e-04
1.30	1.937103e-03	3.115900e-06	3.115900e-06	1.526756e-04	1.526756e-04
1.50	8.417381e-04	1.867226e-06	1.867226e-06	6.634285e-05	6.634285e-05
1.70	3.887143e-04	1.169644e-06	1.169644e-06	3.063710e-05	3.063710e-05
1.90	1.888895e-04	7.613294e-07	7.613294e-07	1.488761e-05	1.488761e-05
2.10	9.657180e-05	5.124417e-07	5.124417e-07	7.611451e-06	7.611451e-06
2.30	5.181239e-05	3.545635e-07	3.545635e-07	4.083671e-06	4.083671e-06
2.50	2.904421e-05	2.530660e-07	2.530660e-07	2.289163e-06	2.289163e-06
2.70	1.677559e-05	1.837049e-07	1.837049e-07	1.322193e-06	1.322193e-06
2.90	1.002742e-05	1.362542e-07	1.362542e-07	7.903261e-07	7.903261e-07
3.10	6.139137e-06	1.024328e-07	1.024328e-07	4.838653e-07	4.838653e-07
3.30	3.887851e-06	7.882039e-08	7.882039e-08	3.064268e-07	3.064268e-07
3.50	2.475293e-06	6.099297e-08	6.099297e-08	1.950939e-07	1.950939e-07
3.70	1.800458e-06	4.995494e-08	4.995494e-08	1.419058e-07	1.419058e-07
3.90	1.071004e-06	3.811424e-08	3.738322e-08	8.441279e-08	8.441279e-08
4.25	5.721368e-07	1.649556e-08	1.649556e-08	4.509382e-08	4.509382e-08
4.75	2.284794e-07	9.995652e-09	9.761026e-09	1.800794e-08	1.800794e-08
5.50	7.446769e-08	4.811467e-09	4.646560e-09	5.869282e-09	5.869282e-09
6.50	2.227313e-08	2.416100e-09	2.280355e-09	1.755490e-09	1.755490e-09
7.50	9.854848e-09	1.547548e-09	1.424949e-09	7.767246e-10	7.767246e-10
8.50	3.649691e-09	8.073333e-10	7.207260e-10	4.647024e-10	4.647024e-10

Table A.6: Invariant inclusive $\frac{e^+ + e^-}{2}$ yield, minimum-bias. The p_T is in units of GeV/c. The yield and correspondings errors are in units of $(\mathrm{GeV}/c)^{-2}$

Appendix B

Tables of Heavy-Flavor Spectra

p_T	inv. yield	stat. error (+)	stat error (-)	sys. error (+)	sys. error (-)
0.35	3.350667e-01	1.635373e-02	1.609976e-02	6.704441e-02	6.600323e-02
0.45	1.624346e-01	7.051423e-03	6.952685e-03	2.726586e-02	2.688407e-02
0.55	8.745515e-02	3.590927e-03	3.545359e-03	1.296472e-02	1.280020e-02
0.65	4.832844e-02	2.146073e-03	2.121280e-03	6.867792e-03	6.788449e-03
0.75	2.960370e-02	1.310362e-03	1.296522e-03	3.740589e-03	3.701081e-03
0.85	1.831652e-02	8.654969e-04	8.571076e-04	2.165870e-03	2.144876e-03
0.95	1.292907e-02	6.127168e-04	6.072471e-04	1.367812e-03	1.355602e-03
1.10	6.775290e-03	2.742672e-04	2.656800e-04	7.051445e-04	6.830667e-04
1.30	3.248078e-03	7.078639e-05	6.886887e-05	4.007409e-04	3.898853e-04
1.50	1.499054e-03	3.093746e-05	3.020536e-05	1.909165e-04	1.863987e-04
1.70	6.419135e-04	6.776056e-06	6.776056e-06	9.977046e-05	9.977046e-05
1.90	3.248503e-04	4.356358e-06	4.356358e-06	4.786807e-05	4.786807e-05
2.10	1.697013e-04	2.907355e-06	2.907355e-06	2.412735e-05	2.412735e-05
2.30	9.258812e-05	1.981638e-06	1.981638e-06	1.280226e-05	1.280226e-05
2.50	5.435582e-05	1.413361e-06	1.413361e-06	7.136570e-06	7.136570e-06
2.70	3.248249e-05	1.028955e-06	1.028955e-06	4.159959e-06	4.159959e-06
2.90	2.026280e-05	7.603154e-07	7.603154e-07	2.523365e-06	2.523365e-06
3.10	1.080802e-05	5.557380e-07	5.457396e-07	1.407848e-06	1.407848e-06
3.30	7.700680e-06	4.382421e-07	4.291110e-07	9.472851e-07	9.472851e-07
3.50	4.842494e-06	3.397015e-07	3.310735e-07	6.015197e-07	6.015197e-07
3.70	3.574083e-06	2.708260e-07	2.630656e-07	4.191744e-07	4.191744e-07
3.90	2.409727e-06	2.226880e-07	2.149946e-07	2.845804e-07	2.845804e-07
4.25	1.010988e-06	8.952983e-08	8.677989e-08	1.264091e-07	1.264091e-07
4.75	3.335507e-07	5.229313e-08	4.979773e-08	4.719026e-08	4.719026e-08
5.50	1.280833e-07	2.750324e-08	2.570863e-08	1.739166e-08	1.739166e-08
6.50	1.732316e-08	1.146060e-08	1.004800e-08	3.595053e-09	3.595053e-09
7.50	2.630617e-08	9.740928e-09	8.506728e-09	2.875178e-09	2.875178e-09
8.50	8.490820e-09	5.008909e-09	4.123076e-09	1.625258e-09	1.625258e-09

Table B.1: Invariant heavy-flavor $\frac{e^+ + e^-}{2}$ yield, 0-10% centrality. The p_T is in units of GeV/c. The yield and correspondings errors are in units of $(\mathrm{GeV/c})^{-2}$

p_T	inv. yield	stat. error (+)	stat error (-)	sys. error (+)	sys. error (-)
0.35	1.903841e-01	1.106154e-02	1.091197e-02	4.481281e-02	4.420684e-02
0.45	9.110863e-02	4.808281e-03	4.749031e-03	1.789520e-02	1.767469e-02
0.55	5.293131e-02	2.522277e-03	2.493838e-03	8.571829e-03	8.475181e-03
0.65	2.922360e-02	1.530294e-03	1.514447e-03	4.550146e-03	4.503027e-03
0.75	1.883808e-02	9.508073e-04	9.417329e-04	2.474193e-03	2.450579e-03
0.85	1.286843e-02	6.417746e-04	6.361117e-04	1.468132e-03	1.455177e-03
0.95	7.928164e-03	4.498539e-04	4.461731e-04	8.768446e-04	8.696700e-04
1.10	4.469994e-03	2.065630e-04	2.005738e-04	4.685667e-04	4.549809e-04
1.30	2.202032e-03	5.024749e-05	4.897341e-05	2.499607e-04	2.436227e-04
1.50	1.011180e-03	2.236916e-05	2.186900e-05	1.156519e-04	1.130660e-04
1.70	4.715567e-04	5.459064e-06	5.459064e-06	7.241960e-05	7.241960e-05
1.90	2.437213e-04	3.555597e-06	3.555597e-06	3.528991e-05	3.528991e-05
2.10	1.295680e-04	2.386101e-06	2.386101e-06	1.808058e-05	1.808058e-05
2.30	7.549216e-05	1.672451e-06	1.672451e-06	9.942776e-06	9.942776e-06
2.50	4.255069e-05	1.184031e-06	1.184031e-06	5.474828e-06	5.474828e-06
2.70	2.430156e-05	8.501218e-07	8.501218e-07	3.113310e-06	3.113310e-06
2.90	1.441243e-05	6.244596e-07	6.244596e-07	1.817839e-06	1.817839e-06
3.10	9.621804e-06	4.822257e-07	4.734447e-07	1.163476e-06	1.163476e-06
3.30	5.570602e-06	3.598510e-07	3.516000e-07	6.894565e-07	6.894565e-07
3.50	3.975491e-06	2.890635e-07	2.813543e-07	4.726776e-07	4.726776e-07
3.70	3.126662e-06	2.421894e-07	2.349432e-07	3.494992e-07	3.494992e-07
3.90	1.258842e-06	1.639150e-07	1.570157e-07	1.704442e-07	1.704442e-07
4.25	9.844817e-07	8.037591e-08	7.793030e-08	1.125493e-07	1.125493e-07
4.75	3.266698e-07	4.698805e-08	4.471936e-08	4.091695e-08	4.091695e-08
5.50	1.004746e-07	2.210882e-08	2.059862e-08	1.320552e-08	1.320552e-08
6.50	4.246044e-08	1.278496e-08	1.148933e-08	4.895154e-09	4.895154e-09
7.50	2.569856e-08	8.790158e-09	7.676423e-09	2.588782e-09	2.588782e-09
8.50	8.803060e-09	4.615598e-09	3.799322e-09	1.496154e-09	1.496154e-09

Table B.2: Invariant heavy-flavor $\frac{e^+ + e^-}{2}$ yield, 10-20% centrality. The p_T is in units of GeV/c. The yield and correspondings errors are in units of $(\mathrm{GeV/c})^{-2}$

p_T	inv. yield	stat. error (+)	stat error (-)	sys. error (+)	sys. error (-)
0.35	7.353340e-02	5.149162e-03	5.086625e-03	2.478409e-02	2.448308e-02
0.45	4.186298e-02	2.301373e-03	2.275755e-03	9.854265e-03	9.744572e-03
0.55	2.249248e-02	1.202618e-03	1.190304e-03	4.657794e-03	4.610100e-03
0.65	1.551910e-02	7.545864e-04	7.474552e-04	2.504387e-03	2.480719e-03
0.75	8.925450e-03	4.634355e-04	4.593809e-04	1.325222e-03	1.313627e-03
0.85	6.503663e-03	3.155637e-04	3.130004e-04	7.826476e-04	7.762904e-04
0.95	3.789720e-03	2.208368e-04	2.191670e-04	4.661339e-04	4.626093e-04
1.10	2.375172e-03	1.025529e-04	9.978802e-05	2.507644e-04	2.440036e-04
1.30	1.147084e-03	2.768141e-05	2.702475e-05	1.260463e-04	1.230562e-04
1.50	5.447096e-04	1.236249e-05	1.210248e-05	6.072386e-05	5.944672e-05
1.70	2.578188e-04	2.739036e-06	2.739036e-06	4.168299e-05	4.168299e-05
1.90	1.330077e-04	1.801350e-06	1.801350e-06	2.057599e-05	2.057599e-05
2.10	7.302256e-05	1.224091e-06	1.224091e-06	1.073426e-05	1.073426e-05
2.30	3.983785e-05	8.460499e-07	8.460499e-07	5.687276e-06	5.687276e-06
2.50	2.333138e-05	6.060842e-07	6.060842e-07	3.228379e-06	3.228379e-06
2.70	1.424472e-05	4.429241e-07	4.429241e-07	1.885621e-06	1.885621e-06
2.90	8.948615e-06	3.338818e-07	3.338818e-07	1.146048e-06	1.146048e-06
3.10	5.770037e-06	2.545458e-07	2.545458e-07	7.217196e-07	7.217196e-07
3.30	3.760352e-06	1.985568e-07	1.947626e-07	4.612115e-07	4.612115e-07
3.50	2.180943e-06	1.492396e-07	1.456562e-07	2.763963e-07	2.763963e-07
3.70	1.662955e-06	1.228363e-07	1.194876e-07	1.981083e-07	1.981083e-07
3.90	9.774605e-07	9.273583e-08	8.964196e-08	1.225590e-07	1.225590e-07
4.25	5.162194e-07	4.091595e-08	3.976856e-08	6.285338e-08	6.285338e-08
4.75	2.262403e-07	2.541977e-08	2.441136e-08	2.723224e-08	2.723224e-08
5.50	6.368838e-08	1.187262e-08	1.116650e-08	8.245451e-09	8.245451e-09
6.50	2.061599e-08	6.239917e-09	5.638985e-09	2.540074e-09	2.540074e-09
7.50	4.719650e-09	3.209666e-09	2.671035e-09	6.965133e-10	6.965133e-10
8.50	2.514086e-09	1.918784e-09	1.533938e-09	5.303431e-10	5.303431e-10

Table B.3: Invariant heavy-flavor $\frac{e^+ + e^-}{2}$ yield, 20-40% centrality. The p_T is in units of GeV/c. The yield and correspondings errors are in units of $(\mathrm{GeV/c})^{-2}$

p_T	inv. yield	stat. error (+)	stat error (-)	sys. error (+)	sys. error (-)
0.35	2.135496e-02	2.665013e-03	2.634273e-03	9.415547e-03	9.306943e-03
0.45	1.361377e-02	1.194672e-03	1.182024e-03	3.686654e-03	3.647622e-03
0.55	8.482472e-03	6.442668e-04	6.379840e-04	1.718431e-03	1.701673e-03
0.65	4.303755e-03	3.999993e-04	3.963948e-04	9.020865e-04	8.939575e-04
0.75	2.779164e-03	2.507915e-04	2.486969e-04	4.732680e-04	4.693154e-04
0.85	2.030766e-03	1.709788e-04	1.696516e-04	2.744464e-04	2.723161e-04
0.95	1.414111e-03	1.228455e-04	1.219570e-04	1.678002e-04	1.665866e-04
1.10	7.483684e-04	5.696234e-05	5.549058e-05	8.646759e-05	8.423348e-05
1.30	4.052883e-04	1.053077e-05	1.029100e-05	4.227065e-05	4.130822e-05
1.50	1.983069e-04	4.998499e-06	4.897461e-06	2.103959e-05	2.061431e-05
1.70	8.686324e-05	1.556029e-06	1.556029e-06	1.492618e-05	1.492618e-05
1.90	4.636991e-05	1.031909e-06	1.031909e-06	7.505510e-06	7.505510e-06
2.10	2.627386e-05	7.127592e-07	7.127592e-07	4.009250e-06	4.009250e-06
2.30	1.514460e-05	5.030455e-07	5.030455e-07	2.209810e-06	2.209810e-06
2.50	9.005039e-06	3.617840e-07	3.617840e-07	1.263288e-06	1.263288e-06
2.70	5.223555e-06	2.628182e-07	2.628182e-07	7.268297e-07	7.268297e-07
2.90	3.032954e-06	1.958888e-07	1.918220e-07	4.231267e-07	4.231267e-07
3.10	2.140611e-06	1.524513e-07	1.487403e-07	2.782857e-07	2.782857e-07
3.30	1.279412e-06	1.169245e-07	1.133445e-07	1.696468e-07	1.696468e-07
3.50	8.247171e-07	9.069113e-08	8.734977e-08	1.089020e-07	1.089020e-07
3.70	6.861384e-07	7.636287e-08	7.327552e-08	8.209629e-08	8.209629e-08
3.90	3.907554e-07	5.758593e-08	5.468855e-08	4.982551e-08	4.982551e-08
4.25	2.128347e-07	2.516385e-08	2.412622e-08	2.596782e-08	2.596782e-08
4.75	1.195993e-07	1.731351e-08	1.637070e-08	1.322841e-08	1.322841e-08
5.50	3.106563e-08	7.823765e-09	7.167395e-09	3.738918e-09	3.738918e-09
6.50	1.086876e-08	4.239693e-09	3.686576e-09	1.213065e-09	1.213065e-09
7.50	1.261656e-09	1.917935e-09	1.405804e-09	2.244293e-10	2.244293e-10
8.50	3.380977e-11	8.999537e-10	5.362385e-10	8.352278e-11	8.352278e-11

Table B.4: Invariant heavy-flavor $\frac{e^+ + e^-}{2}$ yield, 40-60% centrality. The p_T is in units of GeV/c. The yield and correspondings errors are in units of $(\mathrm{GeV/c})^{-2}$

p_T	inv. yield	stat. error (+)	stat error (-)	sys. error (+)	sys. error (-)
0.35	5.279761e-03	8.564079e-04	8.468157e-04	2.160831e-03	2.136628e-03
0.45	1.824913e-03	3.683974e-04	3.645824e-04	8.056377e-04	7.972946e-04
0.55	1.184154e-03	2.008561e-04	1.989272e-04	3.722995e-04	3.687242e-04
0.65	7.894930e-04	1.260959e-04	1.249700e-04	1.931146e-04	1.913903e-04
0.75	4.269219e-04	7.872620e-05	7.807088e-05	9.853379e-05	9.771359e-05
0.85	2.302154e-04	5.278509e-05	5.237452e-05	5.384877e-05	5.342993e-05
0.95	1.992678e-04	3.805328e-05	3.777609e-05	3.290318e-05	3.266350e-05
1.10	1.266385e-04	1.783049e-05	1.736343e-05	1.737831e-05	1.692311e-05
1.30	6.150577e-05	2.082262e-06	2.033800e-06	1.038970e-05	1.014790e-05
1.50	2.987240e-05	1.083589e-06	1.061035e-06	5.207583e-06	5.099192e-06
1.70	1.332989e-05	4.790410e-07	4.790410e-07	2.523586e-06	2.523586e-06
1.90	7.201823e-06	3.198374e-07	3.198374e-07	1.286811e-06	1.286811e-06
2.10	3.157647e-06	2.082584e-07	2.082584e-07	6.255564e-07	6.255564e-07
2.30	1.889733e-06	1.504984e-07	1.475208e-07	3.530975e-07	3.530975e-07
2.50	1.205418e-06	1.107567e-07	1.080390e-07	2.088062e-07	2.088062e-07
2.70	6.846784e-07	8.014572e-08	7.766824e-08	1.206244e-07	1.206244e-07
2.90	3.975175e-07	5.922068e-08	5.692562e-08	7.133372e-08	7.133372e-08
3.10	3.066895e-07	4.749508e-08	4.535682e-08	4.808686e-08	4.808686e-08
3.30	1.781469e-07	3.631055e-08	3.425944e-08	2.935137e-08	2.935137e-08
3.50	1.320064e-07	2.906474e-08	2.718191e-08	2.005851e-08	2.005851e-08
3.70	1.037971e-07	2.426391e-08	2.248892e-08	1.447522e-08	1.447522e-08
3.90	5.881001e-08	1.849309e-08	1.681408e-08	8.860009e-09	8.860009e-09
4.25	2.767120e-08	7.746687e-09	7.145835e-09	4.200387e-09	4.200387e-09
4.75	2.249174e-09	3.703789e-09	3.169707e-09	1.085120e-09	1.085120e-09
5.50	1.599213e-09	2.061578e-09	1.674892e-09	4.067871e-10	4.067871e-10
6.50	1.541568e-09	1.417004e-09	1.079866e-09	1.940980e-10	1.940980e-10
7.50	-2.942736e-10	0.000000e+00	0.000000e+00	1.044452e-11	1.044452e-11
8.50	-1.151854e-10	0.000000e+00	0.000000e+00	4.504857e-12	4.504857e-12

Table B.5: Invariant heavy-flavor $\frac{e^+ + e^-}{2}$ yield, 60-93% centrality. The p_T is in units of GeV/c. The yield and correspondings errors are in units of $(\mathrm{GeV/c})^{-2}$

p_T	inv. yield	stat. error (+)	stat error (-)	sys. error (+)	sys. error (-)
0.35	7.296759e-02	3.011908e-03	2.969054e-03	1.937629e-02	1.910060e-02
0.45	3.744327e-02	1.287068e-03	1.270505e-03	7.730487e-03	7.631002e-03
0.55	2.089250e-02	6.550261e-04	6.473651e-04	3.656483e-03	3.613718e-03
0.65	1.220534e-02	3.857815e-04	3.816632e-04	1.944272e-03	1.923516e-03
0.75	7.459930e-03	2.322290e-04	2.299572e-04	1.040195e-03	1.030019e-03
0.85	5.036477e-03	1.538858e-04	1.525013e-04	6.089836e-04	6.035045e-04
0.95	3.268526e-03	1.059981e-04	1.051180e-04	3.699813e-04	3.669094e-04
1.10	1.843947e-03	4.735482e-05	4.597073e-05	1.952639e-04	1.895568e-04
1.30	8.211567e-04	2.038183e-05	1.986486e-05	9.038323e-05	8.809074e-05
1.50	3.902189e-04	8.814539e-06	8.618718e-06	4.353969e-05	4.257243e-05
1.70	1.991510e-04	1.169644e-06	1.169644e-06	3.126895e-05	3.126895e-05
1.90	1.025193e-04	7.613294e-07	7.613294e-07	1.528622e-05	1.528622e-05
2.10	5.477786e-05	5.124417e-07	5.124417e-07	7.858321e-06	7.858321e-06
2.30	3.063412e-05	3.545635e-07	3.545635e-07	4.234150e-06	4.234150e-06
2.50	1.783867e-05	2.530660e-07	2.530660e-07	2.380689e-06	2.380689e-06
2.70	1.055717e-05	1.837049e-07	1.837049e-07	1.379645e-06	1.379645e-06
2.90	6.459583e-06	1.362542e-07	1.362542e-07	8.264860e-07	8.264860e-07
3.10	4.014782e-06	1.024328e-07	1.024328e-07	5.072676e-07	5.072676e-07
3.30	2.579285e-06	7.882039e-08	7.882039e-08	3.218052e-07	3.218052e-07
3.50	1.644927e-06	6.099297e-08	6.099297e-08	2.055687e-07	2.055687e-07
3.70	1.265133e-06	4.995494e-08	4.995494e-08	1.483074e-07	1.483074e-07
3.90	7.110850e-07	3.811424e-08	3.738322e-08	8.948502e-08	8.948502e-08
4.25	3.805730e-07	1.649556e-08	1.649556e-08	4.630876e-08	4.630876e-08
4.75	1.460155e-07	9.995652e-09	9.761026e-09	1.858867e-08	1.858867e-08
5.50	4.503126e-08	4.811467e-09	4.646560e-09	5.992483e-09	5.992483e-09
6.50	1.364675e-08	2.416100e-09	2.280355e-09	1.785580e-09	1.785580e-09
7.50	6.736508e-09	1.547548e-09	1.424949e-09	7.839460e-10	7.839460e-10
8.50	2.357256e-09	8.073333e-10	7.207260e-10	4.664779e-10	4.664779e-10

Table B.6: Invariant heavy-flavor $\frac{e^+ + e^-}{2}$ yield, minimum-bias. The p_T is in units of GeV/c. The yield and correspondings errors are in units of $(\mathrm{GeV/c})^{-2}$

Appendix C

Tables of R_{AA}

p_T	R_{AA}	stat. error (+)	stat error (-)	sys. error (+)	sys. error (-)
0.35	1.083256e+00	5.294642e-01	2.720851e-01	4.434720e-01	4.086587e-01
0.45	1.180712e+00	4.646729e-01	2.640062e-01	4.408290e-01	4.098639e-01
0.55	1.144111e+00	3.356466e-01	2.152715e-01	3.209574e-01	2.994916e-01
0.65	1.175300e+00	3.359620e-01	2.182816e-01	2.983512e-01	2.792175e-01
0.75	1.000439e+00	2.171763e-01	1.554989e-01	1.814075e-01	1.707970e-01
0.85	1.073578e+00	2.403959e-01	1.709837e-01	1.793838e-01	1.694586e-01
0.95	1.013255e+00	2.030643e-01	1.497649e-01	1.425381e-01	1.353642e-01
1.10	9.363802e-01	1.315761e-01	1.058525e-01	1.196756e-01	1.122975e-01
1.30	1.134813e+00	2.289315e-01	1.642093e-01	1.672271e-01	1.586702e-01
1.50	1.001654e+00	2.349211e-01	1.607610e-01	1.468293e-01	1.404481e-01
1.70	8.445957e-01	8.915575e-03	8.915575e-03	1.786655e-01	1.630027e-01
1.90	7.899244e-01	1.059317e-02	1.059317e-02	1.632041e-01	1.481704e-01
2.10	7.261662e-01	1.244081e-02	1.244081e-02	1.464412e-01	1.322462e-01
2.30	6.690636e-01	1.431978e-02	1.431978e-02	1.323238e-01	1.189594e-01
2.50	6.405859e-01	1.665653e-02	1.665653e-02	1.243243e-01	1.112568e-01
2.70	6.059947e-01	1.919623e-02	1.919623e-02	1.135051e-01	1.006402e-01
2.90	5.832601e-01	2.188550e-02	2.188550e-02	1.078934e-01	9.533555e-02
3.10	4.694156e-01	2.413689e-02	2.370264e-02	8.861965e-02	7.874241e-02
3.30	4.948574e-01	2.816211e-02	2.757533e-02	9.105690e-02	8.033827e-02
3.50	4.525103e-01	3.174365e-02	3.093740e-02	8.362172e-02	7.386770e-02
3.70	4.782032e-01	3.623583e-02	3.519751e-02	8.623876e-02	7.564110e-02
3.90	4.552640e-01	4.207192e-02	4.061841e-02	8.233725e-02	7.228081e-02
4.25	3.391648e-01	3.003534e-02	2.911280e-02	6.282528e-02	5.553412e-02
4.75	2.402794e-01	3.767031e-02	3.587271e-02	4.717805e-02	4.233965e-02
5.50	2.624563e-01	5.635708e-02	5.267972e-02	5.048304e-02	4.507520e-02
6.50	1.233229e-01	8.158756e-02	7.153131e-02	3.040427e-02	2.846621e-02
7.50	5.692529e-01	2.107890e-01	1.840815e-01	9.979746e-02	8.676701e-02
8.50	5.015716e-01	2.958874e-01	2.435592e-01	1.179960e-01	1.097075e-01

Table C.1: R_{AA}, 0-10% centrality. The p_T is in units of GeV/c.

p_T	R_{AA}	stat. error (+)	stat error (-)	sys. error (+)	sys. error (-)
0.35	9.724098e-01	4.762732e-01	2.461261e-01	3.753945e-01	3.417243e-01
0.45	1.046270e+00	4.129585e-01	2.360064e-01	3.667938e-01	3.371594e-01
0.55	1.093993e+00	3.220319e-01	2.075102e-01	2.955882e-01	2.741436e-01
0.65	1.122790e+00	3.224611e-01	2.108111e-01	2.748327e-01	2.557392e-01
0.75	1.005774e+00	2.196928e-01	1.581967e-01	1.786898e-01	1.678120e-01
0.85	1.191613e+00	2.675024e-01	1.907297e-01	1.961980e-01	1.851660e-01
0.95	9.816189e-01	1.990945e-01	1.482462e-01	1.350606e-01	1.279448e-01
1.10	9.760008e-01	1.388580e-01	1.123664e-01	1.223263e-01	1.146391e-01
1.30	1.215459e+00	2.453384e-01	1.760680e-01	1.702501e-01	1.613528e-01
1.50	1.067451e+00	2.504971e-01	1.715264e-01	1.436927e-01	1.370071e-01
1.70	9.802237e-01	1.134774e-02	1.134774e-02	2.056034e-01	1.872552e-01
1.90	9.362990e-01	1.365946e-02	1.365946e-02	1.913147e-01	1.732762e-01
2.10	8.759264e-01	1.613090e-02	1.613090e-02	1.748684e-01	1.575534e-01
2.30	8.618524e-01	1.909345e-02	1.909345e-02	1.663970e-01	1.487129e-01
2.50	7.922401e-01	2.204516e-02	2.204516e-02	1.521792e-01	1.358305e-01
2.70	7.162633e-01	2.505646e-02	2.505646e-02	1.341217e-01	1.189111e-01
2.90	6.554186e-01	2.839789e-02	2.839789e-02	1.218788e-01	1.078507e-01
3.10	6.602169e-01	3.308876e-02	3.248624e-02	1.205451e-01	1.061183e-01
3.30	5.655513e-01	3.653362e-02	3.569593e-02	1.043029e-01	9.208471e-02
3.50	5.869067e-01	4.267481e-02	4.153668e-02	1.064086e-01	9.348070e-02
3.70	6.609183e-01	5.119434e-02	4.966263e-02	1.168977e-01	1.019220e-01
3.90	3.757385e-01	4.892525e-02	4.686595e-02	7.221670e-02	6.446800e-02
4.25	5.217848e-01	4.260001e-02	4.130381e-02	9.308343e-02	8.137587e-02
4.75	3.717770e-01	5.347624e-02	5.089429e-02	6.890531e-02	6.091820e-02
5.50	3.252668e-01	7.157298e-02	6.668400e-02	6.160162e-02	5.478192e-02
6.50	4.775512e-01	1.437920e-01	1.292202e-01	8.546633e-02	7.479051e-02
7.50	8.785680e-01	3.005130e-01	2.624372e-01	1.496296e-01	1.288346e-01
8.50	8.215535e-01	4.307549e-01	3.545752e-01	1.794415e-01	1.647293e-01

Table C.2: R_{AA}, 10-20% centrality. The p_T is in units of GeV/c.

p_T	R_{AA}	stat. error (+)	stat error (-)	sys. error (+)	sys. error (-)
0.35	7.649736e-01	3.758649e-01	1.958757e-01	2.982381e-01	2.706829e-01
0.45	9.791684e-01	3.867676e-01	2.213868e-01	3.293813e-01	2.999178e-01
0.55	9.468525e-01	2.796633e-01	1.810440e-01	2.487224e-01	2.290297e-01
0.65	1.214436e+00	3.479815e-01	2.268318e-01	2.939899e-01	2.731163e-01
0.75	9.705921e-01	2.123377e-01	1.531249e-01	1.729269e-01	1.622976e-01
0.85	1.226622e+00	2.749981e-01	1.958447e-01	1.985046e-01	1.869159e-01
0.95	9.556976e-01	1.942516e-01	1.448918e-01	1.340239e-01	1.271313e-01
1.10	1.056286e+00	1.492702e-01	1.204650e-01	1.311906e-01	1.229489e-01
1.30	1.289600e+00	2.605006e-01	1.870767e-01	1.715494e-01	1.619859e-01
1.50	1.171191e+00	2.749056e-01	1.882904e-01	1.538581e-01	1.466189e-01
1.70	1.091563e+00	1.159664e-02	1.159664e-02	2.353144e-01	2.154858e-01
1.90	1.040737e+00	1.409491e-02	1.409491e-02	2.198624e-01	2.005337e-01
2.10	1.005472e+00	1.685491e-02	1.685491e-02	2.057630e-01	1.864244e-01
2.30	9.263391e-01	1.967298e-02	1.967298e-02	1.858197e-01	1.676050e-01
2.50	8.847768e-01	2.298403e-02	2.298403e-02	1.758552e-01	1.582791e-01
2.70	8.551367e-01	2.658954e-02	2.658954e-02	1.625807e-01	1.447293e-01
2.90	8.288588e-01	3.092555e-02	3.092555e-02	1.552100e-01	1.376089e-01
3.10	8.064025e-01	3.557453e-02	3.557453e-02	1.494255e-01	1.320967e-01
3.30	7.775735e-01	4.105800e-02	4.027341e-02	1.428604e-01	1.259890e-01
3.50	6.557913e-01	4.487511e-02	4.379762e-02	1.222388e-01	1.082404e-01
3.70	7.159626e-01	5.288552e-02	5.144376e-02	1.299299e-01	1.141764e-01
3.90	5.942329e-01	5.637740e-02	5.449653e-02	1.102431e-01	9.749094e-02
4.25	5.572642e-01	4.416919e-02	4.293058e-02	1.020299e-01	8.989101e-02
4.75	5.244288e-01	5.892346e-02	5.658594e-02	9.555162e-02	8.406466e-02
5.50	4.199395e-01	7.828404e-02	7.362813e-02	7.898558e-02	7.011239e-02
6.50	4.722618e-01	1.429412e-01	1.291753e-01	8.688874e-02	7.665814e-02
7.50	3.286392e-01	2.234959e-01	1.859898e-01	6.589764e-02	5.943276e-02
8.50	4.778872e-01	3.647299e-01	2.915769e-01	1.200339e-01	1.126714e-01

Table C.3: R_{AA}, 20-40% centrality. The p_T is in units of GeV/c.

p_T	R_{AA}	stat. error (+)	stat error (-)	sys. error (+)	sys. error (-)
0.35	7.271537e-01	3.650928e-01	2.004574e-01	3.459949e-01	3.234811e-01
0.45	1.042249e+00	4.178113e-01	2.459866e-01	3.513386e-01	3.195094e-01
0.55	1.168781e+00	3.509226e-01	2.320438e-01	3.067203e-01	2.825727e-01
0.65	1.102354e+00	3.277122e-01	2.233460e-01	2.708271e-01	2.514586e-01
0.75	9.892054e-01	2.283933e-01	1.720432e-01	1.853283e-01	1.747833e-01
0.85	1.253655e+00	2.939980e-01	2.176989e-01	2.044068e-01	1.924603e-01
0.95	1.167246e+00	2.488837e-01	1.920764e-01	1.613724e-01	1.529376e-01
1.10	1.089350e+00	1.684078e-01	1.409410e-01	1.408482e-01	1.323104e-01
1.30	1.491384e+00	3.016034e-01	2.168092e-01	1.962494e-01	1.855197e-01
1.50	1.395616e+00	3.279408e-01	2.248750e-01	1.753349e-01	1.666844e-01
1.70	1.203749e+00	2.156342e-02	2.156342e-02	2.686917e-01	2.476383e-01
1.90	1.187589e+00	2.642842e-02	2.642842e-02	2.571568e-01	2.356885e-01
2.10	1.184138e+00	3.212338e-02	3.212338e-02	2.470770e-01	2.247840e-01
2.30	1.152650e+00	3.828662e-02	3.828662e-02	2.336491e-01	2.112456e-01
2.50	1.117750e+00	4.490640e-02	4.490640e-02	2.236486e-01	2.016084e-01
2.70	1.026392e+00	5.164195e-02	5.164195e-02	1.998914e-01	1.790344e-01
2.90	9.195095e-01	5.938818e-02	5.815524e-02	1.793258e-01	1.606699e-01
3.10	9.792120e-01	6.973810e-02	6.804052e-02	1.846384e-01	1.640060e-01
3.30	8.659427e-01	7.913786e-02	7.671478e-02	1.648010e-01	1.467445e-01
3.50	8.116935e-01	8.925897e-02	8.597038e-02	1.541833e-01	1.372217e-01
3.70	9.669128e-01	1.076113e-01	1.032606e-01	1.757966e-01	1.545660e-01
3.90	7.775496e-01	1.145881e-01	1.088227e-01	1.453485e-01	1.288045e-01
4.25	7.520296e-01	8.891389e-02	8.524751e-02	1.378152e-01	1.214508e-01
4.75	9.074252e-01	1.313613e-01	1.242080e-01	1.598268e-01	1.391665e-01
5.50	6.704593e-01	1.688527e-01	1.546869e-01	1.221361e-01	1.074474e-01
6.50	8.149371e-01	3.178913e-01	2.764187e-01	1.440139e-01	1.255299e-01
7.50	2.875518e-01	4.371285e-01	3.204056e-01	6.413054e-02	5.909665e-02
8.50	2.103552e-02	5.599266e-01	3.336330e-01	5.172636e-02	5.169426e-02

Table C.4: R_{AA}, 40-60% centrality. The p_T is in units of GeV/c.

p_T	R_{AA}	stat. error (+)	stat error (-)	sys. error (+)	sys. error (-)
0.35	1.109500e+00	5.688024e-01	3.263213e-01	5.011793e-01	4.658178e-01
0.45	8.622252e-01	3.795277e-01	2.558890e-01	3.978841e-01	3.766448e-01
0.55	1.006942e+00	3.387132e-01	2.506865e-01	3.358619e-01	3.180144e-01
0.65	1.247980e+00	4.048715e-01	2.995751e-01	3.474400e-01	3.275978e-01
0.75	9.377918e-01	2.638677e-01	2.212906e-01	2.250537e-01	2.165268e-01
0.85	8.770782e-01	2.780206e-01	2.400905e-01	2.110847e-01	2.044534e-01
0.95	1.015084e+00	2.768505e-01	2.393082e-01	1.774961e-01	1.711760e-01
1.10	1.137636e+00	2.215622e-01	1.971776e-01	1.698160e-01	1.609820e-01
1.30	1.396776e+00	2.840929e-01	2.051998e-01	2.639678e-01	2.539296e-01
1.50	1.297430e+00	3.067420e-01	2.116618e-01	2.472928e-01	2.392648e-01
1.70	1.140019e+00	4.096928e-02	4.096928e-02	2.699397e-01	2.512319e-01
1.90	1.138303e+00	5.055274e-02	5.055274e-02	2.605036e-01	2.411255e-01
2.10	8.782694e-01	5.792508e-02	5.792508e-02	2.133691e-01	1.993480e-01
2.30	8.876176e-01	7.068992e-02	6.929131e-02	2.070097e-01	1.922042e-01
2.50	9.233839e-01	8.484274e-02	8.276087e-02	2.068395e-01	1.907514e-01
2.70	8.302704e-01	9.718814e-02	9.418384e-02	1.843711e-01	1.697681e-01
2.90	7.437592e-01	1.108025e-01	1.065084e-01	1.670761e-01	1.541573e-01
3.10	8.658119e-01	1.340828e-01	1.280463e-01	1.796387e-01	1.632370e-01
3.30	7.441196e-01	1.516691e-01	1.431016e-01	1.588193e-01	1.451537e-01
3.50	8.018033e-01	1.765384e-01	1.651021e-01	1.635437e-01	1.480661e-01
3.70	9.027066e-01	2.110192e-01	1.955824e-01	1.761071e-01	1.577988e-01
3.90	7.222044e-01	2.271006e-01	2.064819e-01	1.466410e-01	1.326299e-01
4.25	6.034012e-01	1.689251e-01	1.558229e-01	1.229046e-01	1.112390e-01
4.75	1.053152e-01	1.734260e-01	1.484182e-01	5.221343e-02	5.141045e-02
5.50	2.130023e-01	2.745856e-01	2.230820e-01	6.091682e-02	5.805594e-02
6.50	7.133336e-01	6.556939e-01	4.996889e-01	1.325003e-01	1.172134e-01
7.50	-4.139161e-01	0.000000e+00	0.000000e+00	5.939082e-02	4.734950e-02
8.50	-4.422769e-01	0.000000e+00	0.000000e+00	6.387470e-02	5.111278e-02

Table C.5: R_{AA}, 60-93% centrality. The p_T is in units of GeV/c.

p_T	R_{AA}	stat. error (+)	stat error (-)	sys. error (+)	sys. error (-)
0.35	8.740632e-01	4.266099e-01	2.184022e-01	3.298594e-01	2.981839e-01
0.45	1.008445e+00	3.959751e-01	2.239471e-01	3.483984e-01	3.191453e-01
0.55	1.012713e+00	2.958826e-01	1.887002e-01	2.687152e-01	2.482152e-01
0.65	1.099787e+00	3.124996e-01	2.014285e-01	2.675962e-01	2.486774e-01
0.75	9.340980e-01	2.006333e-01	1.422494e-01	1.654390e-01	1.551599e-01
0.85	1.093781e+00	2.417259e-01	1.697744e-01	1.781275e-01	1.677645e-01
0.95	9.491096e-01	1.873600e-01	1.364703e-01	1.304880e-01	1.235566e-01
1.10	9.442473e-01	1.293498e-01	1.028445e-01	1.181253e-01	1.106010e-01
1.30	1.063009e+00	2.148176e-01	1.543166e-01	1.442549e-01	1.363677e-01
1.50	9.660997e-01	2.267561e-01	1.553008e-01	1.274980e-01	1.214408e-01
1.70	9.708854e-01	5.702154e-03	5.702154e-03	2.055198e-01	1.875283e-01
1.90	9.236783e-01	6.859427e-03	6.859427e-03	1.908788e-01	1.733036e-01
2.10	8.684982e-01	8.124718e-03	8.124718e-03	1.751869e-01	1.582142e-01
2.30	8.202205e-01	9.493343e-03	9.493343e-03	1.616900e-01	1.452466e-01
2.50	7.789452e-01	1.105040e-02	1.105040e-02	1.519373e-01	1.361361e-01
2.70	7.297604e-01	1.269853e-02	1.269853e-02	1.379146e-01	1.225775e-01
2.90	6.889383e-01	1.453201e-02	1.453201e-02	1.289548e-01	1.143180e-01
3.10	6.460798e-01	1.648403e-02	1.648403e-02	1.202595e-01	1.064466e-01
3.30	6.141343e-01	1.876734e-02	1.876734e-02	1.136815e-01	1.004690e-01
3.50	5.695334e-01	2.111797e-02	2.111797e-02	1.055074e-01	9.326525e-02
3.70	6.271871e-01	2.476506e-02	2.476506e-02	1.130695e-01	9.916497e-02
3.90	4.977715e-01	2.668061e-02	2.616889e-02	9.250532e-02	8.184382e-02
4.25	4.730596e-01	2.050430e-02	2.050430e-02	8.659464e-02	7.628755e-02
4.75	3.897326e-01	2.667957e-02	2.605332e-02	7.276941e-02	6.446623e-02
5.50	3.418942e-01	3.653046e-02	3.527843e-02	6.513597e-02	5.801528e-02
6.50	3.599638e-01	6.373009e-02	6.014952e-02	6.803619e-02	6.047195e-02
7.50	5.401265e-01	1.240809e-01	1.142510e-01	9.703279e-02	8.501030e-02
8.50	5.159447e-01	1.767052e-01	1.577490e-01	1.240727e-01	1.157454e-01

Table C.6: R_{AA}, minimum-bias. The p_T is in units of GeV/c.

Appendix D

Tables of Inclusive $e^{\pm}$ v_2

p_T	v_2	stat. error	sys. error
0.35	4.760650e-02	2.882985e-03	2.380325e-03
0.45	5.267120e-02	3.234718e-03	2.633560e-03
0.55	5.372072e-02	3.616731e-03	2.686036e-03
0.65	4.749331e-02	4.219087e-03	2.374665e-03
0.75	5.443914e-02	4.884637e-03	2.721957e-03
0.85	7.566610e-02	5.785691e-03	3.783305e-03
0.95	6.840442e-02	6.889142e-03	3.420221e-03
1.10	5.456773e-02	6.180304e-03	2.728386e-03
1.30	6.544634e-02	8.587361e-03	3.272317e-03
1.50	6.716076e-02	1.185611e-02	3.358038e-03
1.70	6.153945e-02	1.608124e-02	3.076972e-03
1.90	1.608243e-02	2.173146e-02	8.041214e-04
2.25	3.124258e-02	2.142829e-02	1.562129e-03
2.75	7.902531e-02	3.898897e-02	3.951266e-03
3.50	1.580319e-01	5.630710e-02	7.901597e-03
4.50	-1.979039e-01	1.407917e-01	9.895195e-03

Table D.1: Inclusive $e^{\pm}$ v_2, 0-10% centrality. The p_T is in units of GeV/c.

p_T	v_2	stat. error	sys. error
0.35	5.783365e-02	2.064026e-03	2.891682e-03
0.45	6.364712e-02	2.314526e-03	3.182356e-03
0.55	7.246123e-02	2.593015e-03	3.623061e-03
0.65	7.699879e-02	3.026397e-03	3.849939e-03
0.75	7.783202e-02	3.557355e-03	3.891601e-03
0.85	8.368179e-02	4.220259e-03	4.184090e-03
0.95	8.910910e-02	5.045223e-03	4.455455e-03
1.10	9.496310e-02	4.547701e-03	4.748155e-03
1.30	8.616297e-02	6.339700e-03	4.308149e-03
1.50	1.090798e-01	8.758482e-03	5.453988e-03
1.70	1.149649e-01	1.189120e-02	5.748246e-03
1.90	9.579952e-02	1.596570e-02	4.789976e-03
2.25	1.156596e-01	1.555936e-02	5.782980e-03
2.75	1.107629e-01	2.889120e-02	5.538147e-03
3.50	6.869309e-02	4.016767e-02	3.434655e-03
4.50	4.799103e-02	9.157437e-02	2.399552e-03

Table D.2: Inclusive $e^{\pm}$ v_2, 10-20% centrality. The p_T is in units of GeV/c.

p_T	v_2	stat. error	sys. error
0.35	7.624912e-02	1.681991e-03	3.812456e-03
0.45	8.528262e-02	1.895644e-03	4.264131e-03
0.55	9.224761e-02	2.149564e-03	4.612380e-03
0.65	1.014798e-01	2.545081e-03	5.073988e-03
0.75	1.152660e-01	3.020115e-03	5.763301e-03
0.85	1.190773e-01	3.594875e-03	5.953863e-03
0.95	1.171907e-01	4.315597e-03	5.859535e-03
1.10	1.259138e-01	3.934308e-03	6.295691e-03
1.30	1.355899e-01	5.512062e-03	6.779496e-03
1.50	1.597048e-01	7.579794e-03	7.985240e-03
1.70	1.548802e-01	1.028910e-02	7.744008e-03
1.90	1.281370e-01	1.387341e-02	6.406851e-03
2.25	1.267328e-01	1.352852e-02	6.336642e-03
2.75	9.688171e-02	2.461458e-02	4.844085e-03
3.50	1.107682e-01	3.480960e-02	5.538411e-03
4.50	5.994806e-02	8.610379e-02	2.997403e-03

Table D.3: Inclusive $e^{\pm}$ v_2, 20-40% centrality. The p_T is in units of GeV/c.

p_T	v_2	stat. error	sys. error
0.35	9.222989e-02	3.686295e-03	4.611494e-03
0.45	1.078462e-01	4.183287e-03	5.392310e-03
0.55	1.205348e-01	4.867389e-03	6.026739e-03
0.65	1.259402e-01	5.871391e-03	6.297010e-03
0.75	1.143525e-01	7.075758e-03	5.717624e-03
0.85	1.459443e-01	8.508150e-03	7.297214e-03
0.95	1.390018e-01	1.029167e-02	6.950088e-03
1.10	1.481121e-01	9.474255e-03	7.405604e-03
1.30	1.736708e-01	1.326830e-02	8.683539e-03
1.50	1.385112e-01	1.825116e-02	6.925560e-03
1.70	1.338779e-01	2.511921e-02	6.693897e-03
1.90	1.841905e-01	3.347431e-02	9.209525e-03
2.25	1.110654e-01	3.203600e-02	5.553268e-03
2.75	1.745330e-01	5.755802e-02	8.726652e-03
3.50	1.411793e-01	8.226904e-02	7.058966e-03
4.50	-1.672124e-01	1.905142e-01	8.360622e-03

Table D.4: Inclusive $e^{\pm}$ v_2, 40-60% centrality. The p_T is in units of GeV/c.

p_T	v_2	stat. error	sys. error
0.35	8.165601e-02	1.825741e-02	4.082800e-03
0.45	1.125040e-01	2.083955e-02	5.625200e-03
0.55	8.414244e-02	2.486066e-02	4.207122e-03
0.65	5.786288e-02	3.025280e-02	2.893144e-03
0.75	1.427307e-01	3.727605e-02	7.136536e-03
0.85	1.775036e-01	4.536977e-02	8.875180e-03
0.95	1.314462e-01	5.462717e-02	6.572310e-03
1.10	1.856234e-01	5.089898e-02	9.281171e-03
1.30	1.439532e-01	7.238497e-02	7.197659e-03
1.50	7.080564e-02	9.996650e-02	3.540282e-03
1.70	4.569599e-01	1.301919e-01	2.284800e-02
1.90	1.732901e-01	1.746531e-01	8.664503e-03
2.25	2.818493e-01	1.749664e-01	1.409246e-02
2.75	1.531869e-03	3.194507e-01	7.659343e-05
3.50	-1.721894e+00	4.472159e-01	8.609469e-02
4.50	1.276378e+00	1.455662e+00	6.381889e-02

Table D.5: Inclusive $e^{\pm}$ v_2, 60-93% centrality. The p_T is in units of GeV/c.

p_T	v_2	stat. error	sys. error
0.35	6.325945e-02	1.406267e-03	3.162973e-03
0.45	7.128252e-02	1.576815e-03	3.564126e-03
0.55	7.614288e-02	1.777249e-03	3.807144e-03
0.65	7.731211e-02	2.086268e-03	3.865606e-03
0.75	8.489975e-02	2.452087e-03	4.244988e-03
0.85	9.905566e-02	2.905268e-03	4.952783e-03
0.95	9.538952e-02	3.471491e-03	4.769476e-03
1.10	9.662803e-02	3.133984e-03	4.831401e-03
1.30	1.027708e-01	4.371215e-03	5.138541e-03
1.50	1.107808e-01	6.039557e-03	5.539042e-03
1.70	1.192742e-01	8.174780e-03	5.963708e-03
1.90	8.973487e-02	1.099588e-02	4.486744e-03
2.25	9.516690e-02	1.070878e-02	4.758345e-03
2.75	1.005549e-01	1.962405e-02	5.027745e-03
3.50	6.178260e-02	2.824344e-02	3.089130e-03
4.50	-1.577542e-02	6.952706e-02	7.887709e-04

Table D.6: Inclusive $e^{\pm}$ v_2, minimum-bias. The p_T is in units of GeV/c.

Appendix E

Tables of Heavy-Flavor $e^{\pm}$ v_2

p_T	v_2	stat. error	sys. error
0.40	8.256271e-02	1.164303e-02	1.870189e-02
0.60	5.719609e-02	8.818214e-03	6.853138e-03
0.80	6.290778e-02	9.129460e-03	8.017550e-03
1.05	6.049593e-02	9.647478e-03	5.161185e-03
1.40	5.606522e-02	1.016181e-02	4.276922e-03
1.80	1.651529e-02	1.668369e-02	6.954014e-03
2.50	1.737177e-02	2.219941e-02	6.235898e-03
4.00	1.271644e-01	5.827845e-02	1.527983e-02

Table E.1: Heavy-flavor $e^{\pm}$ v_2, 0-10% centrality. The p_T is in units of GeV/c.

p_T	v_2	stat. error	sys. error
0.40	3.694658e-02	9.587381e-03	1.749424e-02
0.60	5.624117e-02	6.518020e-03	1.050149e-02
0.80	5.317737e-02	6.587451e-03	1.020374e-02
1.05	6.798049e-02	7.039021e-03	8.203584e-03
1.40	6.324027e-02	7.650217e-03	7.974722e-03
1.80	8.698330e-02	1.249145e-02	6.972227e-03
2.50	1.001554e-01	1.627119e-02	6.330503e-03
4.00	4.251829e-02	4.065234e-02	5.377301e-03

Table E.2: Heavy-flavor $e^{\pm}$ v_2, 10-20% centrality. The p_T is in units of GeV/c.

p_T	v_2	stat. error	sys. error
0.40	6.580105e-02	8.071746e-03	1.909121e-02
0.60	7.358078e-02	5.470889e-03	1.442064e-02
0.80	1.122819e-01	5.680151e-03	1.050324e-02
1.05	9.517557e-02	6.272793e-03	1.052311e-02
1.40	1.307341e-01	7.023130e-03	8.869125e-03
1.80	1.275172e-01	1.129190e-02	8.660880e-03
2.50	8.573235e-02	1.460081e-02	9.036791e-03
4.00	8.213341e-02	3.601407e-02	6.816007e-03

Table E.3: Heavy-flavor $e^{\pm}$ v_2, 20-40% centrality. The p_T is in units of GeV/c.

p_T	v_2	stat. error	sys. error
0.40	1.018307e-01	1.565025e-02	2.078766e-02
0.60	1.284072e-01	1.132442e-02	1.512040e-02
0.80	9.746450e-02	1.310444e-02	1.582105e-02
1.05	1.186123e-01	1.486201e-02	1.215435e-02
1.40	1.484011e-01	1.729204e-02	1.065534e-02
1.80	1.169462e-01	2.883758e-02	1.175039e-02
2.50	8.054577e-02	3.531771e-02	1.185663e-02
4.00	6.644377e-02	8.561446e-02	1.037925e-02

Table E.4: Heavy-flavor $e^{\pm}$ v_2, 40-60% centrality. The p_T is in units of GeV/c.

p_T	v_2	stat. error	sys. error
0.40	4.184655e-02	7.403708e-03	1.940162e-02
0.60	4.696397e-02	5.109513e-03	1.377803e-02
0.80	6.241914e-02	5.065789e-03	1.116422e-02
1.05	6.114115e-02	5.250753e-03	1.036070e-02
1.40	7.684462e-02	5.488322e-03	8.099785e-03
1.80	7.785165e-02	8.799723e-03	8.334638e-03
2.50	5.669380e-02	1.139180e-02	8.912527e-03
4.00	8.925567e-03	2.923994e-02	9.125356e-03

Table E.5: Heavy-flavor $e^{\pm}$ v_2, minimum-bias. The p_T is in units of GeV/c.

Bibliography

[1] E.V. Shuryak, Phys. Repts. **61**, 71 (1980).

[2] I. Arsene *et al.*, Nucl. Phys. **A757**, 1 (2005).

[3] K. Adcox *et al.*, Nucl. Phys. **A757**, 184 (2005).

[4] B.B. Back *et al.*, Nucl. Phys. **A757**, 28 (2005).

[5] J. Adams *et al.*, Nucl. Phys. **A757**, 102 (2005).

[6] K. Rajagopal, Acta Phys. Polon. B31 (2000) 3021.

[7] S.S. Adler *et al.*. Phys. Rev. Lett. **94**, 082301 (2005).

[8] E. Shuryak, Phys. Rev. C**55** 961 (1997).

[9] S. Gavin, P. L. McGaughey, P. V. Ruuskanen, R. Vogt, Phys. Rev. C**54** 2606 (1996).

[10] R.Baier, Yu.L.Dokshitzer, S.Peign, D.Schiff, Phys. Lett. B345, 277 (1995).

[11] M. Gyulassy, P. Levai, I. Vitev, Phys. Rev. Lett. **85**, 5535 (2000).

[12] E. Wang, X.-N. Wang, Phys. Rev. Lett. **87** 142301 (2001).

[13] F. Aversa, P. Chiappetta, M. Greco, J. P. Guillet, Nucl. Phys. **B327**, 105 (1989).

[14] B. Jager, A. Schafer, M. Stratmann, W. Vogelsang, Phys. Rev. D**67** 054005 (2003).

[15] S. S. Adler, et al., Phys. Rev. Lett. **91** 241803 (2003).

[16] S. S. Adler, et al., Phys. Rev. Lett. **91** 072303 (2003).

[17] D. Antreasyan, et al., Phys. Rev. D**19** 764 (1979).

[18] S. S. Adler, et al., Phys. Rev. C**69** 034910 (2004).

[19] S. S. Adler, et al., Phys. Rev. Lett. **91** 172301 (2003).

[20] K.J. Eskola, H. Honkanen, C.A. Salgado, U.A. Wiedemann Nucl. Phys. **A747** 511 (2005).

[21] Yu. L. Dokshitzer, D.E. Kharzeev, Phys. Lett. B**519** 199 (2001).

[22] R.Baier, Yu.L.Dokshitzer, A.H.Mueller, S.Peign, D.Schiff, Nucl. Phys. **B483**, 291 (1997).

[23] Miklos Gyulassy, Ivan Vitev, Xin-Nian Wang, Ben-Wei Zhang, arXiv:nucl-th/0302077v2.

[24] S. S. Adler, *et al.*, Phys. Rev. Lett. **91** 182301 (2003).

[25] P. Huovinen, P. F. Kolb, U. W. Heinz, P. V. Ruuskanen, S. A. Voloshin, Phys. Lett. B**503** 58 (2001).

[26] Jean-Yves Ollitrault. Reconstructing azimuthal distributions in nucleus-nucleus collisions. arXiv:nucl-ex/9711003

[27] A. M. Poskanzer and S. A. Voloshin. Phys. Rev. C**58**, Number 3, 1671 (1998).

[28] S.S. Adler *et al.*, Phys. Rev. C**72**, 024901 (2005).

[29] S.S. Adler *et al.*, Phys. Rev. Lett. **96** 032301 (2006).

[30] I. G. Bearden *et al.*, Phys. Rev. Lett. **88** 202301 (2002).

[31] Magdalena Djordjevic, Miklos Gyulassy, Simon Wicks, Phys. Rev. Lett. **94** 112301 (2005).

[32] N. Armesto, M. Cacciari, A. Dainese, C.A. Salgado, U.A. Wiedemann, Phys. Lett. B**637** 362 (2006).

[33] Simon Wicks, William Horowitz, Magdalena Djordjevic, Miklos Gyulassy, Nucl. Phys. **A784** 426 (2007).

[34] K. Adcox *et al.*, Nucl. Instrum. Methods **A499** 469 (2003).

[35] K. Adcox *et al.*, Nucl. Instrum. Methods **A499** 508 (2003).

[36] K. Adcox *et al.*, Nucl. Instrum. Methods **A499** 521 (2003).

[37] S.C. Johnson et. al. Three-Dimensional Track Finding in the PHENIX Drift Chamber by a Combinatorial Hough Transform Method. *International Conference on Computing in High Energy Physics (CHEP '98)*, Chicago, USA, 1998.

[38] G. David *et al.*, IEEE Trans. Nucl. Sci. 47 (2000) 1982.

[39] Azfar Adil, Ivan Vitev, arXiv:hep-ph/0611109v1

[40] G.Martinez-Garcia, S.Gadrat, P.Crochet, arXiv:hep-ph/0702035v2

[41] Z.w. Lin, D. Molnar, Phys. Rev. C**68**. 044901 (2003).

[42] G. D. Moore and D. Teaney, Phys. Rev. C**71**, 064904 (2005).

[43] V. Greco, C.M. Ko, R. Rapp, Phys. Lett. B**595**, 202 (2004).

[44] S. S. Adler *et al.*, Phys. Rev. Lett. **96** 032001 (2006).

[45] J. Adams *et al.*, Phys. Rev. Lett. **94** 062301 (2005).

[46] H. van Hees, V. Greco, and R. Rapp, Phys. Rev. C**73**, 034913 (2006).

[47] J. M. Maldacena, Adv. Theor. Math. Phys. **2**, 231 (1998).

[48] E. Witten, Adv. Theor. Math. Phys. **2**, 505 (1998).

[49] H. Liu, K. Rajagopal, and U. Wiedemann, Phys. Rev. Lett. **97** 182301 (2006).

[50] C. P. Herzog *et al.*, J. High Energy Phys. 07 (2006) 013.

[51] S. S. Gubser, Phys. Rev. D**74**, 126005 (2006).

[52] J. J. Friess, S. S. Gubser, and G. Michalogiorgakis, J. High Energy Phys. 09 (2006) 072.

[53] R.Averbeck, A. Drees, Y. Akiba, and T. Hachiya, PHENIX Analysis Note 089.

[54] N. Kroll, W. Wada. Phys. Rep. 98, 1355 (1955).

[55] Y. Akiba, R. Averbeck, A. Dion, F. Kajihara, PHENIX Analysis Note 415.

[56] R. Averbeck, PHENIX Analysis Note 349.

[57] S.S. Adler et. al. (PHENIX), nucl-ex/0611007

[58] T. Isobe *et al.*, PHENIX Analysis Note 444.

[59] PHENIX, PPG051, Phys. Rev. Lett. **96**, 202301 (2006).

[60] V. Ryabov *et al.*(PHENIX), hep-ex/0607012.

[61] PHENIX, PPG026, Phys. Rev. C**69**, 034909 (2004).

[62] Y. Akiba, R. Averbeck, S. Butsyk, X. Li, G. Roche, PHENIX Analysis Note 357.

[63] PHENIX, PPG042, Phys. Rev. Lett. **94**, 232301 (2005).

[64] PHENIX, A. Adare *et al.*. Phys. Rev. Lett. **97**, 252002 (2006).

[65] H. Masui *et al.*, PHENIX Analysis Note 445.

[66] David Winter *et al.*, PHENIX Analysis Note 434.

[67] A. Adare *et al.*(PHENIX). Phys. Rev. Lett. **98**, 162301 (2007).

[68] M. Cacciari *et al.*. Phys. Rev. Lett. **95**, 122001 (2005).

[69] S.S. Adler *et al.*. Phys. Rev. Lett. **91**, 072301 (2003).

[70] A. Kozlov *et al.*, Nucl. Instrum. Methods **A523**, 345 (2004).

[71] Johann Heuser *et al.*, Nucl. Instrum. Methods **A511**, 210 (2003).

[72] O. Socolowski, F. Grassi, Y. Hama and T. Kodama, Phys. Rev. Lett. **93** 182301 (2004).

[73] H. Drescher *et al.*, arXiv:0704.3553.